# Diagnostics of a pulsed low-current high-voltage discharge operated at atmospheric pressure

*Michał Jerzy Szulc*

Universität der Bundeswehr München

Fakultät für Elektrotechnik und Informationstechnik
Institut für Plasmatechnik und Mathematik

# Diagnostics of a pulsed low-current high-voltage discharge operated at atmospheric pressure

Michał Jerzy Szulc

# Acknowledgements

The genesis of this work is long and winding. However, as the completion of any thesis means the beginning of a new chapter, I would like to thank the main "actors" who played a role in this spectacle. It was a spectacle of trust and faith in my abilities given by the following players throughout my professional career, that pushed me to tackle much bigger things than I probably would have dared to think about. Some would call this "ride" I went through a little bumpy, but for me it was very experience-rich and allowed me to mature into the human I am now.

First and foremost, I would like to thank the supervisor of this thesis, Prof. Dr.-Ing. Jochen Schein, for accepting the initial proposition of an industrial doctorate several years ago and then, as time passed, for making me join the ranks of his Institute for Plasma Technology and Basics of Electrical Engineering. I would like to thank him for the trust he has placed in me from the beginning, for the scientific freedom he has given me to deal with many different and sometimes only loosely plasma-related topics, for taking care of the financial hurdles, and for always being open and supportive in difficult times. He is the one who made sure that my scientific career literally came full circle and that I returned to the origin, the pulsed low-current high-voltage plasmas. Thank you, Jochen.

Furthermore, I would like to thank the second reviewer of this thesis, Prof. Dr.-Ing. Eckart Theophile. He, together with a bunch of other passionate "Plasmatiker" at Reinhausen Plasma, back in the day led by Thorsten Krüger, sparked my passion for plasma. The incredible confidence these guys had in me back then often made me unconsciously punch way above my weight. As a result, till this day I benefit from the experience gathered while working on an amazing variety of topics under their leadership. Eckart is also the one who laid the foundation of this work and established the contact with Jochen. I vividly remember one of our conversations about the future and Eckart's very clear answer that he would never return to science... And here we are, after all these years, we have come full circle. Who would have thought that the guy I once danced on the tables at 2 a.m. would become a professor and furthermore be the second reviewer of my thesis? Thank you, Eckart.

At this point, I would also like to thank Prof. Dr. rer. nat. Georg Düsberg for chairing the examination committee and taking care of all the formalities involved.

In addition, my gratitude goes to a brilliant (plasma) physicist, Dr. rer. nat. Jose-Luis Marques-Lopez, who has had enough patience and perseverance to hash and rehash the nuances of non-equilibrium plasmas with me over and over again. The countless discussions with him contributed significantly to the final form of this thesis. He was and is, dare I say, my personal plasma-life mentor. Jose, I sincerely thank you for your time, listening to my whining, brainstorming about the observed effects and all the support along the way.

Another personal plasma-life mentor of mine, whose contribution to this work was equally significant, is the Institute's Master Yoda, Dr.-Ing. Günter Forster. He took care of the scientific newcomer, who initially had no idea about plasma diagnostics and was hiding behind the vacuum facility in the welding lab, and showed him the secrets of a plethora of methods. He was the one who took me by my hand and explained every step of light scattering and so much more... I still claim to be a novice in plasma diagnostics, but he probably claims the same about himself. And although I have strenuously tried to bring him to the verge of rage, I have not succeeded! Günter, I wholeheartedly thank you for supporting and believing in me throughout all the years we spent together inside and outside of the lab.

I would like to express my gratitude to the active and former veteran scientists of the Institute, Dr.-Ing. Karsten "the King" Hartz-Behrend, Dr.-Ing. Stephan "Zimbo" Zimmermann and Dr.-Ing.

# Contents

# Abstract

More and more plasma-assisted processes are finding their way into technological applications and thus into various areas of our lives. Examples include surface treatment in joining technology or, more recently, applications in the health sector. However, the plasma-chemical or plasma-physical effects that occur in such processes are complex and have not yet been fully clarified, which means that empirical investigations are required. Therefore, a detailed diagnostic investigation of the plasmas used is indispensable for a better understanding of the processes as a whole.

One of the most industrially used principle for plasma generation is a pulsed low-current high-voltage discharge with a power between 0.3 kW and 1 kW. Nevertheless, no previous work could yet be found in which the relevant plasma parameters, or more specific the electron number density and electron temperature, for such discharge were determined purely experimentally. Thus, the main objective of this work is to characterise a pulsed low-current high-voltage discharge under atmospheric pressure as holistically as possible by combining quantitative and qualitative diagnostic methods. In particular, the electron parameters should be determined experimentally by means of laser scattering.

The scattering results show that, depending on the operating frequency, an electron density between $1.7 \times 10^{21}$ m$^{-3}$ and $2.0 \times 10^{21}$ m$^{-3}$ with electron temperatures in the range of 40000 K can be expected for a pulsed nitrogen discharge of this type at atmospheric pressure. A heavy particle temperature of about 6000 K is reached in the core of the discharge channel at nozzle exit, and drops downstream in the axis of the emerging plasma jet from 4000 K at 10 mm to 2000 K at 15 mm from the outlet. Due to the complex nature of the excitation processes of nitrogen, relatively slow electron recombination rates are observed so that the discharge channel, once ionised, does not extinguish between successive pulses but transitions from a glow discharge to a spark discharge with each pulse. Furthermore, the behaviour of the discharge was visualised with additional camera-based diagnostics.

In summary, the results obtained in this work contribute significantly to the understanding of pulsed low-current high-voltage discharges at atmospheric pressure. The quantitative results can facilitate the validation and development of existing and new computational models to achieve a more accurate spatial composition of the plasma. This knowledge, extended by the findings of qualitative diagnostics, can be used to better adapt such discharges to specific applications in industrial or experimental environments.

Parts of this work were published in:

– M. Szulc, G. Forster, J.-L. Marques-Lopez and J. Schein. A simple and compact laser scattering setup for characterization of a pulsed low-current discharge. *Appl. Sci.*, 12(14):6915, 2022. URL: https://doi.org/10.3390/app12146915

– M. Szulc, G. Forster, J.-L. Marques-Lopez and J. Schein. Spectroscopic characterization of a pulsed low-current high-voltage discharge operated at atmospheric pressure. *Appl. Sci.*, 12(13):6580, 2022. URL: https://doi.org/10.3390/app12136366

– M. Szulc, G. Forster, J.-L. Marques-Lopez and J. Schein. Influence of pulse amplitude and frequency on plasma properties of a pulsed low-current high-voltage discharge operated at atmospheric pressure. *Appl. Sci.*, 12(13):6366, 2022. URL: https://doi.org/10.3390/app12136580

# Kurzfassung

Plasmagestützte Prozesse finden zunehmend Einzug in technologische Anwendungen und somit in verschiedene Bereiche unseres Lebens. Exemplarisch angeführt seien an dieser Stelle die Oberflächenbehandlung in der Fügetechnik oder, seit neustem, Anwendungen im Gesundheitswesen. Die dabei auftretenden plasmachemischen bzw. plasmaphysikalischen Effekte sind allerdings komplex und bisher nicht vollständig geklärt, wodurch man auf empirische Untersuchungen angewiesen ist. Daher ist eine möglichst detaillierte messtechnische Untersuchung der verwendeten Plasmen für ein besseres Verständnis der Prozesse unumgänglich.

Im industriellen Umfeld haben sich gepulste Niederstrom-Hochspannungsentladungen mit einer Leistung zwischen 0.3 kW und 1 kW etabliert. Bis jetzt konnten jedoch keine vorhergehenden Arbeiten gefunden werden, in denen die relevanten Plasmaparameter, genauer gesagt die Elektronenanzahldichte und Elektronentemperatur, für solche Entladungen rein experimentell ermittelt wurden. Somit ergibt sich das Hauptziel dieser Arbeit: Es soll eine gepulste Niederstrom-Hochspannungsentladung unter Atmosphärendruck durch Kombination von quantitativen und qualitativen Diagnostikmethoden möglichst umfassend charakterisiert werden. Insbesondere sollten die Elektronenparameter experimentell mittels Laserstreuung bestimmt werden.

Die Ergebnisse der Laserstreuung zeigen, dass je nach Betriebsfrequenz eine Elektronendichte zwischen $1.7 \times 10^{21}$ m$^{-3}$ und $2.0 \times 10^{21}$ m$^{-3}$ mit Elektronentemperaturen im Bereich von 40000 K für eine gepulste Stickstoffentladung dieser Art bei Atmosphärendruck zu erwarten sind. Eine Schwerteilchentemperatur von etwa 6000 K wird im Kern des Entladungskanals am Düsenaustritt erreicht, und fällt stromabwärts in der Achse des austretenden Plasmastrahls von 4000 K bei 10 mm auf 2000 K bei 15 mm ab. Aufgrund der komplexen Natur der Anregungsprozesse von Stickstoff, werden relativ langsame Elektronenrekombinationsraten beobachtet, so dass der einmal ionisierte Entladungskanal nicht zwischen aufeinanderfolgenden Impulsen erlischt, sondern mit jedem Impuls von einer Glimmentladung zu einer Funkenentladung übergeht. Zusätzlich konnte das Verhalten der Entladung mit weiteren kamerabasierten Diagnostiken visualisiert werden.

Zusammenfassend tragen die in dieser Arbeit erzielten Ergebnisse wesentlich zum Verständnis von gepulsten Niederstrom-Hochspannungsentladungen bei Atmosphärendruck bei. Die quantitativen Ergebnisse können die Validierung und Entwicklung von bestehenden und neuen Berechnungsmodellen unterstützen. Erweitert um die Erkenntnisse der qualitativen Diagnostiken können solche Entladungen besser an spezifische, industrielle oder experimentelle Anwendungen angepasst werden.

Teile dieser Arbeit wurden in folgenden Publikationen veröffentlicht:

– M. Szulc, G. Forster, J.-L. Marques-Lopez and J. Schein. A simple and compact laser scattering setup for characterization of a pulsed low-current discharge. *Appl. Sci.*, 12(14):6915, 2022. URL: https://doi.org/10.3390/app12146915

– M. Szulc, G. Forster, J.-L. Marques-Lopez and J. Schein. Spectroscopic characterization of a pulsed low-current high-voltage discharge operated at atmospheric pressure. *Appl. Sci.*, 12(13):6580, 2022. URL: https://doi.org/10.3390/app12136366

– M. Szulc, G. Forster, J.-L. Marques-Lopez and J. Schein. Influence of pulse amplitude and frequency on plasma properties of a pulsed low-current high-voltage discharge operated at atmospheric pressure. *Appl. Sci.*, 12(13):6366, 2022. URL: https://doi.org/10.3390/app12136580

# 1

# INTRODUCTION

The Earth. A phenomenon in every respect. The only planet in our solar system where life is found in such diversity. Made possible by a thin layer of atmosphere which allowed the emergence of an ecosystem that at first glance may seem simple, but at second glance is complex and, above all, fragile. A system in which four common states of matter can be observed: solid, liquid, gas and plasma. In contrast to the rest of the universe, naturally occurring plasmas are rather an exception on Earth. These include the auroras at the Earth's respective poles as well as atmospheric discharges during thunderstorms that result from electrostatic charging of clouds. As nature suggests, the use of electrical energy is the simplest method to create artificial, i.e. man-made, plasmas on Earth. Accordingly, all plasmas used industrially are artificial, thus no further distinction is made between the terms artificial and natural plasma in the following.

Plasma is, similarly to the Earth, a phenomenon in itself. Macroscopically, a luminous gas which reacts to electromagnetic fields. Microscopically, a mixture of electrons, atomic and molecular ions with different energy states and neutrals. Simple at first glance, but in reality complex, it allows things to be achieved that might otherwise be difficult, environmentally harmful or uneconomical. The range of applications for atmospheric pressure plasmas is surprisingly broad and depends mainly on the power input. At high power levels in the range of several kW or more, the plasma is assumed to be in thermal and chemical equilibrium. This means that the electron number density is assumed to be equal to the number density of ionized species and that all particles, despite their different size and mass, can be described by the same energy distribution function [24, 58, 148]. Such plasmas are used industrially for welding, cutting, coating or melting of various materials, in chemical analysis or waste treatment, to name just a few applications [89, 149, 153]. The lower the input power, the more the plasma is in non-equilibrium, which roughly means that the energy is distributed differently between electrons and heavy particles [24]. Due to their smaller size and weight, the electrons gain more energy than the heavy particles, resulting in higher chemical reactivity and lower gas temperature. Therefore, the application of non-equilibrium plasmas extends over many branches of industry. In the automotive and packaging industries, for example, surfaces are treated before bonding, printing or painting [41, 78, 82, 135]. Surfaces are hydrophilized or hydrophobized by deposition of layers as a result of a chemical reaction induced by such plasmas [21, 42]. Various layers of low-melting materials are coated onto temperature-sensitive substrates [90, 95, 146, 178]. The antibacterial properties of non-equilibrium plasmas are used and intensively explored in food and medical industries [3, 38, 165, 181]. In the environmental sector, such plasmas are used to neutralize industrial waste gases by selective removal of chemical compounds [22, 42, 174]. Also, possible applications to increase efficiency in the production of synthetic fuels are being explored [73, 159]. Many of these applications are of great importance to humanity in order to preserve the fragile balance of our ecosystem on Earth.

**1**

## 1.1 PULSED LOW-CURRENT DISCHARGES AND THEIR DIAGNOSTICS

Non-equilibrium plasma is often generated by a pulsed low-current high-voltage discharge [3, 13, 15, 180]. This type of discharge became more and more popular with the development of power electronics and is also the subject of this work. It is characterized during steady-state operation by voltages usually in the range of a few kV and currents seldom exceeding a couple of amperes. Due to the rather low current, such a discharge is reported to be sensitive to gas flow changes [128]. Additionally, regardless of whether the power supply is pulsed or the discharge pulsates due to its nature (for ex. gliding arc), a pulsed modus operandi inherently implies a frequency dependence of the plasma properties, which are primarily defined by the plasma carrier gas used [180]. Furthermore, the plasma has a nonlinear load character, what thus complicates the control of such a discharge [51, 152].

Plasma kinetics is defined by electron number density $n_e$ and electron temperature $T_e$, because electrons can absorb much more energy from the external electric field due to their lightness compared to other plasma constituents [123, 180]. As a result, if the electron number density is high, the ionization and dissociation reactions are driven by inelastic electron collisions. Nevertheless, these reactions can also be governed by inelastic atom and molecule collisions, depending on the conditions and the plasma carrier gas used [4, 11]. Thus, the knowledge of the heavy particle temperature $T_h$ is sometimes as important as the knowledge of the electron parameters, i.e. $n_e$ and $T_e$ [179]. Consequently, the result of a plasma treatment depends on the chemistry, which is governed by an interplay of collision rates of energetic electrons and of ions with other particles or neutrals of the surrounding gas [15]. Therefore, the knowledge of the quantities $n_e$, $T_e$ and $T_h$, allows the assessment of the chemical reactivity of a plasma and allows to achieve better control over the occurring reactions as a consequence [180].

The pulsed mode of operation of a low-current discharge, whether self-pulsed or actively controlled, offers several advantages over a DC power supply. First and foremost, it facilitates the achievement of non-equilibrium conditions [13], making the plasma thus more chemically reactive [15, 159]. Thereafter, a pulsed operation is usually characterized by a lower energy consumption [68, 98]. Then, the choice of the operating frequency as well as the shape of an excitation pulse allow separate controllability of electron and heavy particle temperatures [15, 113], enabling a better matching of the plasma to the application needs. These advantages have contributed to the fact that pulsed low-current discharges operated at atmospheric pressure are now well established industrially and are constantly growing [180]. Accordingly, several systems from different manufacturers are commercially available [41, 81, 95, 178, 182]. Thereby both the design of the plasma generator, characterized by a finger-shaped inner electrode and a non-segmented nozzle as a second electrode, and the operating principle of these systems, with the excitation pulses being more or less actively controlled or shaped by the power supply, are generally similar and are thus comparable to the system studied in this work. Another type of low-current discharge, which is perhaps not as widespread industrially as the previous one, but is often used in studies under laboratory conditions, is the so-called gliding arc. A gliding arc is in its simplest form a discharge ignited in a transversal gas flow between two divergent electrodes. Due to the gas flow the conducting channel is blown along the diverging electrodes, thus the discharge is often referred to as self-pulsating, whereby it undergoes a transition from thermal to non-thermal equilibrium with increasing length according to different authors [34, 62, 129]. Although the first reports of such discharges date to the beginning of the twentieth century, the modern godfathers of gliding arcs, A. Czernichowski, A. Friedman and A. Gutsol, determined diagnostically the most important parameters [34, 62]. A more complicated swirl-stabilized gliding arc discharge generator, to some extent similar to a conventional plasma generator such as the one used in this work, has also been developed and is referred to in the literature as a gliding arc plasmatron [60, 136] or tornado discharge [80]. A detailed description of such discharges can be found, for example, in [51] or [80].

Due to the wide application field and industrial spread of pulsed low-current discharges, a plethora of publications exist in which this type of discharge is studied. Mostly, however, the effects achieved as a result of a plasma treatment are being characterized, rather than the discharge itself, as presented

in [38, 78, 81, 94, 111, 135, 161], to name a few. In references dealing with the characterization of such discharges, researchers often describe their behavior using electrical measurements [51, 68, 80, 95] or emission spectroscopy. The latter diagnostic method is primarily used to qualitatively describe the composition of the plasma [81, 84, 130, 146]. Only few authors estimated the temperature of heavy particles, or more precisely the rotational and vibrational temperatures of the nitrogen molecular bands, based on the recorded spectra [34, 41, 60, 99, 188]. In some cases the estimation of the gas temperature is also done by thermocouple measurements [95, 136, 146]. This may be easy to implement, but the temperature values which can be assessed are significantly limited by the sensor used. Furthermore, due to the ratio of the sensor size to the measured object size, this method only allows the recording of integral values. Additionally, precautions have to be taken against possible electromagnetic interference, often by embedding the sensor in an insulating tube as in [95], which further increases its diameter. Therefore, spectroscopic measurements or laser scattering diagnostics should be preferred over thermocouple-based ones for the evaluation of $T_h$ with regard to the chemical reactivity of the plasma under study, while calorimetric measurements as presented in [84, 86] are preferable if the thermal load of the substrate is to be evaluated. Nevertheless, as suggested by Fröhlich et al., calorimetric measurements can be improved by taking into account the energy flux caused by convection, which depends on the gas temperature, but according to the authors, an assumption of the gas temperature of a plasma under study is not readily possible [49]. Thereafter, an experimental determination of $T_h$ seems to be a reasonable addition to the calorimetric diagnostic methods.

The energy distribution in a plasma and the associated energy transfer to the treated surface is important [40], as it can affect the treated surface by etching or thermal modification [135], influence the efficiency of chemical vapour thin film deposition [21, 146] or the antibacterial effects of a plasma [3, 115, 144]. As pointed out by Carton et al., who deposited and analysed acrylic acid thin films in [21], an increase in plasma temperature achieved by increasing the operating frequency can be compensated by faster lateral movement of the generator to achieve similar coating efficiencies. When the frequency was varied, the analysis of deposited layers revealed different chemical properties though, suggesting a temperature dependence of the plasma reactivity [21]. Pulpytel et al. reported similar effects and indicated that the steep axial temperature gradient plays an important role in the chemical composition of a coating [146]. The correlation between the plasma properties, i.e. chemical composition and characteristic temperatures, and the effects observed after a treatment becomes visible when considering different hydrodynamic models. Dorai and Kushner developed a detailed model for plasma modification of polypropylene, emphasizing the variety of reactions occurring in the plasma and the temperature dependence of the corresponding reaction rate coefficients [39]. The temperature dependence of the rate coefficients of $N_2$ and $O_2$ dissociation and ionization reactions governed by electrons can be found in the work of Tanaka et al., who developed a hydrodynamic chemical non-equilibrium model of a pulsed discharge [167]. In this work, the researchers concentrated on the modelling of chemical non-equilibrium effects by calculating with a single temperature, but indicated that a non-thermal equilibrium model should be adopted for pulsed discharges. A chemical non-equilibrium is generally related to diffusive and convective transport processes as well as radiation [8], it is more pronounced the greater the separation between the electron and heavy particle temperature is [9, 169], which is promoted by pulsed operation as stated above [15, 113, 166] and can be expected when the plasma interacts with other non-plasma media [173]. The model presented in [167] was further developed by Tanaka into a time-dependent two-temperature chemical non-equilibrium model. According to the author, several dissociation and ionization forward reactions are governed by a different temperature than the corresponding backward reactions when both thermal and chemical non-equilibrium are taken into account [166]. This, of course, increases the complexity and computational cost of such a model [173], but also indicates the need for experimental determination of plasma parameters for validation purposes. An even deeper analysis of the influence of different temperatures

(especially of the nitrogen vibrational states) on the chemistry of a plasma can be found in [186].

Based on an analysis of recent research trends [88, 180], the need for comprehensive characterization of non-thermal plasmas seems to be gaining importance as new application fields are targeted, particularly in the environmental and health domain. For example, in the recently popular research topic of plasma-activated water, due to the ability of such water to inactivate biofilm contamination in food, water and medical applications [3, 116, 187], the plasma-water interface adds complexity to the analysis of the observed effects. The reactive species generated in the gaseous plasma dissolve in water to form long-lasting aqueous species that enhance the antibacterial activity of a plasma-treated water [3, 72, 115, 185]. Thereafter, as reported by Machala and his co-workers, the concentration of the reactive species in water is determined not only by the concentration of species produced in the plasma, but also by the solubility coefficients determining the transport into the aqueous medium [115]. Since the production rate of reactive nitrogen and oxygen species depends on the power consumed by a discharge [61, 115], and thus on the electron density and temperature [187], thorough plasma characterization appears to be a key element for overall understanding of the observed effects. Another recent application for which plasma characterization seems to be important is, for example, the conversion of $CO_2$ into synthetic fuels [159].

As mentioned above, the heavy particle properties, i.e. the rotational and vibrational temperatures of different plasma constituents and to some extent their density, can be assessed experimentally by emission spectroscopy measurements and subsequent fitting of synthetic spectra, as done, for example, by Gröger *et al.* [60], Pawłat *et al.* [144] or also in this work. In comparison, the determination of the electron parameters of non-equilibrium plasmas based on spectroscopic measurements is not so straightforward. Several research groups estimated the electron density or temperature through modelling [60, 139, 152, 188]. Thereby, in addition to the estimation of rotational and vibrational temperatures, the measured spectra are used to estimate the diameter of the discharge channel, which is then used to determine the current density. Thereafter, the electron parameters can be obtained by solving the Boltzmann equation [188], an Elenbaas-Heller [152] or a collisional-radiative model [60]. Such a combined experimental and computational approach is a good estimation method, but cannot be compared with a purely experimental measurement of the electron parameters due to approximations adopted during the calculations (for ex. the assumption of thermal equilibrium). Laser scattering is one of diagnostics which allows an experimental determination of all three plasma parameters, i.e. $n_e$, $T_e$ and $T_h$. This diagnostic technique is not limited by the assumption of equilibrium conditions [70, 125], nor by the plasma composition, both atomic and molecular plasmas can be investigated [100, 170], or the operating pressure range [122, 175]. Laser scattering can provide not only a high spatial resolution [93, 176], but also a high temporal resolution when the laser is synchronized with the pulse frequency of the power supply [188]. Nonetheless, apart from Zhu *et al.*, who used a combination of laser scattering, precisely only Rayleigh scattering to estimate $T_h$ (described in chap. 2), spectroscopy and calculations to determine the temperatures of a gliding arc driven in air by a 35 kHz AC power supply [188], this technique has not yet been used to experimentally determine the electron parameters of pulsed low-current high-voltage discharges. However, the above discussion shows that an experimental determination of electron parameters, coupled with the characterization of heavy particles, can shed new light on the spatial and temporal distribution of species produced in the effluent plasma jet as well as on the modelling approaches of such discharges. With this knowledge, it is conceivable that the selectivity and controllability of plasma-induced chemical reactions can be increased in existing or new application fields.

In order to estimate the plasma parameters experimentally by means of laser scattering, the intensity of the scattered signal, which is proportional to the concentration of scattering species as well as to the intensity of the incident laser radiation [50], has to be high enough to be detected by the diagnostic setup. Laser scattering has therefore its limitations. According to [175, 176], the main detection-limiting factors are the plasma radiation and the stray light, i.e. the light scattered by

the surroundings of the measurement volume and not by the particles inside the volume. Thus, the lowest electron density that can be determined with a simple diagnostic setup consisting mainly of a laser, a spectrograph and a camera, is in the range of $10^{18}$ m$^{-3}$ [176]. Usually, at such low number densities, a mask is placed at the exit of the spectrograph to block the laser wavelength so that the detection sensitivity of the camera can be increased. However, the laser blocking mask has to be removed to calibrate the setup or to measure the temperature of heavy particles. To improve the stray light rejection, the spectral resolution of experimental setups is often increased by coupling multiple spectrographs in series, with double grating [133] or even triple grating [70, 93, 141] spectrographs most commonly used. The latter, in particular, proven to be highly effective for electron densities below $10^{20}$ m$^{-3}$ and, due to the high spectral resolution, allows in most cases a setup calibration or estimation of $T_h$ without major modifications (both based on Raman scattering) [20, 70, 175, 176]. Nevertheless, according to Reece Roth [149] as well as to calculations results [60], electron densities in the range of $10^{21}$ m$^{-3}$ are expected for non-thermal low-current discharges. Thereafter, the electron density should be high enough so that a simple laser scattering setup can be used to estimate the plasma parameters. Furthermore, depending on the intensity of the scattered radiation, it might even be possible to work without a laser blocking mask. This would allow a simultaneous measurement of all three plasma parameters without having to physically modify the experimental setup.

## 1.2 Aim and structure of this work

As can be deduced from the brief introduction, each application places different requirements on the plasma properties, which in turn depend not only on the carrier gas selected, but also on the type, i.e. pulse shape and operating frequency, of source driving the discharge. Thereafter, the knowledge of the plasma composition and possible working agents created in subsequent reactions is one of the key points for an application to be efficient and reproducible in an industrial or laboratory environment. A variety of diagnostic methods can be used to characterize a plasma. One of the methods which allows the evaluation of the most important variables with a high spatial and temporal resolution is laser scattering. By recording of the light scattered by free or bound electrons, the number density and temperature of free electrons as well as the temperature of heavy particles can be assessed. Coupled with probably the most popular plasma diagnostic technique, optical emission spectroscopy, conclusions can be drawn about the composition and energy states of excited species in the plasma. If the above methods are supplemented by further diagnostics, for ex. high speed imaging techniques, a holistic picture of the plasma is obtained for a given set of parameters.

Therefore, the aim of this work is to experimentally investigate the properties of a pulsed low-current discharge operated at atmospheric pressure by means of laser scattering, emission spectroscopy and high speed imaging. The emphasis is thereby put onto the laser scattering technique, with emission spectroscopy and high speed imaging being used as supplementary methods. A commercially available pulsed plasma system, characterized by a simple design comparable to that of other systems on the market, is chosen as a test object. Since the discharge is pulsed, the diagnostics used are to be synchronized with the operating frequency to obtain information about the temporal progression of the characteristic values. Furthermore, as outlined in section 1.1, the expected electron density should be high enough so that it might be possible to estimate the plasma parameters with a simple laser scattering setup. Thus, the estimation of the characteristic plasma values is attempted with an experimental setup that uses only a single spectrograph allowing thereby to design the setup as compact as possible. An additional objective is to simultaneously measure the electron parameters and the heavy particle temperature, i.e. without using of a laser blocking mask.

The thesis is structured as follows. The theoretical foundations of the used diagnostic methods, i.e. laser scattering and emission spectroscopy, are discussed in chapter 2, followed by the description of the experimental setups in chapter 3. In the latter, the plasma system studied as well as the triggering

**1**

of the diagnostic setups are also described. Thereafter, the detailed results are reported in chapter 4. The validation of the results by comparing of laser scattering and emission spectroscopy results, and by comparison with data published for related discharge types are presented in chapter 5. This chapter also discusses other physical effects that were observed with the diagnostics used. Finally, the achieved results and observed effects are summarized in chapter 6.

# 2

# THEORETICAL FOUNDATIONS

Three main diagnostic methods, i.e. laser scattering, emission spectroscopy and high speed imaging, are used for the investigation of the pulsed low-current discharge. The main focus is put thereby on laser scattering, since this method allows the evaluation of electron parameters regardless of whether the plasma is in thermal equilibrium or not. The emission spectroscopy is used, on the one hand, to validate the scattering results and, on the other hand, to complement the results with further information about the distribution and energy state of different species in the plasma. Therefore, the theoretical foundations presented in this chapter are divided into two sections. First, the basics of laser scattering are discussed in section 2.1 and then the basics of emission spectroscopy in section 2.2.

## 2.1 THEORY OF LASER SCATTERING

The main goal of laser scattering diagnostics is to determine relevant plasma parameters such as electron density $n_e$, electron temperature $T_e$ and the heavy particle temperature $T_h$. This can be done without prior knowledge of the plasma state, i.e. the possible departure from thermal equilibrium [50, 124]. The theoretical foundation of laser scattering was laid and comprehensively described by Evans and Katzenstein [45] as well as Sheffield [50] and Jackson [74]. In the following sections a simplified, more application-tailored theoretical description is given.

The incident laser light, an electromagnetic wave, interacts with charged plasma particles. During the short laser pulse, usually only a couple of nanoseconds long, the bound and free electrons are accelerated and follow the electric field of the incident wave due to their small mass and high mobility compared to other heavier species. Thus the electrons start to oscillate with the frequency of the incident radiation. This oscillation causes the electrons to emit electromagnetic radiation corresponding to those of an oscillating electrical dipole. Depending on the energy of the incident radiation several interaction mechanisms can be distinguished. These can be mainly divided into those in which energy is transferred to the interacting particle (called inelastic scattering) and those in which the total kinetic energy is conserved (elastic scattering). Elastic scattering of electromagnetic waves in the visible range can be divided into Rayleigh and Thomson scattering processes. In the first one photons of the incident radiation are scattered by bound electrons, in the latter one by free electrons. The electrons bound to atoms or molecules move at the velocity of the heavy particles, which is much lower compared to the velocity of free electrons, so the Rayleigh scattering signal does not undergo any significant broadening due to the Doppler shift (discussed in sect. 2.1.1) and therefore its wavelength can be considered equal to that of the incident radiation. Moreover, due to the large number of scatterers for plasmas even at a low ionization degree, Rayleigh scattering is the most pronounced signal to be registered. Regarding Thomson scattering on the other hand, the peak of the spectral distribution function is also located at the wavelength of the incident radiation, but is much wider due to Doppler broadening and its amplitude much smaller in contrast to that of Rayleigh case since the scattering

cross section of a single free electron is much smaller than that of an atom containing bound electrons. From the recorded Thomson scattering signal the absolute electron density and electron temperature can be derived. A more detailed description of the scattering principle is given in section 2.1.1. The theoretical approach of elastic scattering processes can be found in sections 2.1.2 for Thomson and 2.1.3 for Rayleigh scattering.

In case of inelastic scattering, when energy is transferred between incident radiation and plasma particles, the process is called Raman scattering. If longer wavelengths than the incident radiation are observed in the recorded signal, then energy is transferred to the interacting plasma particles and the process is referred to as Stokes Raman scattering. If a shift to shorter wavelengths can be observed the internal energy of the scattering particles has been reduced and the process is referred to as anti-Stokes Raman scattering. For molecular gases, the energy transfer during Raman scattering goes into rotational as well as vibrational exitation modes. As stated by Long [112], Raman scattering as well as Rayleigh scattering can be considered under certain conditions to be incoherent, what means that the electromagnetic interactions between charged particles within the scattering volume can be neglected. Moreover, both processes are directly proportional to the irradiance of the incident radiation and can thus be considered linear. Similarly to Rayleigh scattering, due to the rather low heavy particle velocities, the Doppler broadening can be neglected and hence the Raman spectrum consists of several narrow spectral lines at wavelengths corresponding to different energy states. Within this work, rotational Raman lines are of particular interest, since they occur in the same wavelength range as the Thomson scattered signal and can therefore influence the evaluated results [176]. This issue is discussed in further detail in section 2.1.9, where the general theory of rotational Raman scattering is presented in 2.1.4.

The effort required to evaluate the initially mentioned plasma parameters from the recorded scattering signal is relatively low and requires only some rather general assumptions, which are discussed in section 2.1.6. A detailed description of how the parameter evaluation is carried out is outlined in section 2.1.5. The laser scattering technique provides a high spatial resolution and can be considered a non-intrusive one as long as the power of the incident laser radiation is low enough [18, 143]. Possible plasma disturbance by the incident laser radiation is discussed in section 2.1.7. Another aspect that may influence the estimation of plasma parameters, the applicability of the assumption of an incoherent scattering process to the investigated plasma is dealt with in section 2.1.8. Lastly, possible inaccuracy in the estimation of the heavy particle temperature due to a temperature dependence of the Rayleigh scattering cross section is addressed in section 2.1.10.

### 2.1.1 A phenomenological description of light scattering

A static point charge or a point charge moving with a constant velocity, which corresponds to a time constant current in electrical sense, generates a static electric field, i.e. a field without time dependence. However, to emit electromagnetic radiation a time-depentent and location-depentent electric field is needed, so that the time and spatial change in the electric field can sustain a spatial and temporal change in the magnetic field according to Maxwell equations. A time-dependent electric field is only generated by an accelerated charge and thus, as briefly aforementioned, for light scattering to happen the charged particles must be accelerated by the incident laser light [59]. To simplify the following description, firstly only radiation generated by a single electron is discussed. Additionally, since the analyzed case is a non-relativistic one, only the electric field will be considered in the following (more details in Appendix A). Assuming that the incident radiation is a monochromatic sinusoidal electric wave with an angular frequency $\omega_i$, the electron will be accelerated as a reaction to the electric field and will oscillate harmonically with a frequency equal to that of the incident wave creating an electric dipole. An oscillating electric dipole emits radiation itself as schematically shown in Fig. 2.1.

The scattered radiation has a characteristic donut shape, which determines the arrangement of the experimental setup discussed in detail in section 3.3. Since no electric field is radiated along the
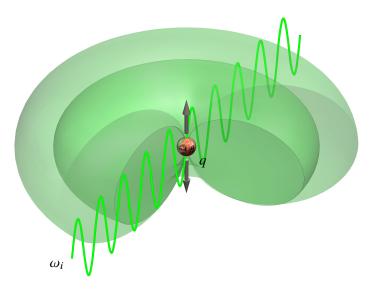
Figure 2.1: The principle of light scattering - a charged particle $q$ is accelerated by the incident electromagnetic wave of frequency $\omega_i$ and creates an electric dipole that oscillates at the same frequency $\omega_i$ of the incident radiation, thereby emitting radiation itself. The emitted radiation has a characteristic, donut-shaped form.

dipole axis and the maximum is reached in the equatorial plane with respect to the axis (see Fig. 2.1), the polarization of the incident laser light should be perpendicular to the propagation direction of the scattered wave to ensure the recording of maximum possible intensity. Hence, the angle between the polarization direction of the laser beam $\vec{E}_i$ and the wave vector of the scattered radiation $\vec{k}_s$ is chosen to be $\varphi = 90°$ in this work. Moreover, another relevant angle is defined between the wave vector of the incident laser radiation $\vec{k}_i$ and the vector $\vec{k}_s$ as depicted in Fig. 2.2. The angle is often referred to as scattering angle and is denoted with $\vartheta$ hereafter.

The scattering particle in a plasma is not static, but moves randomly in space with a thermal velocity $v_{e,th}$. Hence, the angular frequency $\omega_s$ of the scattered light may differ from the incident frequency $\omega_i$ due to a double Doppler shift. On one hand, the frequency which accelerates the scattering particle is shifted from $\omega_i$ due to the particle's velocity component in the direction of the incident radiation. On the other hand, the recorded frequency $\omega_s$ is shifted due to the particle's velocity component in viewing direction. Thus, the higher the thermal velocity of the particles, the spectrally broader the scattered signal becomes. Furthermore, the incident laser beam is spatially extended and actually covers a volume much larger than the size of a single electron as depicted in Fig. 2.3, therefore a large number of particles are accelerated and scatter within that volume. Nonetheless, the scale at which the scattering occurs as well as the scattering volume itself are much smaller than the viewing distance at which the signals are registered in an experimental setup, therefore a far field approximation of the scattered electrical fields is used to simplify the evaluation of the measurements.

Even though the particles in the volume $V$ are positioned randomly (and have a random velocity), the wave vectors $\vec{k}_s$ describing each scattered electromagnetic wave are assumed to have similar direction as a consequence of the far field approximation, but have a slightly shifted frequency due to the aforementioned double Doppler shift. The scattering plasma ensemble within $V$ however still retains its oscillating dipole character, since the polarization and propagation direction of the incident laser beam remain unchanged, therefore the maximal field is registered from the perpendicular viewing direction. The waves radiated by every scattering particle interfere constructively or destructively with each other contributing differently to the resulting total scattered electromagnetic field. If the concentration of particles at a particular position in space, with a specific velocity vector at a given time is described by a distribution function, the total scattering field at one frequency (at a given time)

$$\vec{k} = \vec{k}_s - \vec{k}_i$$
$$\omega = \omega_s - \omega_i$$
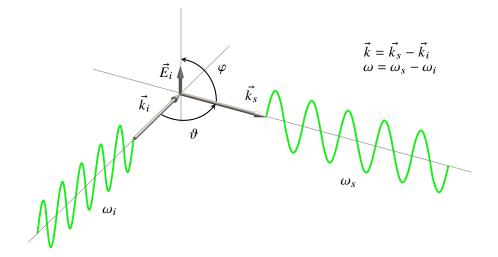
Figure 2.2: Scattering geometry used in this work. The angle $\varphi = 90°$ is chosen to maximize the scattered intensity, whereas the scattering angle $\vartheta = 90°$ is chosen to acquire an incoherent scattering signal.

can be determined by phase-correct addition over the position space of the individual scattering waves. An additional summation over the velocity space provides the distribution of total scattering fields over different frequencies. If a specific distribution function is assumed, usually a Maxwell-Boltzmann distribution for industrial processing plasmas [25], the spectral distribution of the scattering fields can be used to draw conclusions about the plasma parameters. In case of a Maxwellian distribution, if electromagnetic interactions between charged particles within the scattering volume $V$ can be neglected (incoherent scattering), the scattering spectrum has a Gaussian shape with its area being proportional to the absolute particle density $N$ and its width proportional to the square root of $T_e$ [175]. The electron density can be extracted from the absolute particle density under assumption that $n_e$ is constant within the scattering volume.
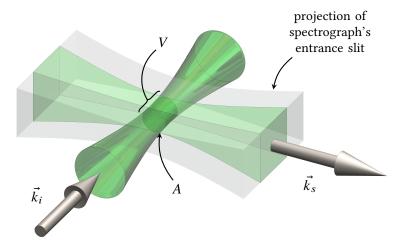


Figure 2.3: The incident power $P_i$ of the laser beam is distributed across an area $A$ which defines the scattering volume $V$.

As a consequence, the mean scattered power $\overline{dP_s}$ over a spectral range $d\omega$ is a function of the total spectral distribution of (free or bound) electrons $s(\vec{k}, \omega)$ within $V$ and, since the scattering depends on the electric field strength of the incident radiation, $\overline{dP_s}$ is also a function of incident power $P_i$. As can be concluded from the above discussion, the spectral distribution function $s(\vec{k}, \omega)$ depends on

the scattering geometry, i.e. on the difference $\vec{k}$ between the wave vector of the incident radiation $\vec{k}_i$ and the wave vector of the scattered radiation $\vec{k}_s$ as well as the difference $\omega$ between the angular frequencies of the incident ($\omega_i$) and scattered ($\omega_s$) radiation. The incident power $P_i$ is distributed across an area $A$, which defines the scattering volume $V$ (see Fig. 2.3). This volume is also defined by the solid angle $\Omega$, since only a part of the scattering signal can be registered from the chosen viewing direction. Concluding, following the approach of Forster [47] and van de Sande [175], for the mean scattered power it can be written

$$\overline{dP}_s = d\omega\ \Omega\ N\ \frac{P_i}{A}\ \sigma\ s(\vec{k}, \omega) \tag{2.1}$$

with $\sigma$ denoting the differential scattering cross section. The scattering cross section can be understood as the probability that scattering will occur within the solid angle $\Omega$ between the incident wave radiation and a plasma particle. Taking into account that $N = n_q V$, with $n_q$ being the density of the charged scattering particles, the above equation can be rewritten in the following form

$$\frac{\overline{dP}_s/_{(d\omega\ \Omega)}}{P_i/_A} = \sigma\ n_q V\ s(\vec{k}, \omega)\ . \tag{2.2}$$

The scattering processes discussed in this work can be described by the last equation.

### 2.1.2 Thomson scattering theory

According to equation (2.2), the ratio of the mean scattered power $\overline{dP}_{s,ThS}$ per frequency interval $d\omega$ and solid angle $\Omega$ to the incident power $P_i$ per surface area $A$ in case of Thomson scattering can be expressed according to

$$\frac{\overline{dP}_{s,ThS}/_{(d\omega\ \Omega)}}{P_i/_A} = \sigma_T\ n_e V\ s_{ThS}(\vec{k}, \omega) \tag{2.3}$$

with $\sigma_T$ indicating the one-particle Thomson scattering cross section and ($n_e V$) standing for the total amount of scatterers, i.e. free electrons, within the scattering volume $V$. The Thomson scattering cross section is given by

$$\sigma_T = (r_e \sin\varphi)^2 \tag{2.4}$$

with $\varphi$ being the angle between the wave vector of the scattered light $\vec{k}_s$ and the polarization direction of the incident laser radiation [47]. As discussed in previous section, $\varphi = 90°$. The classical electron radius $r_e$ is constant and amounts to

$$r_e = \frac{q_e^2}{4\pi\epsilon_0 m_e c_0^2} = 2.818 \times 10^{-15}\ \text{m} \tag{2.5}$$

with $q_e = -1.602 \times 10^{-19}$ C being the electron charge and $m_e = 9.109 \times 10^{-31}$ kg the electron mass. Other constants are the vacuum permittivity $\epsilon_0 = 8.854 \times 10^{-12}$ F/m and the speed of light $c_0 = 2.998 \times 10^8$ m/s [50]. This classical electron radius corresponds to the radial distance $r_e$ where the electrostatic potential energy scale due to the electron charge, $q_e^2/(4\pi\epsilon_0 r_e)$, is equal to the electrons rest energy $m_e c_0^2$ [50]. If incoherent scattering is assumed, the scattered signal is a sum of the contributions of each scattering particle and the spectral distribution function $s_{ThS}(\vec{k}, \omega)$ can be described by a Gaussian function [175]. Hence, it can be written

$$s_{ThS}(\vec{k}, \omega) = s_{ThS,incoh}(\vec{k}, \omega) = \frac{e^{-x_e^2}}{k v_{e,th}\ \sqrt{\pi}} \tag{2.6}$$

with $x_e$ representing the normalized angular frequency deviation from the excitation frequency and $v_{e,th}$ the most probable thermal velocity of electrons. The angular frequency deviation is given by

$$x_e = \frac{\omega_s - \omega_i}{(k v_{e,th})} \tag{2.7}$$

with $\omega_s$ being the angular frequency of the scattered wave and $\omega_i$ the angular frequency of the incident wave [175]. The thermal electron velocity is expressed by

$$v_{e,th} = \sqrt{\frac{2 k_B T_e}{m_e}} \tag{2.8}$$

with $k_B = 1.381 \times 10^{-23}$ J/K being the Boltzmann constant [50]. The parameter $k$ in equations (2.6) and (2.7) depends on the scattering geometry and is calculated as the absolute value of the difference between the wave vector of the scattered radiation $\vec{k}_s$ and the wave vector of incident radiation $\vec{k}_i$

$$k = |\vec{k}_s - \vec{k}_i| \, . \tag{2.9}$$

The above equation can be transformed with $|\vec{k}| = (2\pi/\lambda)$ and $\lambda = \lambda_0 + \Delta\lambda$ according to the following mathematical formalism

$$k^2 = k_s^2 + k_i^2 - 2 k_s k_i \cos\vartheta = \left(\frac{2\pi}{\lambda_0}\right)^2 (2 - 2\cos\vartheta) + C\,(\Delta\lambda)$$
$$= \left(\frac{2\pi}{\lambda_0}\right)^2 \left(4\sin^2\frac{\vartheta}{2}\right) + C\,(\Delta\lambda) \, .$$

Thereafter,

$$k = |\vec{k}_s - \vec{k}_i| \cong \frac{4\pi \sin\left(\frac{\vartheta}{2}\right)}{\lambda_0} \, . \tag{2.10}$$

Herein, $\vartheta$ stands for the scattering angle and in case of incoherent scattering, $\vartheta = 90°$, while the wavelength of the incident laser radiation is denoted by $\lambda_0$. Furthermore, the normalized angular frequency deviation $x_e$ given by equation (2.7) can be transformed into a wavelength dependency. According to [47], after linearization it can be written

$$x_e = \frac{\omega_s - \omega_i}{(k v_{e,th})} \cong \frac{2\pi c_0}{k v_{e,th} \lambda_0^2} (\lambda - \lambda_0) \, . \tag{2.11}$$

Finally, after combining equation (2.11) with equation (2.3) the spectral distribution function of the Thomson signal in case of incoherent scattering is given by

$$s_{ThS,incoh}(\vec{k}, \lambda, \lambda_0) = s_{0,ThS}\, e^{-\left(\frac{\lambda - \lambda_0}{\Delta\lambda_{ThS}}\right)^2} \tag{2.12}$$

with

$$s_{0,ThS} = \frac{2\sqrt{\pi} c_0}{k v_{e,th} \lambda_0^2} \tag{2.13}$$

and

$$\Delta\lambda_{ThS} = \frac{k v_{e,th} \lambda_0^2}{2\pi c_0} \, . \tag{2.14}$$

### 2.1.3 RAYLEIGH SCATTERING THEORY

A similar theoretical approach can be used for non-resonant Rayleigh scattering. The ratio of the mean Rayleigh scattered power $\overline{dP}_{s,RyS}$ per frequency interval $d\omega$ and solid angle $\Omega$ to the incident power $P_i$ per surface area $A$ is given by

$$\frac{\overline{dP}_{s,RyS}/_{(d\omega\ \Omega)}}{P_i/_A} = \sigma_R\ n_h V\ s_{RyS}(\vec{k},\omega) \tag{2.15}$$

with $\sigma_R = 6.26 \times 10^{-32}$ m$^2$/sr indicating the one-particle Rayleigh scattering cross section (see sect. 2.1.10) and $n_h$ the heavy particle density. According to the derivation presented in section 2.1.2 the spectral distribution function of the Rayleigh scattered signal can be expressed by

$$s_{RyS}(\vec{k},\lambda,\lambda_0) = s_{0,RyS}\ e^{-\left(\frac{\lambda-\lambda_0}{\Delta\lambda_{RyS}}\right)^2} \tag{2.16}$$

with

$$s_{0,RyS} = \frac{2\ \sqrt{\pi}c_0}{kv_{h,th}\lambda_0^2} \tag{2.17}$$

and

$$\Delta\lambda_{RyS} = \frac{kv_{h,th}\lambda_0^2}{2\pi c_0}. \tag{2.18}$$

Herein, $k$ denotes the absolute value of the difference between wave vectors $\vec{k}_s$ and $\vec{k}_i$ as defined in equation (2.10) and $v_{h,th}$ is the most probable thermal velocity of the heavy particles, for which can be written

$$v_{h,th} = \sqrt{\frac{2k_B T_h}{m_h}} \tag{2.19}$$

with $T_h$ denoting the temperature and $m_h$ the mass of heavy particles respectively.

### 2.1.4 RAMAN SCATTERING THEORY

The third scattering process, Raman scattering, can be also described in a simplified manner similarly as in the previous sections. In this work only the rotational Raman lines are of particular interest, thus the following description will relate to the emission of rotational lines. For a detailed description it should be referred to [28, 35, 112, 175]. As previously stated, Raman scattering is an inelastic process in which energy is transferred to the interacting plasma particles. Since energy levels within an atom or molecule are quantified, the excess energy gained after an energy changing interaction is associated with emission of a certain discrete wavelength. Due to that, each wavelength of the scattered signal is shifted from the incident laser wavelength depending on the transition, which is described by the rotational quantum number $J$. A single discrete energy transition is hence described by a Dirac delta function at a defined wavelength. The amplitude of the Dirac function $\delta\left(\lambda - \lambda_{J \to J'}\right)$ is determined by the amount of scatterers and the scattering cross section of that specific transition. Thus, the Raman scattering spectrum consists of a sum of individual Dirac delta functions with different amplitudes for all permissible rotational quantum numbers $J$. Accordingly, the ratio of the mean Raman scattered power $\overline{dP}_{s,RaS}$ to the incident power $P_i$ can be written as

$$\frac{\overline{dP}_{s,RaS}/_{(d\lambda\ \Omega)}}{P_i/_A} = \sum_J \sigma_{J \to J'}\ n_J V\ \delta\left(\lambda - \lambda_{J \to J'}\right) \tag{2.20}$$

with $\sigma_{J \to J'}$ denoting the one-particle scattering cross sections for a Raman transition between rotational energy states $J$ and $J'$ and $n_J$ being the density of particles in the initial rotational state $J$. The energy of each rotational state $J$ can be calculated for nitrogen molecules approximately as

$$E_J = BJ(J+1) \tag{2.21}$$

with $B$ standing for the rotational constant. The rotational constant for the ground state of a nitrogen molecule is given by

$$B = \frac{h^2}{8\pi^2 q_e \mu R_{bond}^2} \cong 2.48 \times 10^{-4} \text{ eV} \tag{2.22}$$

with $h = 6.626 \times 10^{-34}$ J s being the Planck's constant, $\mu$ the reduced mass of a molecule and $R_{bond}$ the bond length [145]. In case of nitrogen, which is used as plasma gas in this work, these parameters are equal to

$$\mu = \frac{m_N^2}{m_N + m_N} = 1.163 \times 10^{-26} \text{ kg}, \quad R_{bond} = 1.1 \times 10^{-10} \text{ m}.$$

For rotational Raman scattering only $J \to (J \pm 2)$ transitions are allowed [28], where both $J$ and $(J \pm 2)$ are positive, and hence the characteristic wavelengths can be written as

$$\lambda_{J \to J+2} = \lambda_0 + \frac{\lambda_0^2}{hc_0} B(4J+6) \;, \tag{2.23}$$

$$\lambda_{J \to J-2} = \lambda_0 - \frac{\lambda_0^2}{hc_0} B(4J-2) \;. \tag{2.24}$$

Depending on the internal structure, molecules can react differently to an external electric field. Similarly to a charged particle, a dipole moment is induced as a result of this reaction. The way in which a molecule reacts to an external electric field is defined as polarisability. Since the polarisability, and thus the induced dipole moment, depend on the orientation of the molecule, the polarisability is described by a tensor rather than a constant. The tensor is determined by a mean molecular polarisability $\alpha$, since $n_J$ randomly oriented molecules are present in the scattering volume $V$, and by the anisotropy $\gamma$. A more detailed description regarding the polarisability tensor of molecules can be found in [112]. The differential Raman scattering cross section $\sigma_{J \to J'}$ for a $J \to J'$ transition in case of a perpendicular scattering arrangement ($\vartheta = 90°$ and $\varphi = 90°$), is given according to Penney [145] by

$$\sigma_{J \to J'} = \frac{64\pi^4}{45\epsilon_0^2} b_{J \to J'} \frac{\gamma^2}{\lambda_{J \to J'}^4} \;, \tag{2.25}$$

where $\gamma$ denotes the polarisability anisotropy and $b_{J \to J'}$ indicates the Placzek-Teller coefficients. The coefficients for respective rotational Raman transitions as stated in [145] are calculated followingly

$$b_{J \to J+2} = \frac{3(J+1)(J+2)}{2(2J+1)(2J+3)} \;, \tag{2.26}$$

$$b_{J \to J-2} = \frac{3J(J-1)}{2(2J+1)(2J-1)} \;. \tag{2.27}$$

According to equation (2.25) the rotational Raman scattering cross section depends only on the polarisation anisotropy $\gamma$. For nitrogen and an incident laser wavelength of $\lambda_0 = 532$ nm the squared anisotropy value was approximated by van de Sande [175] and amounts to

$$\gamma^2 = (0.395 \pm 8\%) \times 10^{-82} \text{ F}^2\text{m}^4 \;.$$

Finally, an equation has to be established for the density $n_J$ of particles in the initial rotational state $J$ in order to calculate the ratio of the mean Raman scattered power $\overline{dP_{s,RaS}}$ to the incident power $P_i$ according to equation (2.20). The density $n_J$ is given by

$$n_J = \frac{n_{N_2}}{Q} \, g_J (2J + 1) \, \mathrm{e}^{-\frac{E_J}{k_B T_h}} \,. \tag{2.28}$$

Herein, $n_{N_2}$ is the density of molecular nitrogen, $g_J$ the degeneracy and $Q$ the rotational partition function. In case of nitrogen, the degeneracy is $g_J = 6$ for even rotational numbers $J$ and $g_J = 3$ for odd $J$ respectively, whereas the rotational partition function $Q$ can be approximated according to [175] with

$$Q \cong \frac{9 k_B T_h}{2B} \,. \tag{2.29}$$

### 2.1.5 FROM THEORY TO PRACTICE - DETERMINATION OF PLASMA PARAMETERS FROM MEASURED DATA

The spectral distribution function does not in general correspond exactly to the experimentally measured scattering signal. The registered signal at (for instance) the detector, an image intensified charge coupled device (ICCD) camera, depends not only on the spectral sensivity of the imaging sensor, but also on the sensitivity of the experimental setup and on the spectrometer's transfer function. Hence, for the measured signal $M(\lambda^*)$ it can be written

$$M(\lambda^*) = K \int S(\lambda) \, S_F(\lambda - \lambda^*) \, d\lambda \,, \tag{2.30}$$

where $S(\lambda)$ being the scattered light spectrum, $K$ the detection sensitivity of the experimental setup assumed to be independent of the wavelength and $S_F$ is denoting the transfer function of the setup. The detection sensitivity $K$ takes into account the spectral response of all setup components, i.e. the spectral sensitivity of the ICCD, the lenses, mirrors and spectrometer used. Since the spectral range of the scattering signal is usually smaller than 20 nm [20, 28, 70], the sensitivity $K$ is furthermore assumed to be constant within this range. Both parameters, the detection sensitivity $K$ and transfer function $S_F$, can be determined by measuring light scattered by a reference object (medium) with known properties. Rayleigh scattering of pure nitrogen at room temperature and atmospheric pressure can be used for this purpose. The main parameters determining the scattering spectrum are the temperature of heavy particles $T_h$ and the heavy particle number density $n_h$, which is obtained for the above conditions from the ideal gas law

$$n_h = \frac{p}{k_B T_h} \tag{2.31}$$

with $p = 1.013 \times 10^5$ Pa denoting the atmospheric pressure. If a ratio is formed between the wavelength shift of the Thomson scattered signal and wavelength shift of the Rayleigh scattered signal, according to equations (2.14) and (2.18)

$$\frac{\Delta \lambda_{ThS}}{\Delta \lambda_{RyS}} = \sqrt{\frac{m_h}{m_e}} \cong \sqrt{\frac{4.65 \times 10^{-26}}{9.11 \times 10^{-31}}} \cong 226 \,, \tag{2.32}$$

it can be immediately recognized that for a thermal equilibrium (i.e. $T_h = T_e$) the spectral line width of the Rayleigh scattered signal will be much narrower (approx. 226 times) than that of the Thomson signal. Since thermal equilibrium can be assumed for room temperature under atmospheric pressure conditions, the spectral line width of the Rayleigh scattered signal is in the range of picometers [121]. The resolution of the used spectrometer however amounts to approx. 0.055 nm/$px$ for an entrance slit

width of 150 μm and consequently linewidths in picometer cannot be resolved (see sect. 3.3). Hence, for the spectral distribution function expressed by equation (2.16) a Dirac delta function can be assumed

$$s_{RyS}(\vec{k}, \lambda, \lambda_0) = s_{0,RyS}\, \mathrm{e}^{-\left(\frac{\lambda-\lambda_0}{\Delta\lambda_{RyS}}\right)^2} \cong \delta\left(\lambda - \lambda_0\right) . \tag{2.33}$$

According to the above discussion, the following relation can be written for the measured Rayleigh scattered signal

$$M_{RyS}(\lambda^*) = \sigma_R\, n_h V\, K \int \delta(\lambda - \lambda_0)\, S_F(\lambda - \lambda^*)\, d\lambda \tag{2.34}$$

or equivalently

$$M_{RyS}(\lambda^*) = \sigma_R\, n_h V\, K\, S_F(\lambda^*) . \tag{2.35}$$

Assuming that the transfer function $S_F(\lambda^*)$ is normalized to 1, in case of $\lambda^* = \lambda_0$ the above equation can be solved for the detection sensitivity $K$ yielding

$$K = \frac{M_{RyS}(\lambda^* = \lambda_0)}{\sigma_R\, n_h V} . \tag{2.36}$$

Accordingly the transfer function of the whole detection apparatus, which is mainly determined by the transfer function of the spectrometer, is given by

$$S_F(\lambda^*) = \frac{M_{RyS}(\lambda^*)}{\sigma_R\, n_h V\, K} . \tag{2.37}$$

In case of incoherent scattering, the Thomson scattering spectrum can be written according to equation (2.12) as

$$M_{ThS}(\lambda^*) = \sigma_T\, n_e V\, K \int s_{0,ThS}\mathrm{e}^{-\left(\frac{\lambda-\lambda_0}{\Delta\lambda_{ThS}}\right)^2} S_F(\lambda - \lambda^*)\, d\lambda . \tag{2.38}$$

By combining equation (2.38) with (2.36) the measured Thomson scattered signal is obtained as the following convolution

$$M_{ThS}(\lambda^*) = \frac{\sigma_T\, n_e}{\sigma_R\, n_h}\, M_{RyS}(\lambda^* = \lambda_0) \int s_{0,ThS}\mathrm{e}^{-\left(\frac{\lambda-\lambda_0}{\Delta\lambda_{ThS}}\right)^2} S_F(\lambda - \lambda^*)\, d\lambda . \tag{2.39}$$

If the spectral width of the transfer function $S_F$ is significantly smaller than the spectral width of the Thomson scattered spectrum $s_{0,ThS}$, then the convolution integral, which represents the spectral distribution of the measured signal $M_{ThS}$, is accurately reproduced by a Gaussian distribution function. Hence,

$$\int s_{0,ThS}\, \mathrm{e}^{-\left(\frac{\lambda-\lambda_0}{\Delta\lambda_{THS}}\right)^2} S_F(\lambda - \lambda^*)\, d\lambda = m_{0,ThS}\, \mathrm{e}^{-\left(\frac{\lambda^*-\lambda_0}{\Delta\lambda_{m,ThS}}\right)^2} . \tag{2.40}$$

Thereafter, the electron temperature $T_e$ can be determined from the characteristic width $\Delta\lambda_{m,ThS}$ of the measured signal fitted by a Gaussian curve. In addition, the electron density $n_e$ can be determined by rearranging the equation

$$M_{ThS}(\lambda^* = \lambda_0) = \frac{\sigma_T\, n_e}{\sigma_R\, n_h}\, M_{RyS}(\lambda^* = \lambda_0)\, m_{0,ThS} \tag{2.41}$$

to

$$n_e = \frac{M_{ThS}(\lambda^* = \lambda_0)}{M_{RyS}(\lambda^* = \lambda_0)}\, \frac{\sigma_R}{\sigma_T}\, n_h\, \frac{1}{m_{0,ThS}} . \tag{2.42}$$

### 2.1.6 LASER SCATTERING ASSUMPTIONS

Several simplifying assumptions need to be made, prior to applying the theory of electromagnetic scattering presented in the sections above to the registered signal. These assumptions are discussed in the following.

- The incident electromagnetic wave propagates undamped through a plasma when its frequency $\omega_i$ is much higher than the plasma frequency $\omega_p$ of the plasma's free electrons. By satisfying this condition, it is assumed that the electrons are not shielding the oscillating electric field of the incident wave.

- According to the condition above, due to the timescale differences, the plasma is assumed to be collision-less during the short time window of the scattering process.

- Relativistic effects are neglected, since electron velocity is much lower than the speed of light ($v_{e,th} \ll c_0$). Therefore the effect due to the magnetic field of the incident radiation is also neglected (see Appendix A).

- The power of incident radiation (i.e. the electric field strength) is sufficiently low so that it does not modify the ionization degree of the plasma.

- Scattering on (positive or negative) ions is not considered due to their much higher mass and hence much reduced scattered power compared to that by the free electrons.

- It is assumed that the distance from the scattering location to the detector is considerably greater than the incident wavelength $\lambda_i$, as well as the distance traveled by the electron during scattering and the dimensions of the scattering volume. Therefore it is assumed that only scattered signal is detected in the far field approximation.

- The laser light used in the experiment is assumed to be monochromatic and linearly polarized.

In order to assess whether the above assumptions are satisfied, the relevant variables must theoretically estimated. The plasma frequency $\omega_p$ can be calculated for different electron densities as given by Chen [24]

$$\omega_p = \sqrt{\frac{n_e \, q_e^2}{m_e \, \epsilon_0}}, \tag{2.43}$$

whereas the laser frequency $\omega_i$ is constant and amounts for the used laser to

$$\omega_i = \frac{2\pi c_0}{\lambda_0} = 3.54 \times 10^{15} \text{ s}^{-1}. \tag{2.44}$$

Both values are compared for a wide range of $n_e$ in Fig. 2.4. As can be seen no noticeable shielding of the incident radiation occurs since $\omega_p$ is significantly lower than $\omega_i$. The collision frequency of electrons with other plasma particles is also given by Chen with

$$\omega_{coll} = 2\pi n_e \, \sigma_{coll} \, v_{e,th}. \tag{2.45}$$

Herein $\sigma_{coll}$ denotes the collision cross section, for which can be written

$$\sigma_{coll} = \left( \frac{\pi \, q_e^2}{4\epsilon_0 \, k_B \, T_e} \right)^2. \tag{2.46}$$

The collision frequency is calculated for a wide range of $n_e$ and $T_e$ and plotted in Fig. 2.5, where the laser frequency is marked as a translucent surface. According to the results, the electrons collide far less frequently than the frequency of the incident laser radiation and hence plasma can be assumed to be collision-less during the scattering process within the evaluated value range.
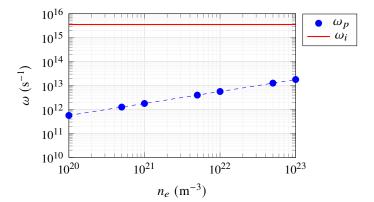
Figure 2.4: The plasma frequency $\omega_p$ is significantly lower than laser frequency $\omega_i$ within a wide range of electron density, hence the incident electromagnetic radiation propagates undamped through the plasma.
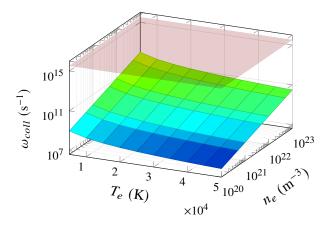


Figure 2.5: The collision frequency $\omega_{coll}$ is significantly lower than the laser frequency $\omega_i$ (translucent surface) within the evaluated range of $n_e$ and $T_e$, hence the plasma can be assumed to be collision-less during the scattering.

### 2.1.7 Possible error sources - laser heating

According to the assumptions discussed in section 2.1.6 the power of the incident radiation plays an important role and should be chosen carefully. The power should be high enough to maximize the scattering signal, but low enough not to locally modify the plasma. Especially when analyzing plasmas with low ionization degrees the laser beam can disturb the gas species and hence cause invalid measurement results. Murphy, who investigated thermal plasmas under atmospheric conditions in [126, 127], stated that incident laser radiation can be an effective heating source of electrons by means of inverse bremsstrahlung induced by electron-ion interaction. The change in electron temperature due to laser heating can be estimated for plasmas close to local thermal equilibrium and with an electron density higher than $10^{21}$ m$^{-3}$ as proposed by Kunze [101]. According to Carbone *et al.* [18, 19] however, for non-thermal plasmas with low ionization degrees not only the electron-ion interaction but also the electron-atom interaction should be considered. The authors proposed a method to determine a critical laser fluency (energy per area) for which laser heating does not take place and validated it for a non-thermal argon plasma. In order to determine the laser fluency, the dissociation and ionization rate coefficients for both electron-ion and electron-atom interactions need to be known. Due to the molecular nature of nitrogen gas, far more interaction channels exist between the electrons and neutral molecules and hence the rate coefficients are significantly higher than for atomic gases such as argon. Nonetheless, according to Cacciatore *et al.* these interaction channels,

which are governed by the exitation cross sections, are of relevance for electron energies higher than 5 eV [17] and therefore can be neglected for the plasma investigated within this work since lower electron energies are expected. The laser perturbation can thus be estimated considering only electron-ion interactions, similarly to [175]. According to van de Sande [175], the relative change in electron temperature $T_e$ caused by the laser beam is approximated by

$$\frac{\Delta T_e}{T_e} \cong 3.38 \times 10^{-39} \frac{n_{h,i} Z^2}{(k_B T_e)^{3/2}} Q_0 \lambda_0^2 \left(1 - \mathrm{e}^{-\frac{\hbar \omega_i}{k_B T_e}}\right)$$

with $n_{h,i}$ being the ion density and $Z$ the charge number of ions. The laser frequency is denoted with $\omega_i$ according to equation (2.44), whereas $Q_0$ denotes the incident laser energy per area. Assuming that the laser radiation does not affect the absorption coefficient of the plasma, a wavelength of $\lambda_0 = 532$ nm, a pulse energy of 0.3 J and a diameter of the laser spot of 200 μm yields a $Q_0 = 9.5 \times 10^6$ J/m$^2$. Assuming further $Z = 1$ and $n_{h,i} = n_e$, the relative temperature increase $\Delta T_e / T_e < 0.025$ for electron densities in the range of $10^{21}$ m$^{-3}$ and electron temperatures in the range of 40000 K. Thereafter, the laser heating is in theory negligible.

Apart from the theoretical estimation, Muraoka *et al.* proposed an experimental evaluation of the plasma perturbation by laser radiation, which can be performed by comparing measurement results taken with different laser power settings [122]. The laser heating can thus be considered
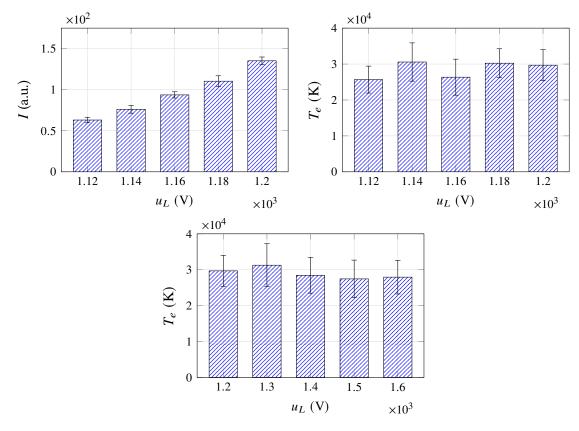


Figure 2.6: Experimental evaluation of the plasma perturbation by laser radiation. The power of the incident laser radiation increases with rising flash lamp voltage $u_L$. Nevertheless, no significant changes are observed in the estimated electron parameters for a wide range of lamp voltages $(1.12 - 1.60$ kV$)$, thus the laser is assumed not to perturb the plasma.

negligible in a certain power range if the measured scattering signals display nearly the same strength at different power levels within the considered power range. According to section 2.1.5, the electron

temperature is much more sensitive to variation of the registered signal, since it is derived directly from the characteristic width of the Gaussian fit. Therefore the electron temperature is used in the following evaluation.

As the laser power is controlled by the voltage of the pumping flash lights $u_L$, measurements for different voltages are shown in Fig. 2.6. The plasma generator settings as well as other parameters, such as exposure time and gain voltage of the image intensifier, are kept constant during these measurements. An increase in flash lamp voltage from 1.12 kV to 1.20 kV resulted in a doubling of the recorded intensity amplitude, as can be seen in Fig. 2.6. Although the recorded intensity varies, the electron temperature $T_e$ values fluctuate insignificantly within the measurement accuracy. Thus, further measurements are conducted for increased flash lamp voltages of up to 1.60 kV, what corresponds to a multiplication of the incident laser radiation intensity by a factor of 2.62 compared to 1.20 kV. The calculated electron temperature values confirm previous results and change only insignificantly. It should be noted, that the gain of the image intensifier module had to be reduced for lamp voltages higher than 1.20 kV. In summary, the results prove that the plasma examined within this work is not perturbed by the incident laser radiation within the evaluated power range.

### 2.1.8 Taking into account the interaction between scatterers

While discussing the theory of laser scattering in previous sections, the electromagnetic interactions between charged particles within the scattering volume have been neglected. This can be done when the scattering electrons are distributed randomly within the scattering volume, which is expected if the scatterers are in thermodynamic equilibrium [50]. A random positioning allows the registered signal to be considered as a sum of scattered powers of individual particles and more importantly, the shape of the signal corresponds to the electron velocity distribution. Hence, the interpretation of incoherent scattering signals is rather straightforward when compared to other diagnostic methods [124]. If however the positions of scattering electrons are correlated, due to periodic plasma density fluctuations or other plasma instabilities, the phases of the scattered waves can interfere and increase or decrease the intensity of the signal depending on the propagation direction. On a microscopic scale, charged particles in a plasma are always coupled within a certain sphere defined by the Debye radius $\lambda_D$. According to [83], electrons inside a sphere of a radius $\lambda_D$ oscillate with a wavelength $\lambda_F$. If the wavelength $\lambda_F \gg \lambda_D$ the electrons oscillate in phase and emit a coherent scattered signal. In the case $\lambda_F \ll \lambda_D$ the electron density oscillation can be considered random on this length scale and the scattered signal contains no coherent contribution. The exact influence of the coherent scattering is extensively discussed in [50], based on the so called Salpeter approximation of the spectral distribution function $s(\vec{k}, \omega)$. The first term of the approximated function, $s_{e,e}(\vec{k}, \omega)$, considers only the interactions between free electrons, whereas the second term $s_{e,h}(\vec{k}, \omega)$ considers the interactions between free electrons and other charged particles. Assuming that $T_e \geq T_h$ and $m_e \ll m_h$, the Salpeter approximation can be reduced after [47] to

$$s\left(\vec{k}, \omega\right) = s_{e,e}\left(\vec{k}, \omega\right) + s_{e,h}\left(\vec{k}, \omega\right) =$$

$$= \frac{1}{k v_{e,th} \sqrt{\pi}} \left| \frac{1}{1 + \alpha^2 \underline{g_e}} \right|^2 e^{-\left(x_e^2\right)} + \frac{Z}{k v_{h,th} \sqrt{\pi}} \left| \frac{\alpha^2}{1 + \alpha^2 \left(1 + \underline{g_h}\right)} \right|^2 e^{-\left(x_h^2\right)} \tag{2.47}$$

with $Z$ denoting the charge number, and $g_e$ and $g_h$ denoting complex functions depending on velocity distributions of electrons and ions respectively. The symbols $x_e$ and $x_h$ correspond to the angular frequency deviation normalized with electron and heavy particle thermal velocity, $v_{e,th}$ and $v_{h,th}$ as expressed by equations (2.7) and (2.8). The difference between scattered and incident wave vectors $\vec{k}$ is expressed by equation (2.10). Furthermore, the Salpeter approximation introduces the scattering

parameter $\alpha$, for which it can be written

$$\alpha \equiv \frac{\lambda_F}{2\pi\lambda_D} = \frac{1}{k\lambda_D} \cong \frac{1}{4\pi \sin\left(\frac{\vartheta}{2}\right)} \frac{\lambda_0}{\lambda_D} \tag{2.48}$$

with $\vartheta$ being the scattering angle and $\lambda_0$ the incident laser wavelength. By calculating the Debye radius with

$$\lambda_D = \sqrt{\frac{\epsilon_0\, k_B\, T_e}{q_e^2\, n_e}}, \tag{2.49}$$

the influence of coherent effects can be estimated. According to equation (2.47), if $\alpha$ is much smaller than unity, then

$$s_{e,h}\left(\vec{k}, \omega\right) \cong 0, \text{ as well as } \left|\frac{1}{1 + \alpha^2\, \underline{g_e}}\right|^2 \cong 1\,.$$

According to the above, if the function $s_{e,h}\left(\vec{k}, \omega\right)$ considering the interactions between electrons and ions is negligible, only the function considering the interactions between free electrons among themselves remains. The latter is also negligible since $\lambda_0 \ll \lambda_D$. Therefore, the spectral distribution function $s(\vec{k}, \omega)$ is Gaussian shaped due to the factor $e^{-\left(x_e^2\right)}$ and dependent only on the electron velocity distribution function - the scattering process is incoherent. Coherent effects increase and must be taken into account for $\alpha$ values near unity or higher [50].

As indicated by equations (2.48) and (2.49) the scattering parameter $\alpha$ is directly proportional to the electron density $n_e$ and inversely proportional to the electron temperature $T_e$. For the experimental setup ($\vartheta = 90°$, $\lambda_0 = 532$ nm) two case studies are analyzed to assess the effect of coherent scattering. In the first one, the electron density is kept constant at $n_e = 3.0 \times 10^{21}$ m$^{-3}$ and the electron temperature varies. In the second case $T_e$ is kept constant at 30000 K and $n_e$ is varied. As can be seen in Fig. 2.7, the calculated scattering parameter $\alpha$ is smaller than unity in both cases, slightly lower than 0.3 in the expected range of $T_e$ and $n_e$ indicating a weak coherent component in the spectral distribution function. When compared with an incoherent spectrum, this can lead to an underestimation of the electron density by about 7% and overestimation of the electron temperature by about 21% as suggested by [175].
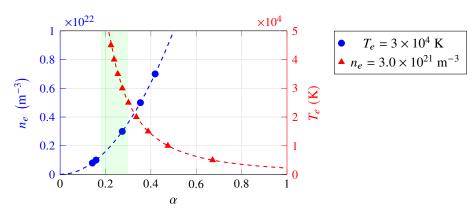


Figure 2.7: Case study to assess the behavior of the scattering parameter $\alpha$ in the expected value range of the plasma parameters. First case (blue): constant $T_e$, variable $n_e$. Second case (red): constant $n_e$, variable $T_e$.

### 2.1.9 Influence of Raman scattering on the Thomson scattering signal

Spectral ranges of rotational Raman scattering and Thomson scattering signals overlap. This feature can provide additional information about the measurement object allowing the determination of

rotational temperature of the scattering particles [176] or can be used for an absolute calibration of the experimental setup [175]. According to Narishige *et al.* [133], an overlap occurs when the total density of Raman scattering particles $n_J > 10^4$ times larger than electron density, since Raman scattering cross sections are about $10^{-5}$ times smaller than the Thomson scattering cross section at the used laser wavelength. Due to the spectral range overlapping, the registered signal $M(\lambda^*)$ given previously by equation (2.30) can be considered as a sum of both signals resulting in

$$M(\lambda^*) = M_{ThS}(\lambda^*) + M_{RaS}(\lambda^*) . \tag{2.50}$$

Herein, $M_{ThS}(\lambda^*)$ is given by equation (2.38) and for $M_{RaS}(\lambda^*)$ can be written correspondingly

$$M_{RaS}(\lambda^*) = \sum_J \sigma_{J \to J'} \, n_J V \, K \int \delta \left( \lambda - \lambda_{J \to J'} \right) S_F(\lambda - \lambda^*) \, d\lambda . \tag{2.51}$$

Combining the above equation with equation (2.36) yields

$$M_{RaS}(\lambda^*) = \sum_J \frac{\sigma_{J \to J'} \, n_J}{\sigma_R \, n_h} \, M_{RyS}(\lambda^* = \lambda_0) \int \delta \left( \lambda - \lambda_{J \to J'} \right) S_F(\lambda - \lambda^*) \, d\lambda . \tag{2.52}$$

According to the above considerations, both $M_{ThS}(\lambda^*)$ and $M_{RaS}(\lambda^*)$ signals can be put into relation as they are calibrated with the Rayleigh scattering signal.

Hence, the influence of rotational Raman scattering is estimated by comparing the experimentally measured signals of $M_{RyS}(\lambda^*)$ and $M_{ThS}(\lambda^*)$ with the calculated $M_{RaS}(\lambda^*)$ signal. As presented in section 2.1.4 and practically demonstrated in Appendix B, the temperature of heavy particles is needed to calculate the intensity of rotational Raman scattering signal. This temperature is determined from the experiments and amounts to $T_h = 3500$ K for the data set presented in Fig. 2.8.
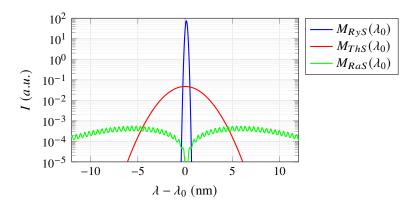


Figure 2.8: Comparison of signal intensities of the measured Rayleigh $M_{RyS}(\lambda_0)$ and Thomson $M_{ThS}(\lambda_0)$, and the calculated Raman $M_{RaS}(\lambda_0)$ spectra. The heavy particle temperature needed for the calculation of $M_{RaS}(\lambda_0)$ is determined from the experimentally measured $M_{RyS}(\lambda_0)$ and $M_{ThS}(\lambda_0)$ signals and amounts to $T_h = 3500$ K.

Thereafter, the rotational Raman scattering spectrum presented in Fig. 2.8 is calculated for a given heavy particle temperature and a known spectrometer transfer function. As can be observed, the experimentally measured Thomson scattering signal is three orders of magnitude smaller than the measured Rayleigh signal, whereas the calculated rotational Raman spectrum is approximately two orders of magnitude smaller than the Thomson signal. Furthermore, the intensity of the $M_{RaS}(\lambda_0)$ signal decreases with increasing $T_h$, while the spectral range becomes broader, as shown by the additional calculations for three different $T_h$ values in Fig. 2.9. Taking into account the decrease in intensity with increasing temperature of the heavy particles, since the scattering particles are more separated from each other, as well as the intensity differences between the respective spectra (see
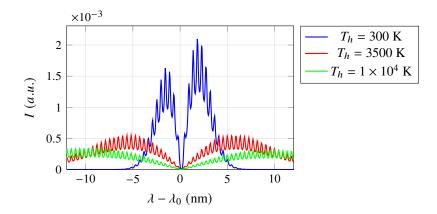
Figure 2.9: Rotational Raman spectra calculated for three different heavy particle temperatures. The intensity decreases with increasing temperature, while the spectral range expands.

Fig. 2.8), it is thus assumed that the rotational Raman signal does not significantly influence the Thomson scattering signal and hence the determined plasma parameters. Due to the low intensity of the Raman spectrum it is also hardly possible to determine the rotational temperature or perform an absolute calibration of the experimental setup.

### 2.1.10 Temperature dependence of the Rayleigh scattering cross section

Apart from calibration reasons, the Rayleigh scattering signal is used to determine the heavy particle temperature $T_h$. This is performed by relating the particle density $n_h$ to $T_h$ through the ideal gas law according to equation (2.31). To determine $T_h$ the intensity of the Rayleigh scattering signal $I_T$, measured while the plasma is turned on, is normalized with the reference intensity of the Rayleigh signal $I_0$ measured for pure nitrogen at room temperature. This can be easily done since the experimental setup allows both signals to be registered without physically changing the setup or even without changing the ICCD settings. According to equation (2.35), for the normalized intesity it can be written

$$\frac{I_T}{I_0} = \frac{M_{RyS,T}}{M_{RyS,0}} = \frac{\sigma_{RyS,T}\, n_{h,T}}{\sigma_{RyS,0}\, n_{h,0}}\ . \tag{2.53}$$

Combining the above equation with the ideal gas law given by equation (2.31), under assumption that the Rayleigh scattering cross section is temperature independent, allows a direct determination of $T_h$, since

$$T_h = \frac{I_0}{I_T} \frac{\sigma_{RyS,T}}{\sigma_{RyS,0}} T_0 \cong \frac{I_0}{I_T} T_0 \tag{2.54}$$

with $T_0 = 293\ K$ denoting the room temperature.

However, the Rayleigh scattering cross section $\sigma_R$ is temperature dependent and can hence influence the estimation of $T_h$. According to Limbach *et al.* [108] a temperature dependence is particularly relevant for molecular gases, where $\sigma_R$ additionally increases with rising $T_h$ due to the rotational and vibrational energy states compared to atoms or ions. The Rayleigh cross section is a function of the molecular polarisability $\alpha$ and the polarisation anisotropy $\gamma$, as was the case with the Raman scattering cross section (compare sect. 2.1.4). After [108] for $\sigma_{RyS,T}$ it can be written

$$\sigma_{RyS,T} = \frac{16\pi^4}{\lambda_0^4} \left( \alpha(T)^2 + \frac{7}{45}\gamma(T)^2 \right) . \tag{2.55}$$

Limbach *et al.* also defined a temperature dependence coefficient $\kappa_\sigma = 4.6 \times 10^{-4}$ %/K, which can be used to estimate the Rayleigh scattering cross section at $T_h$ according to following equation

$$\frac{\sigma_{RyS,T} - \sigma_{RyS,0}}{\sigma_{RyS,0}} = \kappa_\sigma (T_h - T_0) \tag{2.56}$$

with $\sigma_{RyS,0} = 6.26 \times 10^{-32}$ m$^2$/sr denoting the Rayleigh scattering cross section at room temperature. If a heavy particle temperature of $T_h = 6000$ K is assumed as an example, the cross section increases according to equation (2.56) about 2.6% to $\sigma_{RyS,T} = 6.42 \times 10^{-32}$ m$^2$/sr, what results in a similar percentual increase of $T_h$ according to equation (2.54). Correspondingly, for the expected temperature range it can be assumed that by neglecting the temperature dependence of the Rayleigh cross section the measured values are underestimated by about 5% or lower. Since such a small underestimation cannot be detected by other (spectroscopic) diagnostic methods in this work, the temperature dependence is not considered and the symbol $\sigma_{RyS}$ refers to the scattering cross section at room temperature in the following.

## 2.2 Optical emission spectroscopy

Spectroscopy is probably one of the oldest diagnostic tools with its foundations laid by the pioneers of modern physics beginning at the end of the 19th century [171]. It is also one of the most established and continuously developing methods of plasma diagnostics since the first publications by Griem [56, 57] and Cooper [31]. It allows, simply put, to gather information about the composition and energy state of the plasma by analyzing the emitted radiation. The simplest type of spectroscopy is called emission spectroscopy. Here the electromagnetic radiation emitted by the plasma is recorded with spectral resolution and subsequently interpreted to obtain characteristic parameters such as density or temperature of the radiating atoms, ions and molecules. Optical emission spectroscopy is a non-invasive method, since the analyzed plasma is not disturbed by any external fields, electric potentials or probes. Additionally, real-time observation is possible which can be used not only as a diagnostics for R&D applications, but also as a monitoring tool for production processes [25]. Usually the emitted spectrum can be recorded fairly easy, but the interpretation is complex, especially for non-equilibrium plasmas [46], and is often connected with modelling to explain the observed effects [71, 137].

Several other spectroscopy techniques are used for plasma diagnostics. However, for their description, it should be referred to corresponding publications, such as for ex. [37], as only optical emission spectroscopy is used in this work to provide further information about the investigated pulsed low-current discharge. Thereafter, a short description of basic concepts and phenomena of emission spectroscopy is first given in section 2.2.1, followed by a more detailed description of the broadening of hydrogen lines due to Stark effect in section 2.2.2, from which the electron density is estimated. In section 2.2.4 emission of molecular spectra is discussed, whereas section 2.2.5 presents methods to estimate rotational and vibrational temperatures from these spectra. The theory and phenomena discussed in the above mentioned sections are mainly based on works of Griem [56, 57], Thorne [171], Kunze [102] and Demtröder [36]. Reference should be made to these sources for any further details.

### 2.2.1 Basics of emission spectroscopy

As a direct consequence of Heisenberg's uncertainty principle, the electrostatic attraction to the positively charged nucleus makes bound electrons within an atom have discrete energy levels. When such atom interacts with some external energy source, like radiation or an electric current (if the considered atoms form part of an electric conducting material or medium), the atom's bound electrons are excited to higher energy levels, such that when the excited electron returns to a stronger bounded state, radiation of a definite discrete energy is emitted. The final state to which the excited electron returns may be different then the energy state before the excitation took place.

In the following discussion let $i$ denote the initial excited energy state and $f$ the final, less excited energy state with $\lambda_{if}$ being the wavelength emitted by the bound electron due to the transition $i \rightarrow f$. Accordingly $\omega_{if} = \dfrac{2\pi c_0}{\lambda_{if}}$ denotes the (angular) frequency of the emitted radiation. The energy of an emitted photon is thereafter equal to

$$E_i - E_f = \hbar\,\omega_{if} \tag{2.57}$$

with $\hbar = h/(2\pi)$ being the reduced Planck constant. According to the above equation only a certain energy difference causes radiation to be emitted in the visible spectral range, mostly originating from a transition between the excited states [46]. In principle the emitted radiation $\hbar\,\omega_{if}$ would correspond to a sharp, infinitesimally narrow, wavelength. However, also as a consequence of Heisenberg's uncertainty principle which connects the energy uncertainty $\Delta E$ with the lifetime $\Delta t$ of the excited state, the energy of the original sharp wavelength is distributed over a narrow spectral interval. This effect is referred to as natural broadening. The intensity of the emitted wavelength characteristic for the radiating particle is quantified by the transition dependent emission coefficient $\varepsilon_{if}$

$$\varepsilon_{if} = n_{q,i}\,A_{if}\,\frac{\hbar\,\omega_{if}}{\Omega} = \int_0^\infty \varepsilon_\omega\,d\omega\,, \tag{2.58}$$

where $n_{q,i}$ denotes the density of particles in the initial excited state, $A_{if}$ the transition probability from $i$ to $f$ also referred to as Einstein coefficient, $\Omega$ being the solid angle and $\varepsilon_\omega$ the spectral line emission coefficient. For $\varepsilon_\omega$ it can be written

$$\varepsilon_\omega = \varepsilon_{if}\,I(\omega) \quad \text{with} \quad \int_0^\infty I(\omega)\,d\omega = 1 \tag{2.59}$$

and $I(\omega)$ being the normalized line profile intensity. The normalized intensity profile of a natural broadened line centered at $\omega_0$ is represented by a Lorentzian distribution function

$$I(\omega) = \frac{\Delta\omega_L/(2\pi)}{(\omega - \omega_0)^2 + (\Delta\omega_L/2)^2} \quad \text{with} \quad \int_0^\infty I(\omega)d\omega = 1\,, \tag{2.60}$$

where $\Delta\omega_L$ is the full width at half maximum of the profile (short FWHM), often referred to as natural line width. The spectral interval over which the energy is distributed in the visible wavelength range is normally several orders of magnitude smaller than in other broadening mechanisms [171]. Therefore, the influence of natural broadening on the recorded line shape is usually assumed not to be measurable when the resolving power of the experimentally used spectrometer is considered.

The emitting particles within the plasma are moving with a thermal velocity. Hence, similarly to the Thomson scattering signal, the recorded frequency of the emitted radiation is shifted by the velocity component in the observer's viewing direction, according to

$$\frac{\omega - \omega_0}{\omega_0} = \frac{v_{q,th}}{c_0}\,, \tag{2.61}$$

where $v_{q,th}$ denotes the velocity component in the viewing direction and $\omega_0$ is again the central frequency of the line. This effect is referred to as Doppler broadening. The shape of a Doppler broadened line follows the velocity distribution of particles. Assuming a Maxwellian distrubution, the line profile has a Gaussian shape given by:

$$I(\omega) = I(\omega_0)\mathrm{e}^{-\left(\frac{\omega - \omega_0}{\Delta\omega_G}\right)^2} \quad \text{with} \quad \Delta\omega_G = \frac{\omega_0}{c_0}\sqrt{\frac{8k_B T_q \ln 2}{m_q}}\,. \tag{2.62}$$

Herein $\Delta\omega_G$ is the profile's FWHM with $T_q$ being the temperature and $m_q$ the mass of the emitter. The impact of Doppler broadening on the recorded line width is by far more significant than natural

broadening. As stated by Thorne [171], the widths of the Doppler broadened lines range between $0.04 - 0.00004$ nm for atoms and diatomic plasmas. The expected Doppler broadened line width $\Delta\omega_G$ can be estimated for a certain wavelength with the equation (2.62). In case of nitrogen, both molecular and atomic lines can be observed in the expected temperature range [99], though molecular lines or rather bands (as discussed in sect. 2.2.4) are expected to be more pronounced as the density of nitrogen molecules is several orders of magnitude higher than the density of atomic nitrogen for non-equilibrium plasmas [179].

However, to estimate the influence of Doppler broadening, a hydrogen line with a wavelength of 486.13 nm is chosen. This hydrogen line, referred to as $H_\beta$, is of particular interest for electron density determination which is discussed in depth in section 2.2.3. The broadening can be approximated with a simplified formula given by Xiao *et al.* [183]

$$\Delta\lambda_{Dopp} \cong 3.48 \times 10^{-4} \sqrt{T_h}. \tag{2.63}$$

As presented in Fig. 2.10, the calculated width increases slightly in the expected temperature range. Nonetheless, when convoluted with the apparatus profile of the spectrometer, the influence of the broadening effect is almost non existent as also shown in Fig. 2.10. Thus, for an instrumental profile width in the range of 0.1 nm the Doppler broadening can be neglected for line shape evaluation.

Besides the natural and Doppler broadening, several further broadening mechanisms of spectral lines exists. Frequent interactions with external agents, which are too weak to produce the excitation responsible for the emission itself but still strong enough to modify the lifetime of the excited electron, are responsible for further broadening of the line shape. The broadening is hence directly proportional to the corresponding interaction frequency, with a high collision/interaction rate leading to a less narrow spectral line. Depending on the interaction mechanism an additional slight shift of the central frequency can also occur, this however will not be considered here. These external agents can be neutral particles, then the effect is referred to as pressure broadening, or charged particles, referred to as Stark broadening or Stark effect.

The pressure broadening by neutral particles can be further divided with respect to the interacting agents. If the agents are of the same kind (e.g. two identical atoms), then their interaction results in resonance broadening where either the upper energy state from which the transition starts or the lower energy state to which the electron returns is in both cases the upper energy state of a resonant transition [102]. In that case the emitted line has a Lorentzian shape. If the interacting agents are of unlike kind, but are still neutral particles, then the line shape is also Lorentzian but the width is defined by van der Waals forces. Hence, this effect is usually referred to as van der Waals broadening. Laux *et al.* [103] presented a formula which allows the estimation of van der Waals broadening of the hydrogen line at 486.13 nm. As discussed by the authors, the formula can be simplified to

$$\Delta\lambda_{vdW} \cong 3.6 \times \frac{p}{T_h^{0.7}} \tag{2.64}$$

with $p$ being the atmospheric pressure. Thereafter, for a temperature of 5000 K the $\Delta\lambda_{vdW}$ of the hydrogen line lies in the range of picometers and is about 2.7 times smaller than the Doppler broadening as can be seen in Fig. 2.10. Considering the spectral resolution of the experimental setup, the van der Waals broadening thus appears to be insignificant. Moreover, according to Kunze [102], although the pressure broadening by neutral particles comes into play in weakly ionized low temperature plasmas, even then it can be neglected when compared to the broadening caused by charged particles. Thereafter, the influence of pressure broadening effects caused by neutral particles is neglected within this work.

Pressure broadening caused by charged particles, also referred to as Stark broadening, is however more complex and usually dominates in plasmas. This broadening mechanism can be furthermore utilized to determine the electron density as mentioned above. Hence, it cannot be neglected and is discussed in detail in the following section.
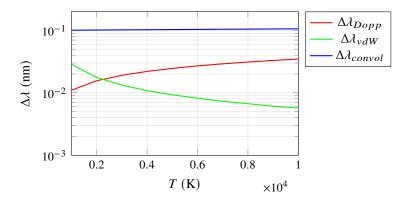
Figure 2.10: Dependence of Doppler $\left(\Delta\lambda_{Dopp}\right)$ and van der Waals $(\Delta\lambda_{vdW})$ broadening mechanisms on $T_h$ for the $H_\beta$ line at $\lambda = 486.13$ nm, calculated with eq. (2.63) and (2.64) respectively, as well as the influence on the line width after convolution with the instrumental profile $(\Delta\lambda_{convol})$ assuming a $\Delta\lambda_{app} = 0.1$ nm.

## 2.2.2 Spectral line broadening in a plasma due to the Stark effect

The so-called Stark broadening arises in an ionized gas, i.e. plasma, due to the interaction of the atom's bound electrons with the electric field created by free electrons within the plasma surrounding the atom.

In general the interaction between the atom's bound electrons and any external agents is of electromagnetic nature, with the coupling of any charge $q$ to the electric field being much stronger than to the magnetic field (assuming $v_q \ll c_0$, with $c_0$ being the speed of light). Since each atom is electrically neutral, at least when observed at length scales coarse enough, in order to be able to interact with either the plasma or the (incident or emitted) radiation an atom must develop a electric dipole moment arising from a slight local separation $d$ of positive and negative charges within the atom. The electric dipole moment of an atom can be described as

$$\vec{d}_{dip} = \vec{d} \, q_e \, . \tag{2.65}$$

This dipole moment couples to the electric field $\vec{E}_0$, the latter either created by the plasma's free electrons or that corresponding to the radiation's electromagnetic wave. The resulting interaction energy scale is given by

$$E_{int} = \vec{d}_{dip} \cdot \vec{E}_0 \, . \tag{2.66}$$

Actually, the above equation describes two effects. Either the main interaction with the bound electron, which causes its excitation and eventually leads to the emission of the observed line's wavelength, or a weaker disturbance, which, although not able to drive the bound electron to an excited state, is still able to broaden the emitted spectral line from the previous main interaction. The Stark effect corresponds to the second category and is due to the interaction of the atom's bound electrons with the plasma's free electrons. This effect mainly occurs as one of the two following opposite approximations:

1. Quasistatic approximation: The electron distribution within the atom is not spherically symmetric (like in the hydrogen atom) and the atom already displays a permanent electric dipole. In this case the plasma's electric free charges can be assumed to act collectively, at once, as a "cloud", creating the external electric field $\vec{E}_0$ which interacts with the atom's dipole moment. This is also called linear Stark effect, to be discussed later in more detail in section 2.2.3.

2. Impact approximation: The electron distribution within the atom is spherically symmetric (like in a noble gas atom) and there is no permanent electric dipole. In this case the interaction is mediated by two electrons: the first one, which after approaching the atom polarizes the latter for a very short time interval, and the second one, which during such time interval interacts

with the induced, short-lived, electric dipole moment. This effect is referred to as quadratic Stark effect. Since a consecutive collision with two electrons is seldom enough, the quadratic Stark effect is much weaker than the linear one. Moreover, due to the low probability of this combined double collision, a subsequent double collision can be considered to be statistically independent of the previous one, leading thus to the impact approximation, where the total effect is just the uncorrelated sum (or average) of single double interactions [158]. Such sum is carried out by introducing the probability for collision/interaction with free electrons in the plasma during a time interval $\Delta\tau$. This collision probability is proportional to the electron density $n_e$, their velocity $v_e$ and to the collision cross-section $\sigma_{col}(v_e)$:

$$\text{collision probability at } v_e: \quad n_e\, v_e\, \Delta\tau\, \sigma_{col}(v_e)\,.$$

The cross-section $\sigma_{col}$, in general a complex nonlinear function of the free electron velocity $v_e$, effectively represents the area offered by the interacting particles to each other. The just mentioned average involves an integration over different electron velocities, which leads to a small temperature dependence if the distribution of electron velocities is in thermodynamical equilibrium. Instead of a detailed average, which also involves an additional average over different scattering angles [56], a simple qualitative estimation can be nevertheless obtained for the spectral line broadening within the framework of the impact approximation.

According to Heisenberg's time-energy uncertainty relation, the lifetime $\Delta t$ of some excited state and the corresponding energy scale $\Delta E$ responsible for limiting such lifetime are related to each other as

$$\Delta t\, \Delta E \sim \hbar\,. \tag{2.67}$$

The lifetime $\Delta t$ is defined as the average time between consecutive collisions, i.e. the time interval $\Delta\tau$ required for having a collision probability equal to 1. Hence it can be written

$$n_e\, v_e\, \Delta t\, \sigma_{col} \sim 1 \quad \text{or equivalently} \quad \frac{1}{\Delta t} \sim n_e\, v_e\, \sigma_{col}\,.$$

The frequency uncertainty $\Delta\omega_{broad}$ characterizing the broadening of the transition frequency at $\omega_{if}$ is directly related to the energy uncertainty $\Delta E = \hbar\Delta\omega_{broad}$. Hence

$$\Delta\omega_{broad} \sim \frac{\Delta E}{\hbar} \sim \frac{1}{\Delta t} \sim n_e\, v_e\, \sigma_{col}\,, \tag{2.68}$$

where the form of cross-section $\sigma_{col}$ is completely determined by the interaction form which is assessed by the energy scale $\Delta E$.

In the remaining part of this section only the quasistatic approximation (or linear Stark effect) will be considered, applied this time to the most simple atom.

### 2.2.3 Particular case: broadening of the hydrogen $\alpha$ and $\beta$ spectral lines

In case of a hydrogen atom the single emitting electron together with the positively charged nucleus already forms an electric dipole and thus the perturbation to the bound electron's energy corresponds to the linear Stark effect. As already mentioned in the previous discussion the resulting spectral line broadening is therefore stronger than in the case of a noble gas atom. Radial distances where the bound electron is mainly located inside the hydrogen atom are quantized and can be derived semi-classically. Since hydrogen only contains one single bound electron attached to its nucleus the total energy (kinetic plus potential) of that bound electron is equal to

$$E = \frac{p^2}{2m_e} - \frac{q_e^2}{4\pi\varepsilon_0}\frac{1}{r} \tag{2.69}$$

with $r$ denoting the distance between electron and nucleus and $p$ the electron's momentum. According to the Bohr's postulate the angular momentum is quantized, that is only "quantum leaps" of $\tilde{n}\hbar$ are possible with $\tilde{n}$ being an integer number called the principal quantum number. Hereafter, for the angular momentum can be written

$$r\, p = \tilde{n}\, \hbar \,.$$

Combining the above equation with the equation (2.69) for the energy of the bound electron yields

$$E(r) = \frac{\tilde{n}^2 \hbar^2}{2 m_e r^2} - \frac{q_e^2}{4\pi\varepsilon_0} \frac{1}{r} \,. \tag{2.70}$$

As can be seen, the energy function depends only on one variable - the distance $r$. The energy minimization principle then allows to define the quantized radial distances as

$$\left. \frac{dE}{dr} \right|_{r=r_n} = 0 \;\; \Rightarrow \;\; r_{\tilde{n}} = \tilde{n}^2 \frac{\hbar^2}{m_e} \left( \frac{4\pi\varepsilon_0}{q_e^2} \right) \,. \tag{2.71}$$

According to the above, the strength of the electric dipole when the bound electron transits from the energy level of quantum number $i$ down to the level of number $f$ is equal to

$$d_{dip,if} = q_e \left( r_i - r_f \right) = q_e \frac{\hbar^2}{m_e} \left( \frac{4\pi\varepsilon_0}{q_e^2} \right) \left( i^2 - f^2 \right) \,. \tag{2.72}$$

The scale of the energy uncertainty $\Delta E$ responsible for the frequency broadening $\Delta\omega_{broad}$, defined by equation (2.68), corresponds to the interaction energy $E_{int} = \vec{d}_{dip} \cdot \vec{E}_0$. The electric field $\vec{E}_0$ interacting with the atom's electric dipole is created by the free charges, ions and/or electrons, inside the plasma. Its strength can be estimated from the electric field strength created by a free point charge $q$,

$$|\vec{E}| \sim \frac{q}{4\pi\varepsilon_0} \frac{1}{r^2} \,,$$

where $r$ is the average separation distance between the plasma charges. If a sphere containing in average 1 electron is created within that distance, $r$ can be approximated with

$$\frac{4\pi}{3} r^3 n_e = 1 \quad \Longrightarrow \quad r = \left( \frac{4\pi}{3} \right)^{-1/3} n_e^{-1/3} \,.$$

Hence, the interacting electric field $\vec{E}_0$ can be estimated with

$$\left| \vec{E}_0 \right| \sim \frac{q_e}{4\pi\varepsilon_0} \left( \frac{4\pi}{3} \right)^{2/3} n_e^{2/3} \,. \tag{2.73}$$

This estimation does not consider correlations between free charges which modify the strength of the electric field affecting the bound electron. Taking such effects into account requires complicated numerical simulations and will not be considered here. Finally, the full width at half maximum of the line profile broadened by charged particles, expressed both in frequency and in wavelength, is approximately equal to

$$2\Delta\omega_{broad} \sim 2 \frac{d_{dip} \left| \vec{E}_0 \right|}{\hbar} \sim 2 \left( \frac{4\pi}{3} \right)^{2/3} \frac{\hbar}{m_e} \left( i^2 - f^2 \right) n_e^{2/3} \,, \tag{2.74}$$

$$2\Delta\lambda_{broad} \sim \frac{\lambda_{if}^2}{2\pi c} 2\Delta\omega_{broad} \sim 2 \left( \frac{4\pi}{3} \right)^{2/3} \frac{\lambda_{if}^2 \, \hbar c}{2\pi m_e c^2} \left( i^2 - f^2 \right) n_e^{2/3} \,.$$

Typical applications of these relations are hydrogen's alpha line $H_\alpha$ ($\lambda_{if}$ = 656.28 nm) for the transition $i = 3 \rightarrow f = 2$ and hydrogen's beta line $H_\beta$ ($\lambda_{if}$ = 486.13 nm) for the transition $i = 4 \rightarrow f = 2$, which are used for electron density estimation. It is worth noting that the spectral broadening of the hydrogen lines is not only more pronounced that in a noble gas, as the latter requires the combined consecutive interaction with two electrons and is since less probable, but also shows no dependence on the temperature since no thermal velocity of the plasma's charged particles is involved, at least not in the order of approximation considered here. Only when including the correlation between free electrons and ions within the plasma such dependence occurs [53], although it is weak. The weak temperature dependence can actually be nearly completely removed if, instead of the full width at half maximum, the full width at half area (area contained inside the broadened spectral line) of the hydrogen line is considered [53].

Concluding, the obtained relation (2.74) differs for the full width at half area (FWHA) only by a factor in the order of magnitude of 1 from the more exact result [53]. Therefore, within this work the FWHA of the hydrogen lines is used to estimate the electron density according to following correlations

$$
\begin{aligned}
H_\alpha : \quad &\text{FWHA [nm]} = 0.549 \left( \frac{n_e \ [\text{m}^{-3}]}{10^{23}} \right)^{0.67965}, \\[2mm]
H_\beta : \quad &\text{FWHA [nm]} = 1.666 \left( \frac{n_e \ [\text{m}^{-3}]}{10^{23}} \right)^{0.68777}.
\end{aligned}
\tag{2.75}
$$

It is worth mentioning that the dependence on the plasma's electron density is weaker in the case of hydrogen (linear Stark effect $\sim n_e^{2/3}$, see eq. (2.74)) than in the case of a noble gas (quadratic Stark effect $\sim n_e$, see eq. (2.68)).

### 2.2.4 Basics of molecular spectroscopy

As presented in section 2.2.1, atoms emit individual lines due to excitation of bound electrons, which makes the radiation characteristic for a specific change of the electronic energy state. The atoms also move in all directions hence the total energy of an atom is a function of the kinetic energy of its center of mass. In case of a molecule, apart from the internal electronic energy and kinetic energy due to the movement of the whole molecule (i.e. its center of mass) in three directions, the relative, vibrational motion of the atoms along the internuclear axis and the relative, rotational motion about two axes perpendicular to the internuclear axis contribute to molecule's energy. Since both the vibrational and rotational energy states are quantized, each transition described by the quantum number $v$ and $J$ respectively emits radiation at a specific frequency, resulting in a much more complex spectrum.

A diatomic molecule in a plasma vibrates about the equilibrium bond length, i.e. a distance at which the attractive and repulsive forces due to the electric field of nuclei and valence electrons are balanced, and simultaneously rotates about an perpendicular axis with rotational inertia depending on the bond length. Therefore each electronic state contains a range of vibrational levels and each vibrational level contains a structure of rotational energy levels. According to [25] the energy coupling through vibrational and rotational states is rather poor. In a typical electron excitation of a rotational state an energy in order of 0.001 eV is transferred. In case of a typical electron excitation of vibrational states, energies in order of 0.1 eV are transferred. Since the energy structure depends on the internuclear distance, the energy levels are defined by potential curves presented in Fig. 2.11 for a nitrogen molecule. The emitted radiation forms spectral bands that reflect the rotational and vibrational states as exemplarily shown in Fig. 2.12. The spectrum depicted in Fig. 2.12 was measured experimentally at a distance of 2 mm from nozzle outlet for the investigated plasma, which was operated at a frequency of 60 kHz. Based on the measured spectra, the parameters characterizing the energy distribution in a plasma can be thus estimated. The following discussion considers only diatomic molecules ($N_2$) and is
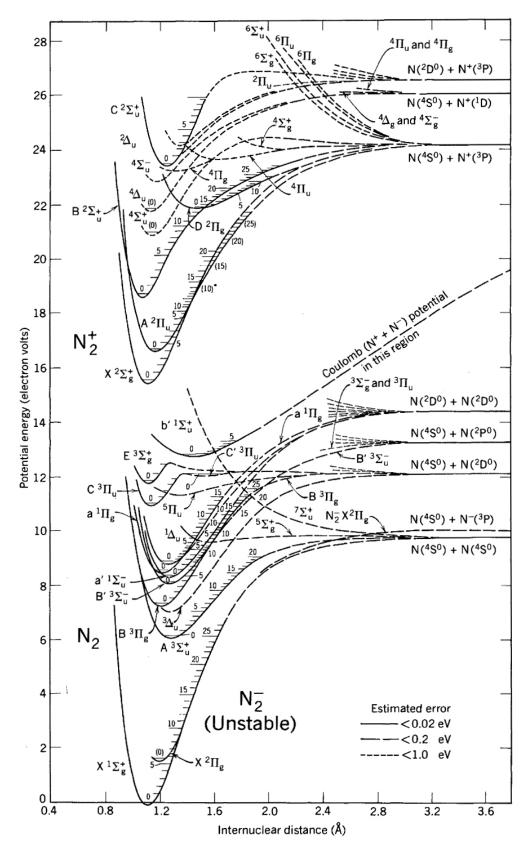
Figure 2.11: Potential curves for different energy levels of $N_2$ and $N_2^+$ after [162].

mainly based on works by Demtröder [35], Struve [162], Herzberg [63, 69], Ochkin [137] as well as Lofthus and Krupenie [110]. For more details it should be referred to the above publications.
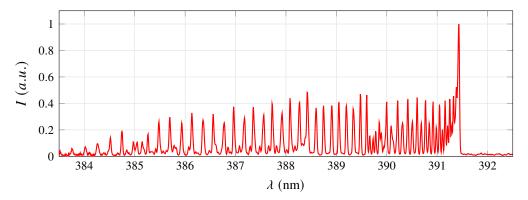


Figure 2.12: Rotational structure of a band sequence of the $(0, 0)$-transition of the $B^2\Sigma_u^+ \rightarrow X^2\Sigma_g^+$ system of $N_2^+$ measured experimentally for the discharge operated at 60 kHz.

According to the Born-Oppenheimer approximation, the total energy of a nitrogen molecule $E(v, J)$ is a sum of the electronic energy $E_e$, vibrational energy $E_{vib}$ and rotational energy $E_{rot}$. Thus, it can be written

$$E(v, J) = E_e + E_{vib}(v) + E_{rot}(v, J) \ . \tag{2.76}$$

The electronic energy $E_e$ is the energy separation between the minima in the potential curves of two electronic states (see Fig. 2.11). To describe the vibrational energy $E_{vib}(v)$ it is assumed that a diatomic molecule behaves like a harmonic oscillator. By doing so, it can be written

$$E_{vib}(v) = \omega_e \left(v + \frac{1}{2}\right) \ .$$

Herein, $\omega_e$ is defined as the equilibrium oscillation frequency, i.e. a frequency for infinitely small vibrations around the equilibrium bond length of a molecule, and is often referred to simply as vibrational constant. As can be seen from the above, the vibrational energy levels are a function of $v$ and are evenly spaced in case of a harmonic oscillator with the lowest energy level being $E(v = 0) = 0.5\,\omega_e$. For larger vibration amplitudes, i.e. higher vibrational quantum numbers $v$, the observed oscillation frequencies deviate however significantly from the frequencies determined for the harmonic oscillator. As the potential curve for each transition converges towards the dissociation energy $E_{diss}$ with increasing internuclear distance (see Fig. 2.11), the behaviour of a molecule is better approximated by an anharmonic oscillator. In that case, the equation defining the vibrational energy is extended with an anharmonic term, which reduces the frequency steps with increasing quantum number $v$. Hence, the energy is given by

$$E_{vib}(v) = \omega_e \left(v + \frac{1}{2}\right) - \omega_e x_e \left(v + \frac{1}{2}\right)^2 \tag{2.77}$$

with $x_e$ being the anharmonicity constant. For a given molecule, both $\omega_e$ and $x_e$, usually given as $\omega_e x_e$, depend on the particular electronic level and are tabulated. The exact values for each energy level can be found in [69, 110].

The rotational energy can be calculated for a single vibrational state $v_0$ with equation (2.21), assuming the nitrogen molecule behaves like a rigid rotator. Nevertheless, the rigid rotator assumption gives rather imprecise results for spectroscopic applications. Thus, the equation is extended by a factor that takes into account the variation of the bond length,

$$E_{rot}(v_0, J) = BJ(J + 1) - DJ^2(J + 1)^2 \tag{2.78}$$

with the rotational constant $B$ given by equation (2.22) and the centrifugal constant $D$ according to [162] given by

$$D \cong \frac{4B^3}{\omega_e^2} . \tag{2.79}$$

The energies calculated for each vibrational state $v_0$ cannot simply be added up to obtain the total rotational energy for all states $v$, because the rotational levels are not independent of the vibrational levels as the bond length changes permanently due to both oscillations and the centrifugal force. To be able to add the energies according to equation (2.76), the rotational and centrifugal constants need to be redefined as functions of $v$, yielding

$$B_v = B - \alpha_e \left( v + \frac{1}{2} \right) , \quad D_v = D + \beta_e \left( v + \frac{1}{2} \right) . \tag{2.80}$$

The coefficients $B, \alpha_e, D, \beta_e$ are tabulated for each particular electronic level of a molecule and can be found in [69, 110]. As $E_e$ is also tabulated, the total energy of a nitrogen molecule is given by

$$E(v, J) = E_e + \omega_e \left( v + \frac{1}{2} \right) - \omega_e x_e \left( v + \frac{1}{2} \right)^2 + B_v J (J+1) - D_v J^2 (J+1)^2 . \tag{2.81}$$

### 2.2.5 PARAMETER EVALUATION BY SYNTHETIC SPECTRA FITTING

As a consequence of the energy difference between two energy levels of bound electrons, radiation is emitted at a certain frequency according to equation (2.57). In case of molecules much more energy differences are possible due to the contributions of each rotational, vibrational and electronic transition. The intensity emitted by a certain transition depends similarly to atomic radiation on the particle density of the emitting energy level and on the probability of the transition $i \to f$. Nonetheless, for molecules a number of selection rules exist which, based on symmetry considerations, select only certain combinations of energy levels between which radiation transitions most probably take place.

Thereafter, the rotational lines follow the selection rules $\Delta J = 0 \pm 1$, forming the s.c. $P$-, $Q$- and $R$- line branches. Depending on the electron configuration in the orbitals of a molecule, which are denoted with capital greek letters, a $\Sigma \to \Sigma$ transition contains only $P$- ($\Delta J = -1$) and $R$- ($\Delta J = 1$) lines, whereas $\Sigma \to \Pi$ or $\Pi \to \Pi$ transitions contain also $Q$- ($\Delta J = 0$) lines. To describe how the total intensity is distributed among the $P$-, $Q$- and $R$-branches the Hönl-London factor $S_{J,if}$ is defined and can be calculated for each transition with corresponding equations summarized and corrected by Ochkin in [137]. Vibrational lines on the other hand are selected according to the Franck-Condon principle. Here it is assumed that, due to the low electron mass, the transition between two electronic states occurs so fast (about $10^{-15}$ s) that both position and velocity of the nuclei hardly change during the electron jump. Therefore the kinetic energy of the nuclei remains constant during the transition. If an electron now transitions from one electronic state to another, the more the vibrational wave functions of the two states are compatible with each other (i.e. as similar as possible to the original nuclear coordinate), the more likely this transition is. Since the internuclear distance does not change, the vibrational transitions occur along straight vertical lines in the potential curve diagram shown in Fig. 2.11. The transition probability is expressed by the Franck-Condon coefficients, which are tabulated for each transition [110].

According to the above discussion, for the experimentally registered intensity can be written

$$I(\omega_{if}) = K \, S_F \left( \omega - \omega_{if} \right) n_{N_2} \left( \frac{\omega_{if}}{2\pi c_0} \right)^4 S_{J,if} \, \mathrm{e}^{\frac{-\left( E_{rot,i} - E_{rot,f} \right)}{k_B T_{rot}}} S_{v,if} \, \mathrm{e}^{\frac{-\left( E_{vib,i} - E_{vib,f} \right)}{k_B T_{vib}}} \, \mathrm{e}^{\frac{-\left( E_{e,i} - E_{e,f} \right)}{k_B T_e}}$$

$$\tag{2.82}$$

with $S_{J,if}$ being the Hönl-London factor, $S_{v,if}$ the tabulated Franck-Condon coefficient for the specific transition, $n_{N_2}$ the density of the emitting molecules and $T_{rot}$ and $T_{vib}$ being the rotational and

2

vibrational temperatures. The transfer function of the experimental setup, denoted with $S_F$ above, can be determined before measurement with a spectral calibration lamp, whereas the detection sensitivity $K$ is also determined beforehand with a calibrated tungsten ribbon lamp.

Thereafter, the characteristic plasma parameters can be evaluated with equation (2.82) from the experimentally measured spectrum by iterative fitting of a calculated intensity to the recorded values. The emitting transitions are determined based on frequencies present in the recorded spectrum, while the corresponding energies can be calculated based on tabulated values as presented in previous section. The iterative variables that are adjusted during the fitting process are the temperatures $T_{rot}$, $T_{vib}$ and $T_e$ and the temperature dependent number density of emitting particles $n_{N_2}$. For the computation of particle densities usually Maxwell-Boltzmann distributions are assumed. The difficulty mainly arises from the temperature dependence of the ionization and dissociation reactions which are still topic of current research debates, especially for non-equilibrium plasmas [27, 119, 179]. As stated by Wang *et al.* [179] it is commonly accepted that the transitions between excited levels are mainly caused by inelastic electron collisions if the electron number density is high and hence the reactions are governed by $T_e$. If the electron density is low however, inelastic atomic and molecular collisions are responsible for electron transitions and therefore the temperature of heavy particles $T_h$ is used for calculations. As stated by the authors, the ionization of nitrogen molecules occurs mainly under such conditions [179]. Thereafter, if the rotational and vibrational energy levels are assumed to be populated by heavy particle collisions, the computations can be simplified by assuming that $T_{rot} = T_{vib} = T_h$ [46]. An exemplary estimation of the gas composition assuming a two temperature model ($T_e$, $T_h$) is given in Appendix C. Additionally, a detailed calculation procedure of the emission spectrum for the $C^3\Pi_u \rightarrow B^3\Pi_g$ transition of molecular nitrogen based on tabulated values is shown in Appendix D.

As can be deduced from the above, the fitting procedure of a molecular spectrum is quite complex and cannot be preformed manually. Each transition is characterized by a different set of tabulated data and follows different selection rules, as described above, which have to be implemented into the fitting procedure. Since several transitions overlap in certain wavelength ranges in a measured spectrum, the fitting procedure in those ranges can be time-consuming if not implemented optimally. Furthermore, the fit accuracy also depends on the used data set which vary slightly from author to author. For these reasons, it seems inefficient to develop a fitting procedure by oneself, especially since an established solution is available. Thereafter, a commercially available software Specair 3.0 made by SpectralFit S.A.S., Antony, France is used for the parameter evaluation from the measured nitrogen molecular spectra. The software is based on quantum mechanical calculations providing higher accuracy and has integrated fitting algorithms [160]. This software is well established in the scientific world and used by many researchers [23, 76, 103, 114, 139].

### 2.2.6 PARAMETER EVALUATION WITHOUT SYNTHETIC SPECTRA FITTING

Several different techniques exist to estimate the rotational or vibrational temperature, which do not require fitting of synthetic spectra [23, 52, 155]. As suggested by Scott *et al.*, the rotational temperature can be estimated by integration of several rotational peaks of the FNS $(0, 1)$-transition of the ionized nitrogen molecule [155]. The integrals are then related to an integral of the main band head peak at 427.81 nm and the temperature is obtained from a fit of the integral ratios. The vibrational temperature can be estimated similarly, with the difference that the band head peaks of different vibrational transitions are integrated and set in relation to each other. A simpler method, also based on the first negative system of ionized nitrogen molecule, is suggested by Chen and Li [23]. The authors compare in a Boltzmann plot the amplitudes of seven rotational peaks in a wavelength range between 389.9 nm and 391.1 nm of the FNS $(0, 0)$-transition with the quantum numbers of the upper (denoted with $J$) and lower (denoted with $J'$) electronic state. The exact wavelengths of the peaks are marked in Fig. 2.13. If the amplitudes are plotted in a certain coordinate system (see Fig. 5.6), the rotational

temperature is then obtained from the slope of a linear fit according to the following equation, given in [23],

$$\ln\left(\frac{I\,\lambda^4}{(J+J'+1)}\right) = -\frac{2.983}{T_{rot}}J\,(J+1) + C \tag{2.83}$$

with $I$ being the line intensity, $\lambda$ the wavelength of the according line and $C$ a constant.

Apart from the estimation of rotational temperature, this method can be also used to identify a possible deviation of the rotational levels from a Boltzmann distribution. Furthermore, it can be applied without the knowledge of the instrumental profile of the apparatus used, although the spectral resolution of the setup has to be high enough to resolve the rotational structure and a spectral overlap with other transitions is to be avoided. Even though the application of this method appears simple at first glance, it can be cumbersome, especially when multiple measurements are to be evaluated. Therefore, it is used here only as an additional validation to verify whether the rotational levels follow a Boltzmann distribution. For a detailed description it should be referred to [23].
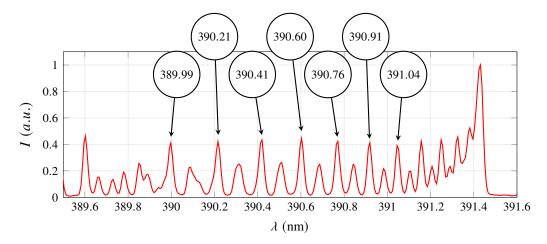


Figure 2.13: The rotational temperature can be estimated based on the marked transitions of the $B^2\Sigma_u^+ \rightarrow X^2\Sigma_g^+$ system of $N_2^+$ according to the method proposed by Chen and Li [23]. Furthermore, a possible deviation of the rotational levels from a Boltzmann distribution can be identified with this method.

### 2.2.7 RELATION BETWEEN ROTATIONAL AND GAS TEMPERATURE

As pointed out by Cruden *et al.* [33], the rotational temperature can be assumed to be equal to the gas or, more precisely, the translational temperature of neutral species if several equilibration conditions are fulfilled. Firstly, it is assumed that the emitting rotational level is in thermal equilibrium and thus obeys a Boltzmann distribution, which can be assessed using the method discussed in the previous section. Then it is assumed that the translational temperature is high enough to equilibrate with the rotational temperature. Thirdly, that the rotational temperature of the upper energy state responsible for radiative emission is in equilibrium with the ground state. Finally, an equilibrium is assumed for rotational temperatures of different excited species. This condition can be verified by a simple comparison of the estimated temperatures for different transitions (see sect. 4.3.2). As stated in [12, 103], the above conditions are typically fulfilled at atmospheric pressure because of the fast rotational relaxation. The relaxation time $\tau$ depends inversely on the density of the species $n$, the collision cross section $\sigma$ and the thermal velocity of the species $v_{h,th}$ as follows $\tau = 1/(n\sigma v_{h,th})$ [107]. If a temperature of 6000 K is assumed, then a relaxation time of around 0.5 ns is expected at atmospheric pressure for the above transitions. When compared to radiative lifetimes of energy levels given by Gilmore *et al.* [54], being about 40 ns for the upper SPS state and 90 ns for the FNS, it becomes apparent that the rotational levels of these states will equilibrate with the translational energy before radiation occurs due to much

more frequent particle collisions. Thereafter, the heavy particles temperature estimated with the laser scattering diagnostic setup as well as the rotational temperatures estimated based on molecular spectra are considered to be equal to the translational, i.e. gas temperature.

**2**

# 3

<div align="center">

## EXPERIMENTAL SETUP

</div>

## 3.1 DESCRIPTION OF THE PLASMA SYSTEM

The aim of this work is to characterize a pulsed, low-current direct discharge operated at atmospheric pressure. There are several commercially available systems on the market utilizing a more or less similar working principle [41, 85, 95, 181]. Here the rather compact system, consisting of a PG31 plasma generator and a PS2000 OEM power supply, both produced by Relyon Plasma GmbH, Regensburg, Germany, was chosen. This generator can be used for surface activation, decontamination or deposition of different materials [90, 94, 95, 165, 178].

### 3.1.1 COMPONENTS

The PG31 generator has a conventional construction with a positively biased, finger-shaped non-refractory inner electrode and a copper alloy nozzle acting as cathode, as presented in Fig. 3.1. Several nozzle geometries are available from the manufacturer - a conical shaped one of type A450 with an exit diameter of 4 mm is used exclusively for the investigations. To prevent a premature electrode wear as well as for cooling purposes, a vortex flow of the plasma carrier gas inside the nozzle is introduced. The system does not require any additional cooling. Various working gases can be used, although the



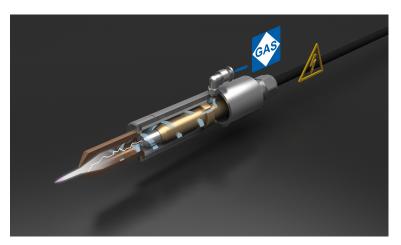Figure 3.1: A schematic cross section of the used plasma generator. Image courtesy of Relyon Plasma GmbH, Regensburg, Germany.

generator is optimized for operation with molecular gases as is usually the case for low-current direct discharges in this power range. Hence most commonly compressed air, pure nitrogen or $N_2$-based mixtures with hydrogen or carbon dioxide are used [95, 130, 181]. The generator can be operated

with gas flow rates between 35-60 standard liters per minute (short l/min) [94], which is regulated separately by an external controller. Accordingly, pure nitrogen at a flow rate of 35 l/min is used in all the following experiments, regulated by a mass flow controller of type 8626 produced by Bürkert GmbH & Co. KG, Ingelfingen, Germany.

Unipolar, triangular current pulses with an variable amplitude of maximal 1 A are generated at the output of the PS2000. As schematically shown in Fig. 3.2, the power supply utilizes a single-phase full-bridge push-pull converter design with a power factor correction module coupled to a transformer that, in total, generates bipolar triangular-shaped current pulses. These are rectified by a full-wave diode bridge with a discrete capacitor at the exit. In steady-state operation, the rise and fall times are fixed at 5 µs regardless of the selected pulse frequency, giving a theoretical maximum charge of 6.5 µC per pulse. The power supply can be controlled via a PC software, which allows an adjustment of the output power between 70-100 %, what corresponds to a current amplitude of 0.7-1.0 A at the exit, whereas the pulse frequency can be varied between 40 kHz and 65 kHz in 1 kHz steps. The maximal pulse frequency is limited by the switching speed of the built-in semiconductors [95]. The generator is connected to the power supply by a 9 m long triaxial cable (similar to a coaxial cable, but with an additional conductive sheath), which serves as an additional high voltage capacitor by utilizing the properties of such a cable. The total cable length between PG31 and PS2000 is 10 m.
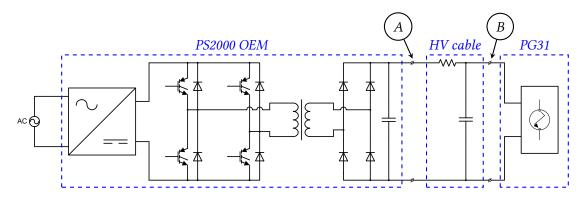


Figure 3.2: Simplified electrical diagram of the plasma system with its components. Relevant connection points between them are marked with capital letters.

### 3.1.2 Ignition and working principle

To ignite the discharge, a gap of 8 mm between the electrodes has to be bridged initially. To achieve this the source charges the capacitors, i.e. the capacitor inside of the PS2000 and the connection cable, up to a voltage between 13 kV and 15 kV. After ignition, the current amplitude of the triangular pulses is gradually increased reaching the target value after ca. 15 ms. In that time, since low-current ($i < 30$ A) discharges are reported to be driven by buoyancy of the gas flow [128], the discharge channel rotates and elongates downstream inside the generator chamber implying a rise of the operating voltage. In case of the A450 nozzle, the discharge channel reaches a length of over 50 mm. According to Raizer [148], a discharge between two non-refractory electrodes cannot be sustained if the current is interrupted for more than 1 ms. For a much higher frequency, however, the discharge channel can be reignited with each pulse retaining thereby roughly its length, rather than being re-strucked at the shortest gap between the electrodes, since many of the free electrons have not been yet recaptured, i.e. recombined, by the plasma ions. Thus, at frequencies in the range of tens of kHz at which the system operates, each pulse reignites the pre-ionized channel and the peak breakdown voltage during steady-state operation stabilizes between 3.0-4.0 kV for nitrogen at 35 l/min. A detailed analysis of voltage and current traces is presented in section 4.1. Steady-state operation is reached after approx. 20 ms in the case of the A450 nozzle, where the discharge channel is blown out of the nozzle, reverses

and forms a cathodic attachment point at the nozzle lip as can be seen in Fig. 3.3. The swirl of the gas flow drags the attachment point around the lip, preventing thereby premature wear of the nozzle. As suggested by Korzec and Nettesheim [95], the effluent plasma jet can be hence divided into two main zones. The first one being the zone, where the discharge is blown out of the nozzle and mixes with ambient atmosphere inducing additional chemical reactions. In the second zone the excited and ionized species recombine to their ground states emitting the excess energy as radiation. Surface treatment is usually performed within this region [41, 90, 94, 181].
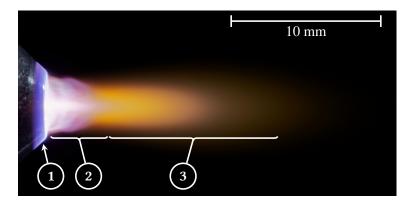


Figure 3.3: The effluent plasma jet can be divided into following zones, as suggested in [95]: 1 - cathodic attachment, 2 - blown-out discharge zone, 3 - recombination zone.

The power source operates without a complicated control loop, it simply charges the capacitors with a defined current pulse at a defined repetition rate. Thus, the discharge timing is not controlled - it happens when the breakdown voltage across electrodes is reached - and there is no feedback signal from the generator if a breakdown occurred. Furthermore, although the system is optimized for "one pulse per discharge"-operation, in extreme cases several consecutive pulses may be required to reach the breakdown voltage, which depends mainly on the plasma gas composition as well as on the pressure inside the generator, i.e. the gas flow rate. This rather simple design of the system ensures high robustness and a wide range of applications, but at the same time implies that certain fluctuations in the plasma properties are inevitable, since the next discharge depends on the energy state of the channel left by the previous pulse. So there is a certain memory effect, which leads to the fact that only a comprehensive statistical analysis is applicable to study the behavior of this system.

## 3.2 Voltage and current acquisition

Electric voltage and current are those physical quantities that can be measured most easily. For this purpose, a dedicated measurement box was set up in which the triaxial cable was separated so that both signals can be recorded using standard probes. The voltage and current traces were measured in both connection points of the system, i.e. at the exit of the power supply (marked as A in Fig. 3.2) and prior to the plasma generator (marked as B in Fig 3.2) for different pulse frequencies and power settings. The acquisition is based on a digital oscilloscope of type HDO8108A produced by Teledyne Lecroy, Chestnut Ridge, NY, USA. The voltage is measured using a P6015A probe made by Tektronix, Beaverton, OR, USA, while the current is measured by a Teledyne Lecroy produced CP031A high sensitivity AC/DC probe. This basic setup was used throughout all experiments, often coupled with further diagnostics such as a high speed camera or a trigger circuitry, allowing a temporal synchronization between the experiment and the diagnostic system.

## 3.3 Laser scattering

The measurement of plasma parameters, i.e. electron density and temperature as well as gas temperature, by means of laser scattering requires the usage of a high power light source [18]. Here, a Nd:YAG pulse laser of type Surelite SL II-10 made by Continuum, Santa Clara, CA, USA, is used. Coupled with a frequency doubler of type SSP-2, also produced by Continuum, pulses with a central wavelength of $\lambda_L$ = 532 nm and a width of 4-6 ns are generated [30]. As schematically presented in Fig. 3.4, the initial laser beam with a diameter of 7 mm and a full angle divergence of 0.5 mrad is diverted by 180° with two hard-faced 50 mm mirrors and focused onto the scattering volume using a planoconvex lens with a focal length of $f$ = 500 mm and a diameter of $d$ = 50 mm. This allows for a compact setup.

According to the theoretical considerations in section 2.1, to ensure the recording of the highest possible intensity of the scattered signal, the laser beam is polarized vertically and is perpendicular to the propagation direction of the scattered wave, while the scattering plane is chosen to be horizontal and also perpendicular to the beam polarization (compare Fig. 2.2). Such "square" setups are recommended for plasmas with low electron densities [83] and most commonly used in experiments [20, 70, 175]. Nonetheless, due to the large disparity of the scattering cross sections [47], special attention should be also paid to the optical sensitivity of the detection apparatus. A Fastie-Ebert spectrograph with a focal length of 250 mm is chosen for the experiments, coupled with an ICCD camera of type 4 Picos from Stanford Computer Optics, Berkeley, CA, USA, positioned in the image plane of the spectrometer.
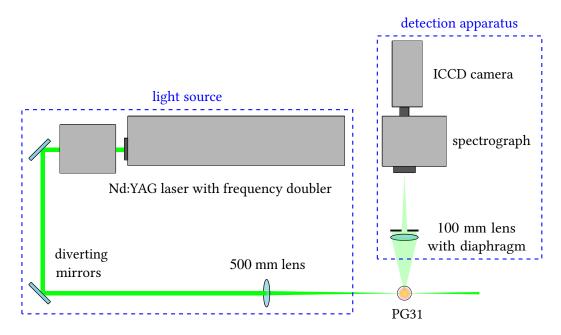


Figure 3.4: Schematic diagram of the experimental setup for laser scattering.

As shown in Fig. 3.4, the scattered beam is projected onto the horizontally oriented entrance slit by a 100 mm planoconvex lens coupled with a diaphragm to control the solid angle of the beam. The moderate focal length of the spectrograph combined with a diffraction grating of 1500 $l$/mm operated in the first diffraction order yields an aperture of f/4 on the one hand and still provides sufficient spectral resolution. On the other hand, the image intensifier of the camera, a Gen II photo-cathode of type S20 with a single-stage microchannel plate and a P43 phosphor screen optically coupled via an internal, distortion-free f/0.8 lens to a CCD chip with a resolution of $768 \times 576 \ px$, offers a quantum efficiency of about 11 % at a wavelength of 532 nm following the brochure [66]. Moreover, the ICCD camera allows external triggering - an important aspect for analysis of pulsed processes. The focal length of imaging lens is chosen so that distortion is minimized and the diaphragm is set to match

the aperture of the spectrograph to limit possible stray light. Lastly, the PG31 plasma generator is mounted on a motorized XYZ positioning unit, which simplifies adjustment and allows reproducible positioning during the experiments.

### 3.3.1 Calibration and settings

The detection apparatus, with an entrance slit width of the spectrograph set to 150 μm, is calibrated with a neon spectral calibration lamp of type 6032 made by Oriel Instruments, Stratford, CT, USA. A resolution of 0.055 nm/$px$ was obtained after evaluation of spectral lines observed at wavelengths of 533.08, 534.11 and 540.06 nm. The instrumental profile of the apparatus is determined as follows. An idealized transfer function of a spectrometer, assuming the entrance slit is illuminated homogeneously, is described by a square wave. Considering the spectral resolution, the linewidth of the laser can be assumed to be a Dirac excitation for the detection apparatus [30]. Moreover, the spatial intensity distribution of the laser beam within the scattering volume can be approximated by a two-dimensional Gaussian, what yields a one-dimensional Gaussian after projection onto the entrance slit. As a result, the slit is illuminated inhomogeneously. If a Gaussian profile is convoluted with an idealized rectangular transfer function of the spectrometer, the instrumental broadening of the entire apparatus can also be approximated by a Gaussian profile. Thereafter, the instrumental broadening of the whole detection apparatus can be estimated directly from the fit of the measured Rayleigh peak, as shown in Fig. 3.5. The FWHM of the instrumental function for the above settings amounts to 0.22 nm.
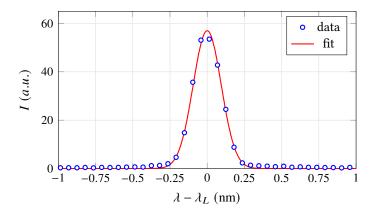


Figure 3.5: The instrumental profile of the detection apparatus determined by a Gaussian fit of the measured Rayleigh peak has a FWHM of 0.22 nm.

The images recorded by the ICCD camera not only contain spectral but also spatial information along the propagation direction of the laser beam. To determine the spatial resolution of the apparatus, the spectrometer's grating is rotated to the zero diffraction order and the entrance slit is fully opened. A calibration pin placed inside the nozzle with a diameter equal to the nozzle diameter of the plasma generator, i.e. 4 mm, serves as a marker. According to the above, a spatial resolution of 0.041 mm/$px$ was determined. Taking into account that the length of the focal point of the laser beam, i.e. the length of the measurement volume, does not exceed 2 mm, the region of interest in the acquired images is expected to be 50 $px$ or less wide. Because the region of interest is small compared to the width of the whole image, several aberrations exhibited by the simple Fastie-Ebert design as well as the curved focal field [75] can be neglected.

In addition to the experimental layout, the settings of the ICCD camera also play a crucial role in the acquisition process so that the images contain enough scattering signal to be evaluated. The sensitivity of the image intensifier module can be adjusted with the gain voltage applied to the microchannel plate, although the higher the voltage, the noisier are the recorded images. The intensifier used here works best with voltages between 700 V and maximal 1000 V. Based on preliminary tests, a gain

voltage of 800 V provides an optimal signal-to-noise ratio, which was kept constant for all following experiments. The exposure time is chosen so that the whole laser pulse is captured, but the stray light minimized. Stray light is caused by scattering from the surroundings and has a similar wavelength to the incident laser, which negatively affects the measurement results, especially when investigating plasmas with low electron densities. While the "square" orientation of the experimental setup already reduces stray light, it can be further minimized by shortening of the exposure time. The laser pulse has a duration shorter than 6 ns [30] and travels at a speed of approx. 0.3 m/ns. If an object-free space with a radius of 1.5 m around the measuring volume is assumed, approx. 10 ns are needed for a complete reflection. Therefore, if the exposure time of the ICCD is chosen shorter than the sum of both, the recording of the reflection can be excluded temporally. Considering the laboratory conditions and the jidder due to external triggering, an exposure time of 15 ns was set for the experiments. The delay between trigger input and exposure of the ICCD is adjusted according to the triggering circuitry, discussed in the next section.

Although precautions are taken to minimize stray light, it cannot be completely eliminated by temporal discrimination because the incident laser light is also scattered by objects or surfaces in direct vicinity of the measurement volume, such as the metallic surface of the nozzle tip. This stray light can be however estimated by comparing the measured scattering intensity on nitrogen with an additional measurement of scattering on helium [125, 163, 175]. Since the ground state of helium has one of the smallest scattering cross section [58, 70], an assumption is thus made that the detected intensity is only due to reflections from the surrounding objects. Thereafter, the measurement procedure for each parameter set consists of three steps. First, the stray light is evaluated by measuring of scattered intensity on helium flowing through the generator. The discharge is switched off in this step. In the second step, a cold gas measurement is performed to obtain a calibration profile of the scattering setup. During this step, pure nitrogen flows through the generator without the plasma being ignited. Accordingly, the acquired images contain a Rayleigh scattering signal as well as the stray light from the surfaces surrounding the measurement volume. Finally, a measurement is performed with the discharge switched on. The signal registered in this step consists of a Rayleigh scattering signal, a Thomson scattering signal and the stray light. All of the above measurements need to be pre-processed before evaluation of the plasma parameters. The pre-processing is described in section 3.3.3.

### 3.3.2 Triggering

The analysis of a pulsed process necessitates a temporal resolution. To achieve that, the plasma generator working in a frequency range between 40-65 kHz has to be synchronized with the laser pulse frequency of 10 Hz. Moreover, the laser frequency is fixed and cannot be adjusted. To synchronize both systems, the laser is operated in the so called direct access triggering mode [29]. Hereby the pumping flash lamps and the Q-switch are triggered with two separate TTL level signals and the delay between both signals is controlled externally. The required signals are generated by a pulse-delay generator in combination with an ancillary triggering circuit. The synchronization is based on the process voltage, which is tapped before the plasma generator (location B in Fig. 3.2).

The triggering circuit can be divided into several stages, as depicted in Fig. 3.6. Firstly, in order to protect the electronic components and the following equipment from interference caused by the ignition pulse of the plasma torch, the circuitry is disconnected from the power supply network with a high-voltage relay. After ignition, the relay is manually closed. The supply voltage is then divided by a resistive voltage divider, filtered and preconditioned with a unity gain buffer amplifier to obtain a signal amplitude suitable for TTL logic level components. The down-scaled, filtered voltage is compared with an adjustable threshold to create logic pulses. Thereafter, the delay time between exceeding of the threshold value and the output logic pulse can be adjusted, so that the complete period between two pulses can be sampled steplessly. The output of the TTL logic module is used as an external trigger input of a pulse-delay generator of type DG645 from Stanford Research Systems, Sunnyvale, CA, USA,
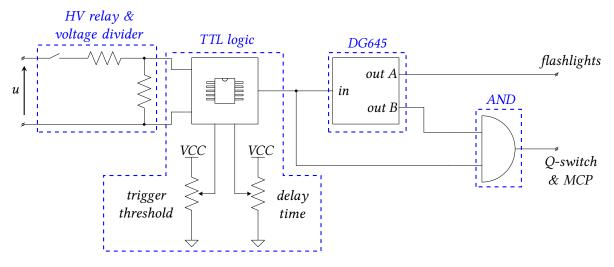
Figure 3.6: Simplified schematic of the triggering setup used for laser scattering.

which runs in advanced triggering mode. In this mode, a hold-off value specifies a minimum time allowed between successive triggers, and consequently the fixed frequency of 10 Hz required for the laser is provided. The DG645 provides thus an output signal for the laser pumping flash lamps and a preliminary Q-switch signal, as the rising edges of the flash lamps signal and the Q-switch signal should be within about 180 µs of each other [29]. Considering this time difference and the working frequency of the plasma system, the Q-switch signal needs to be synchronized again with the process to obtain the desired temporal resolution. Consequently, the preliminary Q-switch signal is thus logically conjugated via an AND-gatter with the input signal of the pulse-delay generator. Finally, the conjugated signal triggers the laser's Q-switch and is also used to trigger the MCP of the ICCD camera. As stated in section 3.3.1, the activation of the ICCD exposure is postponed by the camera software in relation to the trigger signal so that the maximal intensity of the laser pulse is acquired. This time shift is however in the nanosecond range and can hence be assumed insignificant compared to the other time scales in the experimental setup. With the triggering setup described above, the laser pulse is synchronized with the operating frequency of the plasma generator and the plasma parameters can be estimated at any point of the current waveform.

### 3.3.3 Data pre-processing

Dust and other particles in the ambient air of the laboratory cannot be avoided. However, the incident laser light is scattered by these particles due to the Mie scattering effect with different intensity [123], significantly stronger than Rayleigh or Thomson scattering signals. In addition, the Mie scattered light has a similar wavelength to the incident laser and thus influences the following estimation of the plasma parameters. To filter out the Mie scattering, the acquired images are sorted using a four-stage algorithm. In the first step, two regions of interest (ROI) are defined for each image - one containing only the plasma zone, marked red in Fig. 3.7, and one along the entire recorded laser line, marked green in Fig. 3.7. In the next step, an average intensity value for both ROIs is calculated for each image of a measurement and then graphically displayed. In addition to this, the intensity distribution for the respective single image is displayed in a separate graph. Thus, two histograms are created for each ROI - a distribution of the average intensity in the entire measurement and an intensity distribution for the currently analyzed image. By setting a lower and upper limit for each histogram, four validity ranges are defined. Only if the average intensity value of ROI 1 and ROI 2 as well as the intensity distributions of each ROI are within the defined validity range limits, an image is selected for further processing. Finally, an average image is created for the data evaluation.
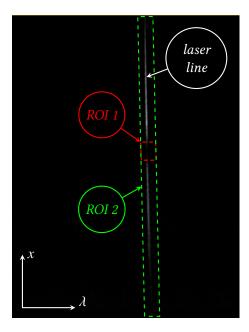
Figure 3.7: Typical scattering image explaining the sorting algorithm for the acquired images. ROI 1 contains the plasma zone, ROI 2 the complete laser line. The spatial coordinate is denoted by $x$, while $\lambda$ denotes the wavelength.

As stated at the end of section 3.3.1, the measurement procedure for each parameter set consists of three steps - a stray light measurement, a cold gas measurement and a plasma measurement. After an average image for each of the steps is created as described above, the average stray light image is subtracted from the others. As a result, pure Rayleigh scattered signal is obtained from the average cold gas image and a Thomson and Rayleigh scattered signal from the average plasma image. These two images are thereafter used to determine the plasma properties, as theoretically described in section 2.1.5.

## 3.4 Emission spectroscopy

Both, the measurement of the spectral broadening of hydrogen lines as well as molecular spectra require high spectral resolution. Thus, a similar experimental setup based on a Czerny-Turner spectrograph of type THR1000 made by Jobin-Yvon (now Horiba), Oberursel, Germany, with a focal length of 1000 mm and a diffraction grating of 1200 $l$/mm is used for both. The horizontally placed effluent plasma jet is projected through a 100 mm planoconvex fused silica lens onto the vertically oriented entrance slit as shown in Fig. 3.8. By mounting the plasma generator perpendicularly with respect to the entrance slit, each acquired image contains the spectrally resolved intensity distribution in the radial direction. Additionally, the generator is mounted on a positioning table to vary the axial distance $d$ from nozzle exit. The effluent plasma jet can thus be spatially scanned. Hence, the spectra are measured in 1 mm steps starting from nozzle exit. Lastly, the same 4 Picos ICCD camera as in the scattering setup is placed directly in the imaging plane of the spectrometer.

The instrumental profile is estimated by homogeneous illumination of the 100 μm wide entrance slit with a krypton spectral calibration lamp of type 6031 produced by Oriel Instruments, Stratford, CT, USA. For the spectral line at $\lambda_0 = 450.24$ nm, the resulting instrumental function has a FWHM of 0.1 nm as shown in Fig. 3.9. The spatial resolution is determined to be 0.07 mm/$px$. Additionally, an absolute calibration of the entire experimental setup is performed using a spectral radiance calibration standard, a frosted 50 W quartz-halogen lamp in an integrating sphere of type ISS-8P-HP-V01 made
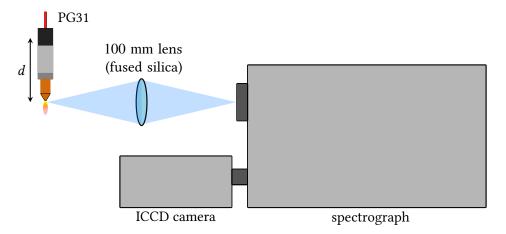
Figure 3.8: Schematic diagram of the spectroscopic experimental setup. The plasma generator PG31 is positioned perpendicularly to the vertically oriented entrance slit of the spectrograph.

by Gigahertz-Optik, Türkenfeld, Germany.

The hydrogen lines of the visible Balmer series, in particular $H_\alpha$ at 656.28 nm and $H_\beta$ at 486.13 nm are superimposed on the nitrogen spectrum, so to extract the lines both a pure nitrogen spectrum and a nitrogen-hydrogen spectrum are recorded consecutively. To reduce a possible influence of hydrogen addition on the plasma properties, but still achieve evaluable line intensities, a mixture of nitrogen and hydrogen of 99/1 $vol.$ % is used. Nonetheless, the gas flow is kept unchanged at 35 l/min. The molecular spectra are measured with pure nitrogen. The data evaluation for each case is discussed in section 3.4.2 and in 3.4.3 respectively.
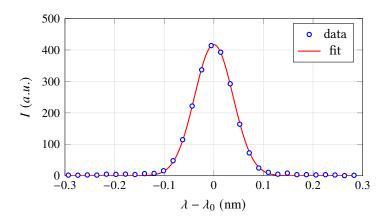


Figure 3.9: The instrumental profile of the spectroscopic setup determined by a Gaussian fit of a krypton emission line at $\lambda_0 = 450.24$ nm. The FWHM is 0.1 nm.

### 3.4.1 Triggering

The spectroscopic setup is triggered to achieve temporal resolution, as is the case of scattering diagnostics. The triggering circuitry is based on a simplified setup from section 3.3.2, since here only the image intensifier has to be triggered. Again, the circuit is separated by a high-voltage relay prior the ignition and afterwards the working voltage is scaled-down by resistive voltage divider as can be seen in Fig. 3.11. If the trigger threshold voltage is exceeded, a TTL pulse triggers the DG645 pulse-delay generator which is used to control the delay. Accordingly, the MCP of the camera is triggered with the pulse frequency of the plasma generator, utilizing the on-chip integration mode to

achieve a better signal-to-noise ratio. The gain voltage is fixed at 800 V, while exposure time of the MCP ranging from 40 ns to 2 μs has been varied according to the distance from nozzle exit.
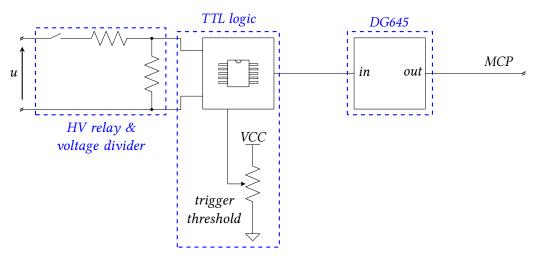


Figure 3.10: Simplified schematic of the triggering setup used for spectroscopic measurements.

### 3.4.2 Data evaluation of hydrogen lines

The same experimental setup was used to measure the broadening of the hydrogen lines as well as the molecular spectra. Thus, the first steps of data processing are also similar. The images are evaluated pixel line by pixel line. In both cases, an average image is first calculated from all recorded images for further processing and subsequently each pixel line is corrected with the according pixel line of the radiance calibration measurement. Afterwards, due to the fact that hydrogen lines are superimposed on the nitrogen spectrum, each nitrogen image is multiplied by a variable scaling factor and subtracted from the nitrogen-hydrogen image to obtain an image containing only the hydrogen line. According to Konjević *et al.* [92], Laux *et al.* [103] and Palomares *et al.* [141], the $H_\beta$ line represents a good compromise between acceptable signal-to-noise ratio and self-absorption, which can occur if the lines are too strong. It is also less dependent on the electron temperature and thus more suitable for electron densities in the range of $10^{21}$ m$^{-3}$, which are expected for the analyzed plasma. Hence, although both $H_\alpha$ and $H_\beta$ lines were measured, $H_\beta$ is used exclusively for the parameter evaluation.

The shape of the recorded hydrogen line is determined by a convolution of several broadening mechanisms. As discussed in section 2.2, the four most significant mechanisms are: broadening due to instrumental profile, Doppler, van der Waals (short vdW) and Stark broadening. The parameter evaluation is easiest if an assumption can be made that the Stark broadening is dominant. Then, the measured data can be approximated with a Voigt profile, a convolution of a Gaussian and a Lorentzian profile, where the width of the Gaussian component is taken as the width of the instrumental profile and the width of the Lorentzian component is taken as the Stark broadening. Both, the Doppler and vdW components are neglected as discussed in section 2.2.1 (Fig. 2.10). Thus, taking into account the experimental conditions, the implemented evaluation methodology is depicted in Fig. 3.11. At first the background nitrogen spectrum is subtracted from the hydrogen-containing measurement. Prior to fitting of a Voigt profile to the resulting data, the local intensity distribution of the hydrogen line is calculated using the Abel transform, assuming that the line is optically thin and axially symmetric. The assumption is in general valid if the whole effluent plasma jet, which can roughly be divided into two zones as discussed in section 3.1.2, is considered without a temporal resolution. On a short time scale however, especially in the region where the discharge is blown out of the nozzle, an assumption of rotational symmetry can only be made locally, i.e. for the region in direct proximity of the nozzle

Figure 3.11: Simplified mehtodology of the data evaluation of the $H_\beta$ line.

axis. The assumption is further supported by the fact that average images are used for parameter evaluation. Hence, only a radius range of 0.6 mm from generator axis is analyzed. Thereafter, the local $H_\beta$ profiles are fitted by a Voigt profile, where the Lorentzian component is varied to achieve the best possible fit of the measured data. With the so determined $\Delta\lambda_{lor}$, the electron number density is finally calculated using the approximation formula (2.75).

### 3.4.3 DATA EVALUATION OF MOLECULAR SPECTRA

Similarly to the evaluation of $H_\beta$, after an average image is calculated, corrected with the radiance calibration measurement and Abel transformed for local intensities, the nitrogen spectra are assessed. To determine the properties two molecular transitions in the visible range, the $C^3\Pi_u \rightarrow B^3\Pi_g$ transition of the excited nitrogen molecule called second positive system (short SPS) and the $B^2\Sigma_u^+ \rightarrow X^2\Sigma_g^+$ transition of the ionized nitrogen molecule called first negative system (short FNS), are used.

According to equation (2.82), the emitted light intensity depends on the transition energy as well as number density of the emitting species. Thus, by comparing amplitudes of the vibrational peaks a relative ratio of densities of both emitting species can serve as a very rough estimation of the energy distribution in the plasma [87]. For nitrogen the most relevant vibrational transitions can be observed between 310 nm and 430 nm [99, 110]. Depending on the experimental setup, it is usually not possible to register at once such a wide spectral range with sufficient resolution required for temperature determination. One could try to string several wavelength ranges together, but it can be cumbersome with high resolution setups and requires very precise work from the experimenter. In case of nitrogen however, the wavelength range around 357 nm shown in Fig. 3.12 can be used due to the overlap of SPS and FNS transitions.

Thereafter, the $(0, 0)$-SPS-transition with the band head at 337.13 nm, the $(0, 0)$-FNS-transition with the band head at 391.44 nm (shown in Fig. 2.12) and a mixing range around 357 nm, where the $(1, 0)$- & $(2, 1)$-transitions of SPS are superimposed with the $(0, 1)$- & $(1, 2)$-transitions of FNS, are acquired with the experimental setup. Each pixel line of the locally resolved spectra is then imported to Specair. Here, the synthetic spectra calculated by the software under assumption of $T_{rot} = T_{vib}$, as discussed in section 2.2.5, are broadened with the instrumental profile of the experimental setup shown in Fig. 3.9. The temperatures estimated for the $(0, 0)$-transitions of both systems are then used

to assess the relative density ratio of $n_{N_2}$ to $n_{N_2^+}$. Each data point presented in section 4.3.2 is a mean value of three separate measurements.
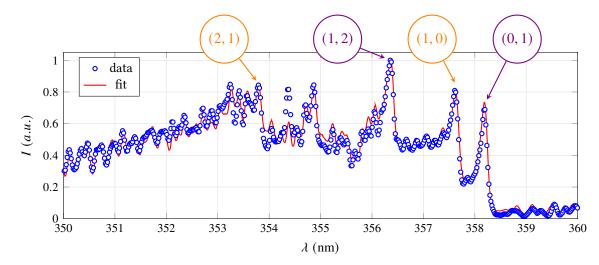


Figure 3.12: A relative ratio of densities of SPS and FNS is estimated based on the vibrational transitions around 357 nm. The SPS transitions are marked in orange, the FNS in purple.

## 3.5 Further optical diagnostics

For a better understanding of the effects observed with the methods presented above, the discharge is examined with additional diagnostic setups. The methods presented within this section are based on a high speed camera that records the behavior of the discharge channel blown out of the nozzle. In most cases, current and voltage waveforms are recorded synchronously with the images, though the camera is not triggered by the pulses of the power supply as was previously the case.

To visualize possible instabilities in the effluent plasma jet, Schlieren imaging is set up as described in section 3.5.1. In addition to that, the behavior of the cathodic attachment point is studied with an arrangement described in section 3.5.2 as well as the spatial behavior of the discharge channel with a different setup explained in section 3.5.3.

### 3.5.1 Schlieren imaging

As stated by Traldi *et al.*, Schlieren imaging is a powerful diagnostic tool for atmospheric pressure plasmas [172]. Schlieren imaging, named so by Toepler in the nineteenth century [156], is method which allows to detect changes in the refractive index of a transparent medium. In the simplest case, the refractive index depends on the density of the gas according to the Gladstone-Dale relation and thus depends on pressure and temperature according to ideal gas law. If one of the quantities changes, the light rays passing through the transparent medium are refracted in different directions by the refractive index gradients. The refracted rays can then be filtered out by a spatial filter after the light beam is focused, resulting in a shadowing of that area on the image plane.

Several optical setups to visualize the refractive index gradients were developed over time, though the most commonly used setup for plasma studies is the Z-type arrangement as depicted in Fig. 3.13 [172]. In this work, the setup is based on parabolic mirrors with a focal length of 1219 mm and a diameter of 152 mm made by Edmund Optics, Barrington, NJ, USA. Parabolic mirrors offer satisfactory optical quality and are less expensive to manufacture than lenses for viewing areas larger than 100 mm [172]. To minimize possible aberrations, mirrors with long focal lengths and $f$-numbers of $f/6$ or higher are preferred [156]. Furthermore, the mirrors should be tilted to opposite sides mimicking the shape of the

letter Z (hence the name), with the tilt angle being as small as possible. The above conditions are met by the chosen mirrors and implemented setup, as shown schematically in Fig. 3.13. To illuminate the effluent plasma a point-like light source, a Xenon lamp XBO-150W made by Osram GmbH, Munich, Germany, positioned in the focal point of the first parabolic mirror is used. The so created parallel light beam passes through the plasma jet and is focused with the second parabolic mirror onto the spatial filter, often called knife edge, which blocks part of the refracted light rays. Finally, the Schlieren images are recorded with a high speed camera of type pco.dimax HS4 made by PCO AG, Kelheim, Germany coupled with a 100 mm lens with an maximal aperture of $f/2$ made by Carl Zeiss AG, Oberkochen, Germany. With this setup, thanks to the intensive illumination of the arc lamp, frame rates of over 40000 images per second can be reached at exposure times as short as 2 μs. The setup was used previously to investigate welding arcs by Siewert *et al.* [157].
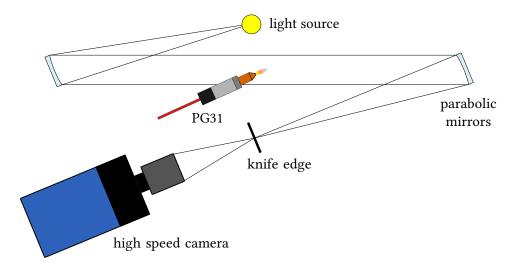


Figure 3.13: Schematic diagram of the Schlieren setup. A Z-type arrangement is used with parabolic mirrors, similar to the one used in [157].

Schlieren imaging is, as indicated in Fig. 3.13, an integrative technique, i.e. the refractive index gradients are integrated in the direction of the light beam. Thereafter, if quantitative results are to be obtained from a measurement, an Abel transform should be applied to the images assuming the effluent plasma is axially symmetric [172]. For highly turbulent gas flows, reconstruction of the distribution of refractive index gradients in the direction of integration that led to the resulting image is difficult. Furthermore, the Gladstone-Dale relation describing the refractive index is much more complex in plasma environments and depends not only on the density of neutrals, but also on the density of ions and electons as well as their polarizability as described by Merzkirch [120]. According to Traldi *et al.*, the effects are increased for plasmas in non-equilibrium [172]. Thus, quantitative analysis of Schlieren images is difficult, and since this diagnostic method is not the focus of this work, the recorded images will be evaluated only qualitatively. For a detailed description it should be referred to the books of Settles [156] and Merzkirch [120].

### 3.5.2 High speed imaging

A direct discharge between two electrodes, even if sustained by a relatively low current density, will erode the surface of the electrodes over time. Generally speaking, electrode degradation is caused by energy losses required to sustain the discharge [147]. The cathode surface has to be heated to emit the electrons required to sustain the discharge. The anode is in turn heated by absorption of electrons and recombination processes. Depending on the electrode material, the intense and often only localized heating of the electrodes can lead to particle emission, material evaporation, sputtering or oxidative

degradation of the surface, the main electrode erosion mechanisms [55, 64, 77, 147]. Depending on the current density, different energy amounts may be dissipated in each of the electrodes [77, 147]. For low-current discharges, it is assumed that most of the energy is spent on electron emission from the cathode material [147]. Thus, a faster erosion rate of the cathode, i.e. of the nozzle of the PG31 plasma generator, is expected over time.



Figure 3.14: Schematic diagram of the high speed imaging setup. The camera is angled directly onto the outlet of the PG31 plasma generator and is synchronized with the voltage and current traces via the exposure time signal $t_{c,exp}$.

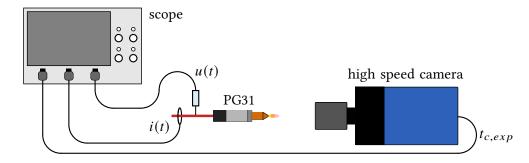According to the above, the temporal progression of the cathodic attachment point is studied by high speed recordings with a simultaneous voltage-current measurement. The camera is thereby directed straight onto the nozzle outlet as schematically shown in Fig. 3.14. The pco.dimax HS4 and the 100 mm lens are used again for image acquisition. The captured images are correlated with the voltage and current waveform by a simultaneous measurement of the electrical traces and the exposure time signal of the camera, denoted with $t_{c,exp}$. An oscilloscope of type HDO8108A is used for this purpose, together with a P6015A voltage probe and a current probe of type CP031A (see sect. 3.2).

### 3.5.3 HOBAS-3D imaging system

Apart from the simple setup from previous section, another high speed imaging system named HOBAS, an abbreviation from the german name **HO**chgeschwindigkeits**B**ild**A**ufnahme**S**ystem, is used to study the behavior of the discharge channel. Though, as will be described later on, slightly modified in comparison to the original version developed by Forster and Schein [154], so that the images can be reconstructed three-dimensionally.

The HOBAS system enables an acquisition of short film sequences at recording speeds of up to $10^6$ frames per second with exposure times in the range of a few nanoseconds. To achieve such high recording speeds an image intensifier gated by a rotating mirror is used as schematically shown in Fig. 3.15. Both, a separate image intensifier module coupled with a camera or an integrated intensified camera can be used, depending on which equipment is available. Although an integrated camera is depicted in Fig. 3.15 for the sake of clarity, a separate intensifier module of type Quantum Leap equipped with a S25 photocathode, produced by Stanford Computer Optics, Berkeley, CA, USA, coupled with the pco.dimax HS4 camera is used in the experiment. The projection of the analysed object, the effluent of the plasma generator PG31, is moved across the sensor plane of the image intensifier by a rotating mirror. Thus, the shift $\Delta x$ between each on-chip projection depends the rotation speed $\omega$. Furthermore, $\Delta x$ depends also on the object distance to the imaging sensor $\Delta z$ and on the trigger timing. The distance between the rotating mirror and the image intensifier is thereby fixed and kept as short as possible. The shorter $\Delta z$ is, the faster the mirror has to rotate so that the image projections do not overlap. The time delay $\Delta t$ between two successive trigger points $t_{1..n}$ has to be longer than the exposure time $t_{i,exp}$ of the image intensifier, otherwise the projections will overlap (see Fig. 3.16). In general, the exposure $t_{i,exp}$ should be chosen as short as possible to minimize possible motion blur in

Figure 3.15: Schematic principle of operation of the HOBAS system after [154]. The projection of the plasma generator PG31 is moved across the ICCD by a rotating mirror, while the camera is operated in an integrate-on-chip mode.

the acquired images. The delay time allowed by the image intensifier module used in the experimental setup cannot be set shorter than 1 µs. The possible exposure times, on the other hand, can be as short as 1.2 ns [65]. According to the above, the resulting image recorded by the camera contains $n$ projections of the observed object as shown in Fig 3.16.

As can be deduced from Fig. 3.16, the acquisition time is limited by the physical size of the image intensifier's photocathode. To achieve longer acquisition times, the image reproduction has to be adjusted, i.e. reduced accordingly. The 100 mm lens, the same one as in section 3.5.2, is used again as imaging optics in the experiment resulting in rotation speeds ranging from 12000 to 18000 revolutions per minute and a spatial resolution of 0.4 mm/$px$ at a distance $\Delta z$ of about 1.5 m. Similarly to the previous section, the voltage and current traces are measured in parallel with the HOBAS image sequences to provide a better understanding of the observed effects as well as to reveal possible correlations. The same setup as in section 3.2 is used to perform the electrical measurements.
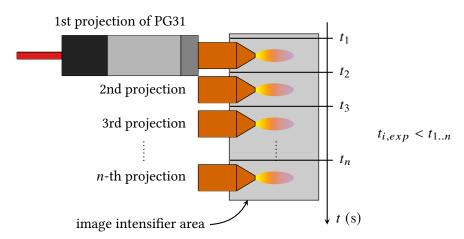


Figure 3.16: The image intensifier is gated at points of time from $t_1$ to $t_n$ with an exposure time $t_{i,exp}$ shorter than the gating time, while the camera shutter is open. Thus, the HOBAS image contains $n$ projections of the plasma generator, depending on the rotation speed of the mirror and gating frequency of the intensifier.

Due to the relatively small size of the discharge channel, the HOBAS setup can be modified to record additional projections from different viewing angles, which subsequently allow a three-dimensional

reconstruction of the measured object. The additional projections are created by two mirrors mounted at an angle of 22.5° behind the PG31, as depicted in Fig. 3.17. In this way, the object is observed from three different viewing directions: −45° (projection I in Fig. 3.17), 0° (projection II) and 45° (projection III). The depth of field for this kind of setup should be selected so that all three projections are in focus. At a distance of $\Delta z$ of 1.5 m, the depth of field even at the widest aperture of the used lens is sufficient to reproduce all projections in focus.
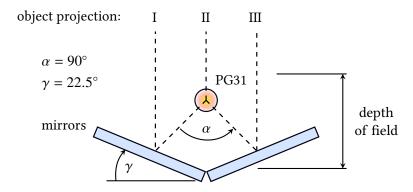


Figure 3.17: By adding two mirrors behind the analyzed object, further viewing directions can be recorded in a HOBAS image. The projections I-III are used thereafter for a three-dimensional reconstruction of the plasma.

An object can be reconstructed three-dimensionally based on the Radon integral transformation. According to the Radon theory [16], a projection $p(\phi, a)$ can be calculated by integration of a two-dimensional function $f(x, y)$ along a straight viewing line $L_{\phi,a}$. Thus, for a reconstruction an inverse transformation has to be calculated. To do so, several $n_a$-sized projections from $n_\phi$ different viewing angles are necessary [89]. Thereafter, a linear system with $n_a \times n_\phi$ equations and $n_a \times n_\phi$ unknowns has to be solved. Even with today's computing power, solving of such an equation system is time consuming. Because of that, iterative solution methods are usually used. Here, similarly to the works of Kirner [89, 164], the so-called algebraic reconstruction technique (ART) is applied. Furthermore, the plasma is assumed to be optically thin. A similar assumption is made in case of the laser scattering diagnostics as well as for Abel transform of the spectroscopic measurements. To reconstruct most details of a complex object, usually many projections are used for the calculations [89]. However, the iterative algorithm allows to reduce the number of projections if the quality requirements of the reconstruction may be lowered. Since the discharge channel observed here has a comparatively simple shape, it has been found that three projections are sufficient to achieve a satisfactory quality. For an in-depth description of the tomographic reconstruction algorithm it should be referred to [16, 89], as it is beyond the scope of this work.

# 4

# Experimental results and their interpretation

In the following chapter, the results of all experimental methods are presented. All experiments have been carried out with pure nitrogen flowing at a rate of 35 l/min, except for hydrogen line broadening, where a mixture of nitrogen and hydrogen of 99/1 $vol.$ % is used. The first section 4.1 compiles the results of a current-voltage analysis, on the basis of which two working frequencies were selected for further investigations. These two working points are then thoroughly examined with laser scattering and the results are presented in the section 4.2 of this chapter. The third section contains the outcome of spectroscopic diagnostics, which are used as a comparison to the results of laser scattering in section 4.2. The last section 4.4.2 summarizes the insights obtained from observing the movement of the discharge channel using the methods described in section 3.5.

## 4.1 Voltage and current analysis

The power source of the examined plasma system allows an adjustment of two parameters - the power setting and operating frequency. The power setting corresponds to the amplitude of the current, whereas the operating frequency adjusts the time between two current pulses as the rise and fall times are fixed at 5 µs. Typical traces for pulse frequencies of 43 kHz and 60 kHz and a power setting of 100 % are presented in Fig. 4.1. Since the edge times are kept constant, only a period of 16 µs is depicted. The solid lines represent an average value, while the dashed lines represent the minimum and maximum values within the analyzed range. As stated in section 3.1, both voltage and current traces were measured at the exit of the power supply, denoted by the subscript "$supply$", and shortly before the plasma generator, correspondingly denoted by "$gen$".

As expected, $i_{supply}$ increases independently of the frequency and without significant deviations. The voltage $u$ in Fig. 4.1 also increases with a similar slope and without deviations for both presented frequencies, but with a time delay in regard to $i_{supply}$ indicating a typical behavior for the charging process of a capacitor. The current measured prior to the plasma generator, $i_{gen}$, is shifted even further related to $i_{supply}$ and corresponds well to the falling edge of the voltage indicating a typical discharge behavior of a capacitor after short-circuiting or reaching of the breakdown voltage. Regardless, the voltage is independent of the measurement position. The time shift between maximum value of the current peak at source exit and the maximum value of the voltage is approximately 1.5 µs, while the current peak measured near the generator is shifted further by about 1-1.5 µs depending on the pulse frequency. Additionally, the variation of the peak voltage value, different falling voltage slopes, different peak values of $i_{gen}$ as well as the hump and higher deviations from average on the falling edge of $i_{supply}$ all indicate a frequency-dependent behavior of the system.
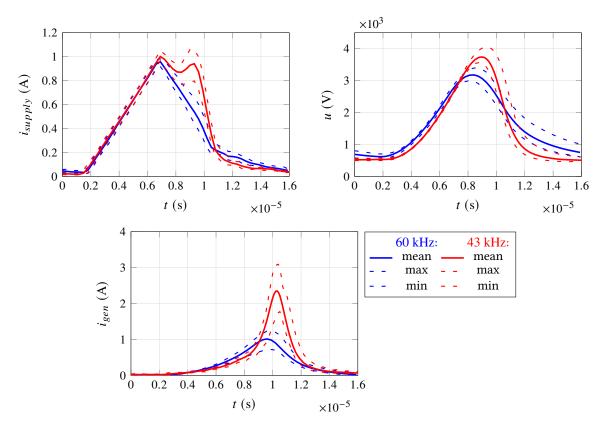
Figure 4.1: Typical voltage and current traces recorded at both connection points of the system for operating frequencies of 43 kHz and 60 kHz and a power setting of 100 %.

A more comprehensive statistical analysis of the traces is shown in Fig. 4.2, where the values for each pulse are calculated separately, then averaged and plotted. Looking at peak voltage $U_{peak}$ as well as valley voltage $U_{valley}$, i.e. the minimal voltage between two pulses, no significant differences are observed between the two measurement positions as discussed above. The voltage peak value, corresponding to the breakdown voltage across the discharge channel, reduces with increasing pulse frequency from almost 4.0 kV to about 3.2 kV. The amplitude of the valley voltage stays constant at about 500 V up to 55 kHz and increases slightly for higher frequencies. A different behavior is observed for the current traces. Whereas the $I_{peak}$ values at the exit of the power source can be assumed to be constant at 1 A, corresponding to the maximal amplitude emitted by the power supply, as can be the valley current values $I_{valley}$ at 50 mA in that position, the current peak values measured in the proximity of the plasma generator increase significantly with decreasing frequency reaching a maximum of about 2.8 A at a frequency of 43 kHz. When measuring in this position, negative valley current values are observed indicating the transmission line characteristics of the coaxial connection. This frequency dependence of the load, i.e. of the plasma generator coupled with the triaxial high voltage cable, implies that a simultaneous power increase with rising frequency cannot be assumed. To analyze the power consumption of the system, energy per pulse $E_{pulse}$, being the integral of the instantaneous power over one pulse, and the charge per pulse $Q_{pulse}$, being the integral of instantaneous current over one pulse accordingly, are calculated and presented in Fig. 4.2. As stated in section 3.1, the maximal charge per pulse for an ideal triangular shaped current pulse is 6.5 μC. At the exit of the supply, an almost identical $Q_{pulse}$ is measured up to 55 kHz and decreases slightly thereafter. A different behaviour is nevertheless registered at the generator, where the charge values are reduced by over 15 % compared to the supply's output from a frequency of 45 kHz onwards.

Correspondingly to the voltage increase with decreasing frequency, the highest energy per pulse is consumed for the lowest value of 40 kHz. Moreover, a reduction of about 10 % in energy of each pulse at the plasma generator is observed when the frequency rises from 50 kHz towards higher values.
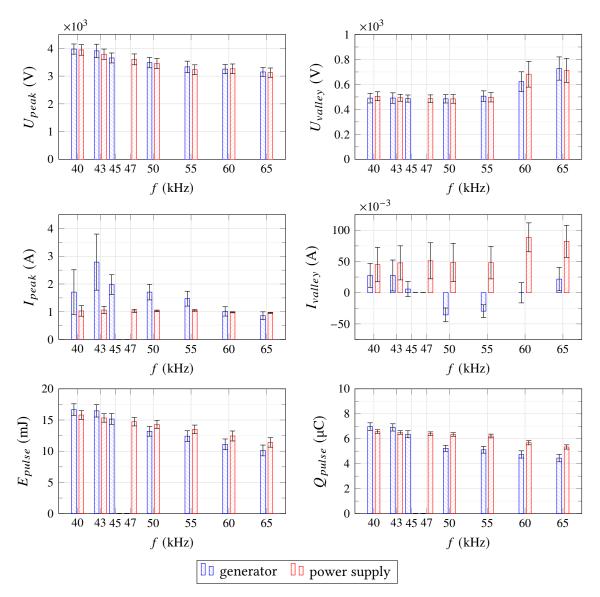


Figure 4.2: Results of the voltage and current traces analysis for the full available frequency range at a power setting of 100 %.

Concluding, it can be stated that the largest differences are observed in the current amplitude. Accordingly, two operating points are chosen for further examination - a pulse frequency of 43 kHz, at which the largest difference in peak current values between the connection points of the system is registered, and a pulse frequency of 60 kHz, at which the current peak values are equal.

## 4.2 Laser scattering results

As described in section 3.3, average images are used to evaluate the relevant plasma parameters at the two above suggested operating frequencies of 43 kHz and 60 kHz. The plasma parameters are evaluated furthermore for different trigger time points and two values of the power setting of the investigated plasma system. The scattering measurements are carried out in such a way as to obtain

a spatial distribution of the parameters, whereby the distribution in the radial direction is assessed directly for each pixel line of the plasma ROI shown in Fig. 3.7. To achieve axial resolution the plasma generator is moved in the according direction with the motorized positioning unit. Before a parameter study is started, the position of the plasma generator is adjusted so that the incident laser beam passes exactly through the generator axis. Each setting of the power supply is measured at least three times at a given position, evaluated and a mean of the results created. The plasma system is run constantly at a power setting of 100 % and the scattering setup is triggered to record the plasma parameters reached at the peak current, except for section 4.2.2 where the temporal distribution of the plasma parameters and section 4.2.3 where the influence of the power setting are evaluated. As it turned out, electron
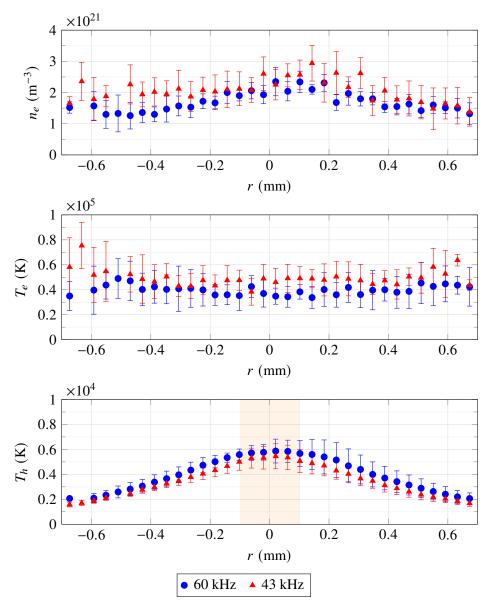


Figure 4.3: Plasma parameters ($n_e$, $T_e$, $T_h$) at an axial distance of $d = 1$ mm for different pulse frequencies estimated from scattering measurements.

parameters can be reliably estimated for a radial distance perpendicular to the jet axis of 0.7 mm and up to a axial distance of about 7 mm downstream from the nozzle outlet when operating with a frequency of 60 kHz, and up to 5 mm downstream when the current is pulsed at 43 kHz. Further downstream, only an estimation of the heavy particle temperature based on the Rayleigh scattering is

possible. A typical radial distribution of the estimated plasma parameters for a distance of $d = 1$ mm from nozzle exit is shown in Fig. 4.3.

The radial distribution of the electron number density depicted in Fig. 4.3 varies by about $0.7 \times 10^{21}$ m$^{-3}$ between the jet axis and the outer fringes at radii above 0.6 mm at the operating frequency of 60 kHz, an increase of slightly more than 30 %. It should be noted that the maximum value of $2.3 \times 10^{21}$ m$^{-3}$ is reached about 0.1 mm outside the axis. Looking at the error bars, a deviation of 25 % from the average $n_e$ value is to be expected throughout the analyzed diameter. In contrast, a significant increase of the electron temperature with varying radius is not observed. A mean $T_e$ value of 41000 K is estimated with a similar deviation of about 25 %. The temperature of heavy particles in turn shows a significant, Gaussian-like radial distribution when the generator is operated with 60 kHz, with a maximum value of 5800 K lying at jet axis and a negative gradient of $\sim$ 3000 K/mm towards larger distances from the axis. Also, an approx. 0.2 mm wide temperature plateau can be observed around the axis, as marked in Fig. 4.3. Analogously to other plasma parameters the standard deviation ranges about 25 % in the case of $T_h$, although it decreases with increasing radius. The figure 4.3 also depicts the radial distributions estimated for an operating frequency of 43 kHz. The progression of the data points is almost equivalent as for 60 kHz, whether $n_e$, $T_e$ or $T_h$ is considered, whereby the amplitudes are shifted towards higher or lower values on average. And so, the zone where the maximal electron density of $2.5 \times 10^{21}$ m$^{-3}$ on average is reached for a frequency of 43 kHz, is also slightly offset from nozzle axis. Moreover, virtually all $n_e$ values at 43 kHz are higher than those measured at the higher frequency of 60 kHz. If the $T_e$ values for $r > \pm 0.6$ mm are considered as outliers, than no significant changes in electron temperature are observed throughout the analyzed range and an average of 49000 K is reached, a value 8000 K higher than for 60 kHz. The temperature of heavy particles is in contrast slightly lower than previously, with an maximal value of 5300 K reached on nozzle axis. Similarly to the the higher operating frequency, a standard deviation of 25 % can be assumed also for 43 kHz.

Since the radial distributions, especially those characterizing the electrons, do not change significantly within the analyzed radial range, it seems sufficient for the sake of clarity to compare only the mean values in the following. Hence, an average $n_e$ and $T_e$ is calculated from the whole analyzed radial range. The mean $T_h$ value is however calculated only for values within the plateau marked in Fig. 4.3. The average values are denoted as $\overline{n}_e$, $\overline{T}_e$ and $\overline{T}_h$.

### 4.2.1 AXIAL DISTRIBUTION OF THE PLASMA PARAMETERS

The mean $\overline{n}_e$, $\overline{T}_e$ and $\overline{T}_h$ values at different axial distances from nozzle exit are presented in Fig. 4.4. The difference in electron number density between the studied frequencies described above, which is observed for a distance of 1 mm, is only present in the immediate vicinity of the nozzle exit. The presented $\overline{n}_e$ value of $1.7 \times 10^{21}$ m$^{-3}$ at $d = 1$ mm is lower than stated in the previous section, as it represents the average value over the entire radial range. Electron densities estimated for 2 mm and 3 mm are only marginally higher for the slower pulsed process and, similar to the data points further downstream, can be assumed to be constant at about $1.5 \times 10^{21}$ m$^{-3}$ when the standard deviation is taken into account. The progression of the axial distribution of the electron temperature is somewhat different. The values decrease for both frequencies at a rate of approx. 10 %/mm up to a distance of 3 mm. Throughout this distance range, the electron temperatures estimated for the lower operating frequency are about 15% higher than for 60 kHz. Thereafter, $\overline{T}_e$ reaches about 43000 K in both cases and can be assumed to be constant up to 7 mm for the higher frequency. The temperature of heavy particles on the contrary is higher for the higher working frequency over the entire range of distance studied. It should be also noted, that the $\overline{T}_h$ values vary only insignificantly around 5900 K up to 5 mm for the higher and around 5200 K up to 3 mm for the lower frequency. The temperature starts to decrease slowly from there on in both cases.
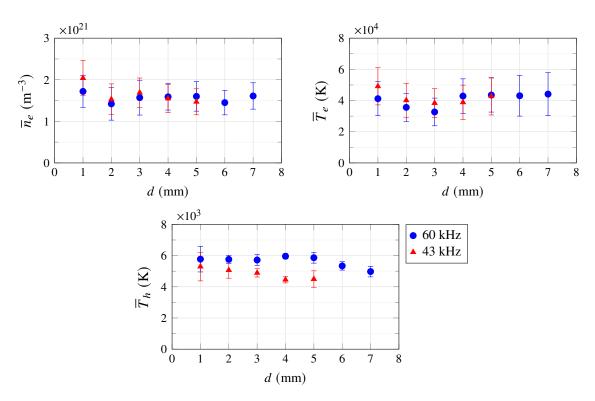
Figure 4.4: Mean electron density ($\overline{n}_e$) and particle temperatures ($\overline{T}_e$, $\overline{T}_h$) estimated for different axial distances $d$ downstream from nozzle outlet.

To assess the temperature of heavy particles at larger distances, further measurements were undertaken for the process pulsed with 60 kHz. A full spatial distribution of $T_h$ up to a distance of 17 mm from nozzle exit is shown in Fig. 4.5. The distribution can be roughly divided into two zones, a 8 mm long inner finger-shaped zone with a diameter of about 0.5 mm and an almost constant core temperature of 5900 K up to 5 mm and a 12 mm long, 1 mm in diameter zone with a temperature around 3000 K. For further distances, the temperature value drops to 1000 K.
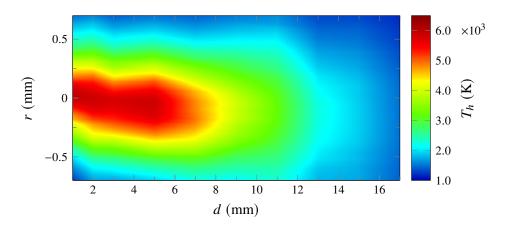


Figure 4.5: Spatial distribution of the heavy particle temperature estimated based on Rayleigh scattering for a frequency of 60 kHz.

### 4.2.2 Temporal distribution of the plasma parameters

The circuitry described in section 3.3.2 not only synchronizes the laser pulse frequency with the operating frequency of the plasma system, but also allows to trigger the laser scattering setup at different points of time of a current pulse. By doing so the temporal distribution of the plasma parameters is assessed. The parameters are examined at four trigger timeframes stretching across a current pulse as depicted in Fig. 4.6. Since the plasma system operates without a control loop, which implies fluctuations in plasma and thus in the measured electrical signals as described in section 3.1.2, no exact trigger time points can be defined. Accordingly, the width of the timeframes in Fig. 4.6 illustrates approximately the jitter of the trigger time point.
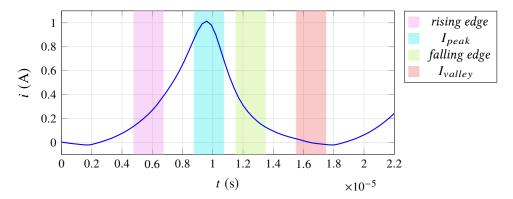


Figure 4.6: Trigger timeframes at which the scattering setup was triggered to assess the temporal distribution of the plasma parameters in relation to a current pulse.

The temporal distribution is analyzed for both operating frequencies at an axial distance of 1 mm from nozzle exit. Similarly to the analysis of the axial distribution in the previous section, the results presented in Fig. 4.7 are averages calculated from the full radial range. The first thing to notice when looking at the results for a pulse frequency of 60 kHz is that the amplitudes of the plasma parameters follow the current trajectory, i.e. the maximum values are measured for the peak current timeframe $I_{peak}$. As shown the Fig. 4.7, the electron number density correlates well with the current trajectory reaching an average value of $1.7 \times 10^{21}$ m$^{-3}$ at $I_{peak}$. From there, the electron density follows the current trajectory with an almost linear decrease from the current peak towards the rising edge of the next current pulse. Here, an almost 24 % reduction is observed compared to the maximal $\overline{n}_e$ value. A sort of similar behavior is observed for the mean electron temperature $\overline{T}_e$, although the values remain unchanged at the current minimum after an initial reduction of 5 % for the falling edge. Again, the lowest mean temperature, which is about 15 % lower than at $I_{peak}$, is estimated for the rising current edge. Looking at the mean heavy particle temperature $\overline{T}_h$ an almost linear decrease is observed from $I_{peak}$ towards the current minimum, where the temperature is reduced by about 15 %. The lowest temperature of approx. 4800 K is estimated for the rising edge of the following current edge, giving a reduction of 18 % when compared to the maximum at $I_{peak}$. The behavior of the plasma parameters estimated for the lower operating frequency does not correlate so well with the current trace as before.

According to the results in Fig. 4.7 only the mean electron number density follows the current progression with a maximal value of $2.0 \times 10^{21}$ m$^{-3}$ reached at the current peak when the process is pulsed with 43 kHz. Thereafter, the electron density decreases about 10 % while the current is falling towards the minimal current value $I_{valley}$. The $\overline{n}_e$ values recorded for the rising edge are almost identical to those estimated for $I_{valley}$ and almost 15 % lower than for peak current. The mean electron temperature on the other hand behaves differently with the highest value of 53000 K registered for the rising edge of the current pulse, about 10 % higher than for peak current. The temperature decreases by further 10 % for the remaining two timeframes. Also the $\overline{T}_h$ values progress differently than at 60 kHz. The highest heavy particle temperature of almost 5900 K registered for the falling current

edge, over 10 % higher than at $I_{peak}$. A 5 % lower temperature is recorded for the current minimum $I_{valley}$ when compared to the value estimated for $I_{peak}$ and does not change while the current is rising, showing somewhat similar behavior to $\overline{n}_e$ for these two timeframes.
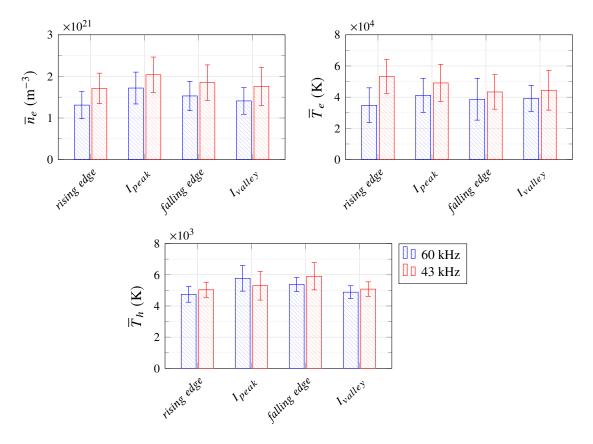


Figure 4.7: Temporal distribution of the mean plasma parameters for both studied frequencies at a power setting of 100 % and axial distance $d = 1$ mm.

In summary it can be stated that the temporal distribution of the plasma parameters follows the progression of a current pulse well for a working frequency of 60 kHz. However, at a working frequency of 43 kHz, this is only the case for the distribution of the electron number density as the particle temperatures show a different behavior.

### 4.2.3 Distribution of plasma parameters for different power settings

Apart from the frequency, the PS2000 power supply allows for an adjustment of the output amplitude of the current pulses. To further assess the operation of the system at different frequencies, an attempt is made to evaluate the distribution of the plasma parameters for different power settings as well. In order to not overcomplicate the analysis, only two power settings, 85 % and 100 %, are compared. The trigger timeframe is set to $I_{peak}$ and the distance from nozzle to 1 mm. The results compiled in Fig. 4.8 represent the mean values, similar to previous sections.

By reducing the power setting from 100 % to 85 % the mean electron number density decreases regardless the operating frequency, although a much more significant reduction of over 20 % is observed when the discharge current is pulsed with 60 kHz. The reduction of $\overline{n}_e$ for the lower operating frequency is in the range of about 10 %. Interestingly, contrary to $\overline{n}_e$, no change in mean electron temperature is observed when the power setting is changed at 60 kHz, while it decreases by about 20 % when operating at 43 kHz. In addition, a change in the current amplitude at the output of the power source entails a reduction in the average temperatures of heavy particles, almost 10 % for a

working frequency of 60 kHz and 14 % for a frequency of 43 kHz. Moreover, it should be noted that the estimated $\overline{\overline{T}}_h$ values are higher when operating at 60 kHz for both power settings.
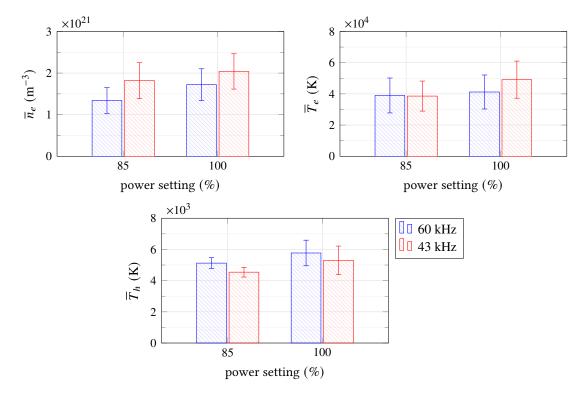


Figure 4.8: Mean plasma parameters estimated for different power settings at an axial distance of 1 mm from nozzle exit while the scattering setup is triggered at $I_{peak}$.

## 4.3 Emission spectroscopy

### 4.3.1 Electron density estimation based on line broadening

Similar to the laser scattering experiment, the broadening of hydrogen lines is measured for both working frequencies studied, although only for a power setting of 100 %. Moreover, the experimental setup is triggered at the peak value of current. After recording, the spectra are evaluated as described in section 3.4.2.

The estimated electron number densities when operating at 60 kHz increase insignificantly in the axial direction up to about 3 mm downstream from nozzle exit, denoted as $d$ in Fig. 4.9. After consideration of the measurement error, the density can be thus assumed to be constant at $0.52 \times 10^{21}$ m$^{-3}$ for distances $d < 3$ mm and $r < 0.3$ mm. Thereafter, the values decrease for larger distances from nozzle exit. The radial distribution of the electron number density increases somewhat unexpectedly by about 17 % towards larger radial positions $r$. The spatial distribution of $n_e$ determined for the lower working frequency of 43 kHz, also presented on the right-hand side in Fig. 4.9, displays a similar character as for 60 kHz with maximal values measured at a distance of 2 mm. It should be noted that the density rises by approx. 32 % in radial direction, almost twice as much as before. Most significantly, all $n_e$ values are nearly twice as high across the whole spatial range reaching an average of $0.95 \times 10^{21}$ m$^{-3}$ compared to the higher operating frequency.
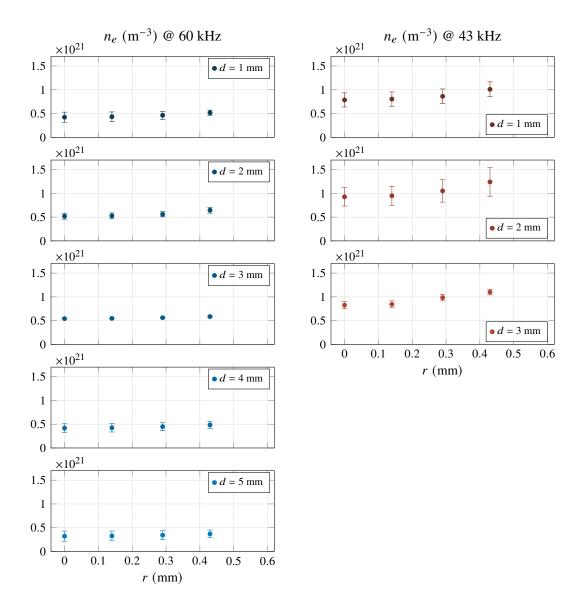
Figure 4.9: Spatial distribution of the electron density estimated from hydrogen line broadening for both operating frequencies. The axial distance from nozzle outlet is denoted with $d$, the radius from the axis with $r$.

### 4.3.2 Temperature determination from molecular spectra

The molecular transitions of excited and ionized nitrogen were recorded and pre-processed according to the description given in section 3.4.3. Thereafter, the locally resolved spectra are imported and evaluated in the commercially available software taking into account the instrumental profile of the experimental setup shown in Fig. 3.9. During the evaluation it is assumed that the rotational and vibrational temperatures are equal, i.e. $T_{rot} = T_{vib}$. While recording of the spectra, the ICCD is triggered on both the peak current and the valley current between two consecutive pulses (see sect. 4.1) using the circuit described in section 3.4.1. Thereby each datapoint is measured three times and a mean value is calculated subsequently. By doing so an attempt was made to assess the temporal evolution of the temperatures. During the valley current phase however, the emitted light intensity is so low that temporal resolution cannot be obtained due to the required extension of the exposure time to achieve evaluable images. Therefore, only the spectra emitted during the current maximum are evaluated in the following. Based on the analysis of the voltage and current traces presented in section 4.1, the spectra are recorded for two frequencies, 43 kHz and 60 kHz, at a power setting of 100 %.
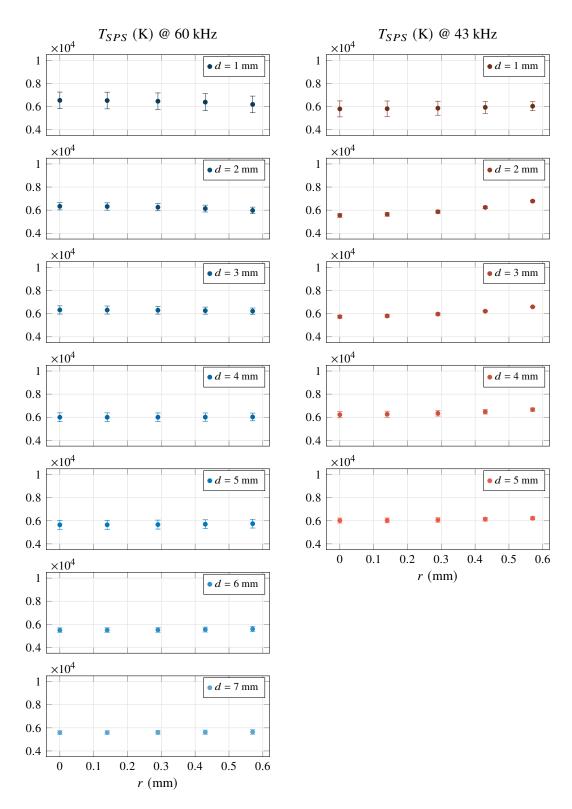
Figure 4.10: Spatial distribution of the temperature $T_{SPS}$ estimated for the SPS $(0,0)$-transition under the assumption $T_{rot} = T_{vib}$, when operating at two different frequencies. The axial distance from nozzle outlet is denoted with $d$, the radius from the axis with $r$.
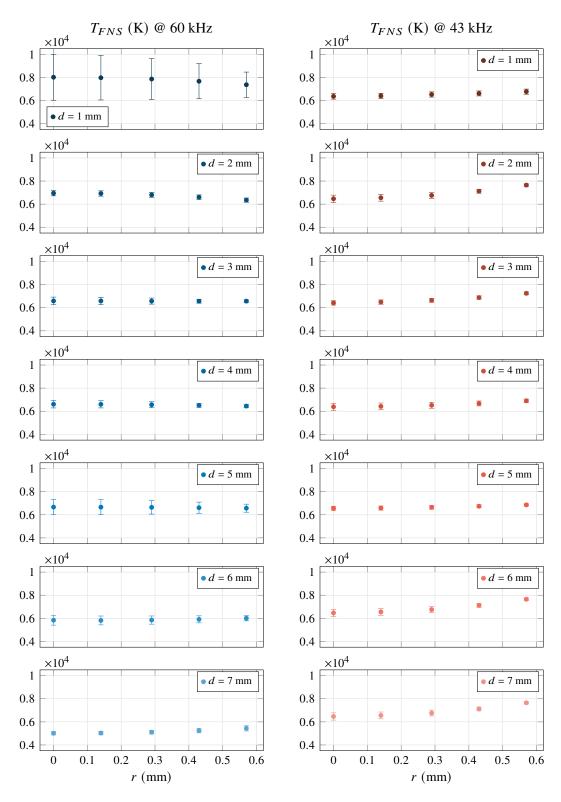
Figure 4.11: Spatial distribution of the temperature $T_{FNS}$ estimated for the FNS $(0,0)$-transition under the assumption $T_{rot} = T_{vib}$, when operating at two different frequencies. The axial distance from nozzle outlet is denoted with $d$, the radius from the axis with $r$.
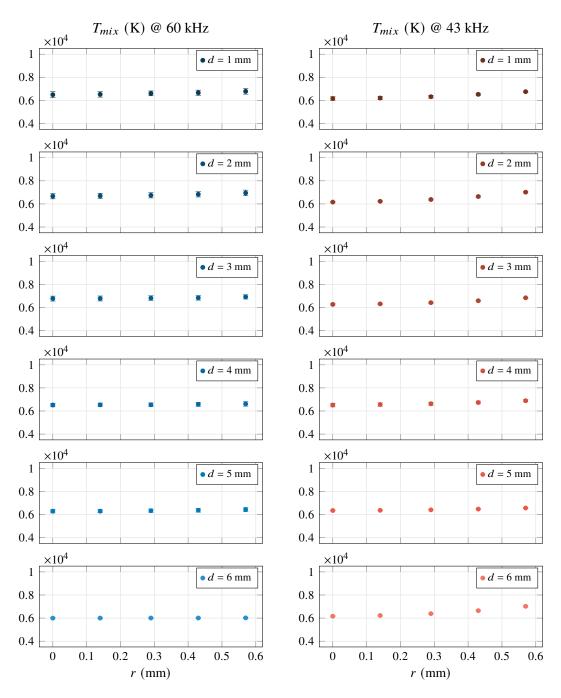
Figure 4.12: Spatial distribution of the temperature estimated for the $(1, 0)$- & $(2, 1)$-transition of SPS and $(0, 1)$- & $(1, 2)$-transition of FNS, denoted as $T_{mix}$, under the assumption $T_{rot} = T_{vib}$, when operating at two different frequencies. The axial distance from nozzle outlet is denoted with $d$, the radius from the axis with $r$.

The spatial distributions of the temperatures estimated for the SPS $(0, 0)$-transition, denoted as $T_{SPS}$, the FNS $(0, 0)$-transition, denoted as $T_{FNS}$, and for the wavelength range around 357 nm where the SPS $(1, 0)$- and $(2, 1)$-transitions mix with the $(0, 1)$- and $(1, 2)$-transitions of FNS, denoted as $T_{mix}$, are presented in Fig. 4.10, Fig. 4.11 and Fig. 4.12 respectively. Similarly to the previous section, the axial distance from nozzle exit is denoted with $d$ and the radius from its axis with $r$. In general, the temperature of the excited nitrogen molecule when operating at 60 kHz, presented on the left-hand side of Fig. 4.10, diminishes from 6500 K to 5500 K across an axial distance of 7 mm downstream from nozzle outlet. The temperature along the nozzle axis, i.e. for $r = 0$, can be assumed constant up to 3 mm and then gradually decreases with an approximate gradient of $-250$ K/mm. Looking at the radial distribution of $T_{SPS}$, a slight temperature drop of about 500 K is measured towards larger radial positions, although only up to about 3 mm. Further downstream, the estimated temperatures are constant or even marginally increase with increasing radius $r$. A similar behaviour of the estimated temperature values is observed for the $(0, 0)$-transition of ionized nitrogen molecule if the discharge is pulsed with 60 kHz, although the temperature difference is more significant within the analyzed distance range of 7 mm in comparison to the excited molecule. The $T_{FNS}$ values in the left-hand side of Fig. 4.11 decrease from almost 8000 K to 4600 K on nozzle axis, although a rather high deviation from the mean values is observed at a distance of 1 mm. This uncertainty is probably caused by imaging errors and hance should be considered as an outlier. At $d = 2$ mm the temperature falls radially from 7000 K on nozzle axis to about 6300 K at $r = 0.6$ mm, almost twice the value compared to a temperature difference of only 350 K in case of SPS spectra. A zone of almost constant temperature of approx. 6600 K spreads between 3 mm to 5 mm from nozzle exit. Further downstream, $T_{FNS}$ increases by about 8 % with increasing radial separation from the jet axis, which is also more significant than was the case for the SPS $(0, 0)$-transition.

When the discharge is pulsed with 43 kHz, the estimated temperatures for the excited nitrogen molecule $T_{SPS}$ are about 500 K lower for $r$ smaller than 0.3 mm and axial distances $d$ shorter than 3 mm when compared to the higher pulse frequency. Additionally, a steeper increase towards larger radial distances is observed, as depicted on the right-hand side of Fig. 4.10. Highest temperature values of approx. 6400 K are determined for a distance of 4 mm from nozzle exit. The irradiance of the SPS $(0, 0)$-transition proves to be lower than for other analyzed transitions, so spectra are collected only up to a distance of 5 mm to maintain temporal resolution and hence comparability with other measurements. The estimates for the FNS $(0, 0)$-transition are about 500 K higher compared to SPS, while working at the lower pulse frequency. When compared to the results observed for 60 kHz (see Fig. 4.11), the $T_{FNS}$ changes in the vicinity of nozzle axis are insignificant throughout the analyzed distance range up to $d = 5$ mm with an average of about 6600 K. Moreover, as already observed for $T_{SPS}$, the FNS results show a more pronounced temperature increase towards the outside at a frequency of 43 kHz than is the case at 60 kHz. This effect reoccurs in the spatial distribution of $T_{mix}$, as depicted in Fig. 4.12, estimated for the wavelength range where both transitions overlap. Only the core temperatures, i.e. for $d < 3$ mm and $r < 0.3$ mm, are slightly lower at 43 kHz, while others are similar and can be hence assumed to be independent of pulse frequency. The reduction might be caused by the less pronounced SPS radiation as previously stated. Interestingly, the $T_{mix}$ estimates at a distance of 6 mm are significantly lower than for 60 kHz.

Generally it can be noted that the trends and temperature values depicted in Fig. 4.10 and Fig. 4.11 for the $(0, 0)$-transitions of both systems correlate well with the results estimated from the wavelength range around 357 nm shown in Fig. 4.12. Thereafter, since both systems overlap in that wavelength range, the $T_{mix}$ values are used to estimate a relative particle density ratio between the SPS and FNS transitions. The particle density ratio presented in Fig. 4.13 when operating at the higher frequency of 60 kHz varies insignificantly around 0.74 in the immediate vicinity of the nozzle exit, i.e. for $d < 2$ mm and $r < 0.3$ mm. A second area where the ratio remains almost constant at 0.76, can be defined for distances $d < 4$ mm and radial distances $r < 0.45$ mm. Similarly to the temperature estimates, an

increase toward higher radii and a decrease in values for axial distances greater than 4 mm downstream from nozzle outlet is observed at this frequency. Comparing the particle density ratios between the two frequencies, it can be noted that the values are almost identical near the nozzle outlet and decrease by about 0.3 at an axial distance of 5 mm. As can be observed in Fig. 4.13, the increase of particle densities in the radial direction is almost non-existent for the lower frequency.
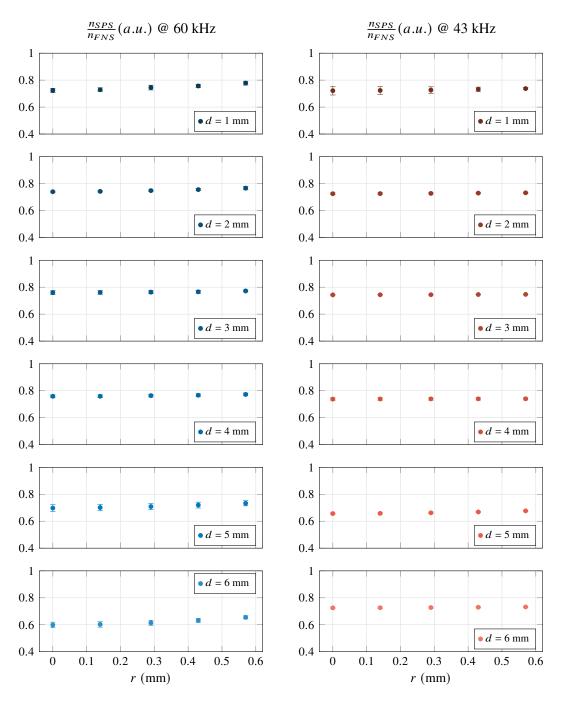


Figure 4.13: Spatial distribution of the relative ratio of $n_{SPS}$ to $n_{FNS}$ for both operating frequencies.

In summary, considering the measurement errors and inaccuracies in temperature estimation, it can generally be assumed that the rotational and vibrational temperatures within the discharge channel range between 6000 K and 7000 K for the analysed transitions and are nearly independent of the pulse frequency. Additionally, roughly about 25 % of the discharge channel consists of ionized

nitrogen molecules up to about 4 mm according to the results presented in Fig. 4.13.

## 4.4 Dynamics of the discharge channel

Several optical setups build around a high-speed camera are used to assess the dynamics of the discharge channel. The main focus is thereby put on three different aspects. Firstly, since low-current discharges are assumed to be driven by bouyancy of the carrier gas, the gas flow is visualized by Schlieren imaging in section 4.4.1. Thereafter, the temporal behaviour of the cathodic attachment point of the discharge is evaluated in section 4.4.2, as it seems to be crucial for the service lifetime of electrodes according to literature. Finally, the shape and movement of the blown-out channel is observed in section 4.4.3.

### 4.4.1 Schlieren imaging

Schlieren imaging allows for the visualization of gas flows due to density gradients as described in section 3.5.1. When coupled with a high-speed camera, thanks to the high frame rate and short exposure time, possible instabilities in the gas flow can be revealed. Nonetheless, a quantitative analysis of Schlieren images is difficult, especially for highly turbulent flows. The turbulence of a gas flow can be assessed by the dimensionless Reynolds number, denoted as $Re$. Assuming that the flow at the outlet of the nozzle resembles a gas flow through a pipe with an analogous diameter $d_\phi$ of 4 mm and that the gas is also at room temperature, the Reynolds number can be easily estimated using the following formula [48]

$$Re = \frac{\rho_{N_2} Q d_\phi}{\nu_{N_2} A} = \frac{1.165 \cdot 5.83 \times 10^{-4} \cdot 4 \times 10^{-3}}{1.757 \times 10^{-5} \cdot 1.26 \times 10^{-5}} \cong 12000$$

with $\rho_{N_2}$ and $\nu_{N_2}$ being the density and dynamic viscosity of nitrogen at room temperature. The cross section of the nozzle exit is denoted as $A$ and the volumetric gas flow as $Q$. A flow in a pipe is assumed to be fully turbulent for Reynolds numbers above 3000 [48]. Accordingly, the cold gas flow exiting the plasma generator can be already considered to be highly turbulent. Even higher $Re$ numbers are expected once the plasma is ignited, since the characteristic properties of the carrier gas, such as density or dynamic viscosity, are temperature-dependent. Hence, as already stated in section 3.5.1, only a qualitative analysis of the recorded images is attempted within this work.

The most significant effects occuring in the analyzed plasma system can already be observed in Schlieren images taken during an ignition phase of the discharge. An image sequence of the ignition phase for the generator pulsed at 40 kHz with a gas flow set to 35 l/min is shown in Fig. 4.14. The images are recorded at a rate of 40000 frames per second, with each image being exposed for 2 µs. For reasons of clarity, however, a longer time interval of 500 µs between the respective images is chosen for Fig. 4.14. As described in section 3.1.2, a much higher ignition voltage is needed to initially bridge the gap between electrodes. When such a high amount of energy stored in the high voltage capacitors is abruptly discharged, a significant pressure wave is emitted which can be seen in image 01. At a flow of 35 l/min, the volume of the discharge chamber is filled with fresh gas within approx. 1 ms. Thereafter, it takes about two consecutive images in Fig. 4.14 for the heated gas to reach the nozzle exit, resulting in an increase in the observed Schlieren intensity (image 04). With increasing temperature and prolongation of the discharge channel, the Schlieren get more and more pronounced. The swirl of the injected gas flow is noticeable between images 05 and 12, but the continuously increasing turbulence makes it less apparent from then on. Although the discharge is assumed to be driven by buoyancy [128], the lengthening of the conducting channel seems to be only loosely related to the gas flow velocity. The channel is blown out of the nozzle after approx. 8 ms (image 17 in Fig. 4.14), much later than the volumetric flow of the gas would suggest. The time at which the channel exits the nozzle varies between 8 ms and 14 ms, depending on the pulse frequency, and can be determined even
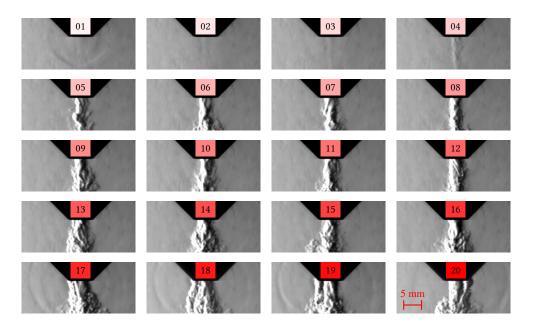
Figure 4.14: Schlieren images of the ignition phase of a discharge operated at 40 kHz with a gas flow of 35 l/min. The time difference between consecutive pictures is 500 µs, whereby the exposure time of each is set to 2 µs.

without a synchronous measurement of the electrical values. The attachment point outside the nozzle causes an additional, clearly visible turbulence, which rotates on the nozzle lip as depicted in images 18 to 20. Its rotation direction is assumed to be correlated with the swirl of the plasma carrier gas. Unfortunately it is not possible to estimate the rotation speed with sufficient accuracy, eventhough the images are recorded at a high frame rate, as the camera is not triggered synchronously with the process and the Schlieren setup provides only a two-dimensional information.
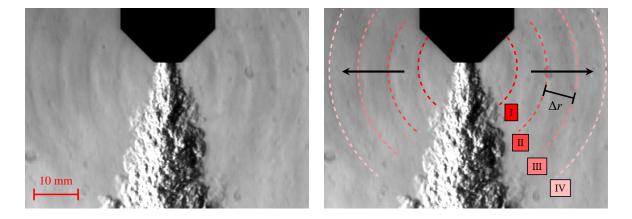


Figure 4.15: Due to pulsed operation, pressure waves are emitted by the discharge channel. The process is operated at 50 kHz with a gas flow of 35 l/min. An original Schlieren image is shown on the left-hand side, on the right-hand side the distinguishable pressure waves I-IV are marked with dashed lines. Arrows mark the propagation direction and the distance between two consecutive pressure waves $\Delta r$.

Furthermore, another effect is observed after the discharge stretches out of the nozzle. Beginning from image 17 in Fig. 4.14 pressure waves similar to the one emitted after the initial breakdown are observed. When the process operates at a similar frequency to the frame rate of the camera, a quasi-standing wave is found around the nozzle exit, indicating the discharge pulses as the cause. If a larger

area around the nozzle outlet is observed, it can be noted that the emitted pressure waves propagate in space as shown in Fig. 4.15. The presented image is taken at a rate of 10000 frames per second while the generator is working at 50 kHz. Four consecutive pressure waves I-IV can be distinguished in the image and are marked on the right-hand side of Fig. 4.15 for better visibility. If the discharge pulses are responsible for the emission of these waves, the distance $\Delta r$ between the concentric marks in the right-side image should correlate with the operating frequency. In Fig. 4.15, the $\Delta r$ is approx. 6.9 mm, which divided by the speed of sound, assumed to be 343 m/s at atmospheric pressure and room temperature, results in a time interval of approx. 20 µs between successive pressure waves. The calculated time interval thus correlates exactly with the pulse frequency at which the discharge is operated. Thereafter, although the waves are not observed as long as the discharge channel is not blown out of nozzle (see Fig. 4.14), their emission is inevitable due to the pulsed mode of operation. Furthermore, the pressure waves are permanently reflected by the inner walls of the generator and influence the channel's stability.

### 4.4.2 The cathodic attachment point

To assess the cathodic attachment point of the discharge, the camera's angle of view is directed straight onto the nozzle outlet as described in section 3.5.2. The images are captured at a rate of 18000 frames per second and an exposure time of 2 µs, while the process is operated at 60 kHz with a nitrogen flow of 35 l/min. To capture both, the bright intensity of the discharge at peak current and the glow between pulses, the full 12 bit dynamic range of the camera is used. Hence, the dynamic range of the images presented in Fig 4.16 is adjusted so that the cathodic attachment point is clearly visible at each point of time.
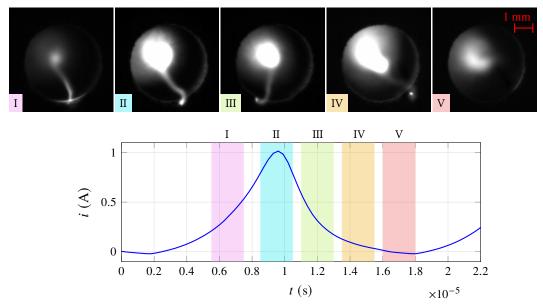


Figure 4.16: Typical cathodic attachment points observed for different points in time of the current waveform. The discharge is driven with 60 kHz and nitrogen flowing at 35 l/min. Although the exposure time was fixed at 2 µs, the brightness is adjusted for each image separately to emphasize the differences.

As depicted in Fig 4.16, the cathodic attachment point of the discharge changes with the current waveform. For a rising current (image I), the attachment point is diffuse and spans over about 1.5 mm across the nozzle lip. With further increasing current (image II), the discharge channel increases in diameter but the attachment contracts to a bright spot to sustain the required electron emission. The local spot heats the surface of the cathode intensively so that the attachment point remains constricted

during the falling edge of the current trace (images III and IV). Only when the current falls to minimum (image V), the spot fades away and a new diffuse attachment is created when the current starts to rise again. According to Jeanvoine, the transition from a diffuse to a constricted attachment mode is coupled with an increase in cathode current density by many orders of magnitude. Due to the localized heating or even evaporating of the electrode material, the author showed that additional erosion mechanism come into play, what results in a higher electrode erosion rate than in case of a diffuse discharge attachment [77].

### 4.4.3 Spatial dynamics

For a better evaluation of the shape and movement of the discharge channel, the HOBAS-3D system is used. The high frame rate achievable with this system allows to observe the progression of the channel within a pulse period. By simultaneous acquisition of the HOBAS sequences with the electrical waveforms, an attempt is made to find possible indicators of channel movement in the traces.

A HOBAS-3D image sequence is shown on the left-hand side of Fig. 4.17. It contains 10 projections of the observed object from three different viewing angles, which are subsequently used for a tomographic reconstruction as described in section 3.5.3. The sequence was recorded with the mirror rotated at a speed of 12000 revolutions per minute, the gating delay between consecutive images set to 2 µs and the exposure time of the intensifier to 150 ns. On the right-hand side of Fig. 4.17, the corresponding voltage and current traces are plotted. Additionally, the trigger time points $t_{1..10}$ are marked in both.
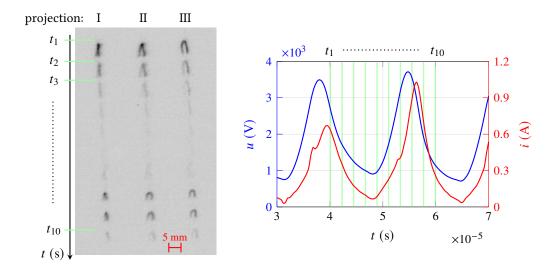


Figure 4.17: A HOBAS-3D image sequence containing 10 projections of the discharge channel with the corresponding electrical traces. The trigger time points are marked as $t_{1..10}$. For selected time points, the projections I-III are reconstructed to a three-dimensional image.

The image sequence in Fig. 4.17 confirms the effects observed with other diagnostic methods. The energy supplied to the system with each pulse is sufficient to reignite the discharge channel. Accordingly, the emitted radiation intensity correlates clearly with the current waveform, the highest intensity is observed at the current maximum. Furthermore, altough significantly weaker, emission is also registered during the current minimum between successive pulses. The channel retains roughly its length from pulse to pulse. No jumps or shortening of the discharge is observed, as was reported for pulsed thermal discharges [7, 44, 153, 189]. Interestingly, the amplitudes of the electrical waveforms do not seem to correlate with the length or shape of the channel. Also, the intensity emitted at $t_8$ and

$t_9$ seems to be weaker than the radiation at $t_1$. This effect, however, may be caused by spatial gain inhomogenities of the image intensifier or by imaging aberrations due to the rotating mirror.
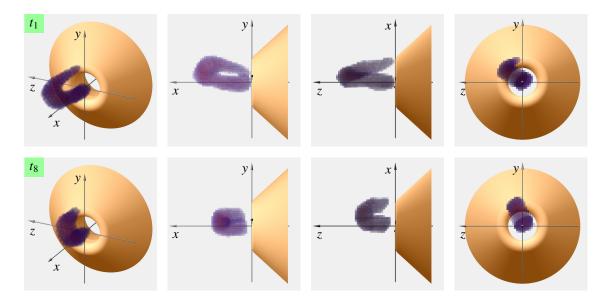


Figure 4.18: Tomographic reconstructions of the discharge channel at trigger time points $t_1$ and $t_8$ according to the measurement displayed in Fig. 4.17.

To further assess the movement of the discharge channel, tomographic reconstruction at time points $t_1$ and $t_8$ are presented in Fig. 4.18. At the point $t_1$ the discharge is blown-out further downstream, resulting in a much more twisted shape. At the next pulse, i.e. at time point $t_8$, the channel is shorter and rotated slightly clockwise, as can be seen in image of the $yz$-plane. The gap between the reconstruction and the nozzle model observed in the $xy$- and $xz$-planes at this point of time results from the selected display settings. For comparability reasons, the settings were kept constant for both time points. As indicated by Schlieren imaging, the rotation is attributed to the swirled flow of the plasma gas. Even if the rotation seems to be relatively slow according to Fig. 4.18, a quantitative evaluation of its speed cannot be made on the basis of only a few images. Thereafter, since the creation of the tomographic reconstructions is a time-consuming process, an attempt is made to estimate the movement speed based on the change in length of the blown-out channel.

Thus, further HOBAS sequences are recorded. Thereby, the number of acquired images was increased to 20, which allows the observation of almost three periods when the generator is operated at a frequency of 60 kHz. As can be observed in Fig. 4.19, the discharge lengthens or shortens only slightly from pulse to pulse with the movement direction being stochastically indepentent. The movement of the channel thus appears to be only loosely related to the gas flow velocity. Again, similar behavior was observed in the Schlieren recordings. The HOBAS sequences show additionally, that the turning point of the discharge is located on average at a distance of about 5 mm from nozzle exit. The discharge channel behaves as described above also when working with the lower frequency of 43 kHz, although the blown-out channel stretches only occasionally over 5 mm in contrast to the higher pulse repetition rate. Usually, the turning point is located between 2 mm and 3 mm from the nozzle, as can be seen in Fig. 4.20.
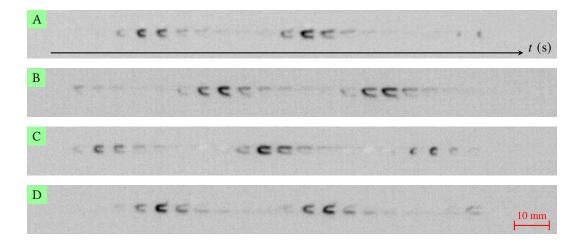
Figure 4.19: Typical HOBAS sequences of the discharge channel pulsed at 60 kHz. The mirror is rotating with 12000 revolutions per minute, the time delay between each image is set to 2 µs and the exposure time of the image intensifier to 150 ns. The different points of time A-D are chosen arbitrarily.
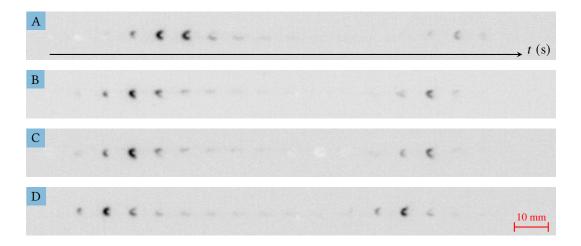


Figure 4.20: Typical HOBAS sequences of the discharge channel pulsed at 43 kHz. The mirror is rotating with 15000 revolutions per minute, the time delay between each image is set to 2 µs and the exposure time of the image intensifier to 150 ns. The different points of time A-D are chosen arbitrarily.

# 5

## DISCUSSION

Based on the above results, the following working hypothesis can be formulated. The operating principle of the system, as described in section 3.1.2, is quite simple. The power supply delivers constant current pulses that charge a capacitance, the size of which is defined by the length of the triaxial high voltage cable. While charging, the voltage across the electrodes increases until the electric field strength reaches the breakdown voltage. Then, since the system is usually operated with molecular gases (compressed air or nitrogen) at atmospheric pressure, a streamer is formed which transforms into a spark within nanoseconds after reaching the cathode [15, 152]. The accumulated energy is then discharged through the conductive channel. Thus, the discharge in itself is a self-pulsating system - a discharge will occur whenever the breakdown voltage across the conductive channel is reached. However, a pulsed power delivery lowers the energy consumption of a system [98] and provides control over the power deposited in the plasma by altering the pulse amplitude or repetition rate [68], allowing the timing of the discharge to be controlled as a result. A pulsed operation also implies higher electron temperatures to sustain a similar electron density, since the energy transfer between electrons and heavy particles is several orders of magnitude smaller than between electrons themselves according to the example given in [98], which is why pulsed operation is often used to minimize the heating of neutrals at atmospheric pressures [15, 113]. Thereafter, according to Lu [113], the electron temperature, which is mainly determined by the reduced electric field, i.e. the electric field divided by the neutral gas density, as well as gas temperature, which is defined by dissipated power, can be in theory controlled independently by adjustment of the pulse amplitude, its width and frequency. As a conclusion, pulsed operation implies that the plasma is in non-equilibrium.

Molecular gases, especially nitrogen, are capable to accumulate energy in vibrational, metastable or dissociated states over longer periods of time [4, 5]. Reactions such as ionic recombination, metastable induced dissociation or neutral interactions and diffusion processes occur on timescales of hundreds of microseconds or even milliseconds [10, 15, 91], hence for sufficiently high pulse repetition rates the temperature and concentration of excited species within the discharge channel cannot be cleared fast enough by the gas flow [67], what inhibits the streamer formation [15] and leads to a significant reduction of the initial breakdown voltage in comparison to the operating breakdown voltage as a result [4]. As described by Cobine [26] and more recently by Risacher *et al.* [152], the reaction of the plasma forming gas on the pulse frequency is reflected in the current-voltage characteristic. Consequently, once ignited, a glow discharge is created between the electrodes that does not fully extinguish between consecutive pulses. In contrast to sparks or arcs, a glow discharge is characterized by the predominant presence of molecular bands in the spectrum rather than atomic lines [67]. With each current pulse, the energy is used for excitation of nitrogen molecules at first, while the neutral particles are heated mainly as a result of the vibrational-translational relaxation processes [91]. The channel transitions from a glow discharge to a spark as the current density rises (see sect. 4.4.3), creating thereby spots on the cathode (see sect. 4.4.2) while the electron emission mechanism changes

to thermo-field emission [67, 148]. The creation of a contracted cathodic attachment point influences the lifetime of the consumables [55, 77, 147]. Although for non-refractory cathode materials a sudden transition into an arc can occur already at currents in the range of 1 A or lower as reported by some [68, 148], it does not seem to be the case here since such a transition is usually characterized by a large voltage drop coupled with a high-amplitude, short-duration current spike as observed by Hsu and Wu [68]. For such a transition to occur, an efficient energy transfer between free electrons and heavy species is needed, what is usually the case when $T_e \sim T_h$. Due to the short duration of the pulses, this is not the case here, as the results in chapter 4 also show. Thereafter, the discharge is probably best described as transient spark as suggested by Bruggeman *et al.* [15]. Nonetheless, due to the complex and above all transient nature of the plasma studied in this work, it seems difficult and to some extent rather irrelevant to find a term that would accurately describe or assign it to a common type of discharges usually described in the literature.

A pulsed energy delivery implicates pulsed heating of particles in the discharge channel, what leads to pressure changes and creation of shock-waves [15, 184]. Similar pressure waves to those observed by Xu *et al.* [184] were visualized by Schlieren images here (see sect. 4.4.1). The emitted waves are inevitably reflected by the inner walls of the plasma generator creating acoustic resonances and, even though the connection between gas buoyancy and channel movement is found to be far less stringent than might be expected (see sect. 4.4.3), lead to instabilities as described by Ashfar [1, 2]. It should be noted, that the instabilities change with varying temperature of the entire generator body what sort of limits the choice of operating point of the system until steady-state is reached. The emission of shock-waves can however be used as a process monitoring diagnostics as proposed by Law *et al.* [104]. Furthermore, the current pulsed at frequencies studied does not cause a controlled relocation, i.e. shortening of the discharge channel as previously reported for thermal arcs [7, 44, 153, 189], due to the relative long lifetime of different molecular states. Consequently, to prevent the discharge from exiting the generator as shown in Fig. 3.3 for the A450 nozzle - an effect also described by Fulcheri *et al.* for low-current high-voltage DC discharges in [51] - when for example new application fields are targeted, these effects should be taken into account in the development process. According to the above discussion, the stability of such a discharge is an interplay between the type of gas used, the pulse frequency, the gas flow rate and the geometry in which the discharge takes place. Although often overlooked, the exact specification of parameters for which a measurement was carried out seems crucial when such complex transient discharges are analyzed experimentally.

If the results are considered with regard to the diagnostics used, it can be noted that it is possible to determine the electron parameters with a relatively simple and compact laser scattering setup. Experimentally measured values of $n_e$ and $T_e$ of a transient spark discharge could not be found in the literature until now. Hence, with their knowledge the relevant excitation and de-excitation processes can be re-evaluated. Furthermore, the heavy particle temperatures determined by the means of laser scattering and spectroscopically agree well with each other (see sect. 5.2.1) and with literature values (see sect. 5.2.2). Other diagnostics used allow to observe effects, as already indicated above, to some extent similar to ones reported by other researchers for glow and spark discharges at atmospheric pressure. A detailed discussion of the results that supports the above working hypothesis can be found in the following sections.

## 5.1 Electrical behavior

The transient nature of the analyzed discharge can be visualized by comparing the results of the electrical measurements with the voltage-current characteristic of a DC discharge depicted in Fig. 5.1. Although the characteristic is recorded for a low pressure discharge, the gas pressure is not a definitive determinant of the occurring transitions [149], and so abnormal glow discharges as well as non-thermal and thermal arcs can be operated at atmospheric pressure. Therefore, it is referred to by the authors as

an universal voltage-current characteristic [149].
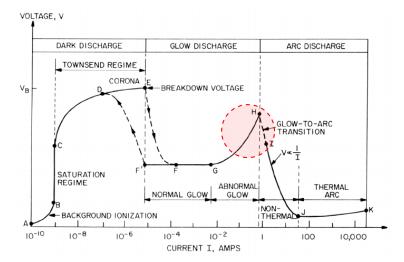


Figure 5.1: An universal voltage-current characteristic of a DC discharge taken from [149]. The operating range of the plasma system is marked by a dashed circle.

The output current of the power supply transitions in steady-state operation between 50 mA and 1 A according to the measurements from section 4.1. In this current range, marked by a dashed circle in Fig. 5.1, a discharge transitions from abnormal glow to a non-thermal arc discharge according to the graphic. The current and voltage values of about 50 mA and 500 V measured between consecutive pulses, denoted as $I_{valley}$ and accordingly $U_{valley}$ in Fig. 4.2, are in a similar range to those measured by Hontañón *et al.* [67] for a nitrogen glow discharge between pin-pin copper electrodes. Furthermore, when looking at the high speed images presented in section 4.4, a glow discharge existing between consecutive pulses can be observed. Thus, it can be concluded that a glow discharge exists between consecutive pulses.

The rising current density of the glow discharge heats up the cathode surface leading to creation of cathode spots, what initiates the glow-to-arc transition [148, 149]. Images of the high speed camera coupled with measurement of the electrical signals show such a behavior, as presented in section 4.4.2. The cathode spot typically appears to be diffuse for a rising current edge and is constricted to a spot when the current peak is passed. However, probably due to an insufficient charge contained in each pulse, the discharge does not fully transition to an arc as no sudden voltage drop coupled with a short-duration current spike, similar to those reported by Hsu and Wu [68], is observed in the temporal progression of the electrical traces. According to the authors, the transition of the discharge occurs when a specific amount of energy, defined as the integral of the product of voltage and current during the rising edge, is deposited in the existing conducting plasma channel. Furthermore, Hsu and Wu state that the energy needed for a transition to occur decreases with increasing pulse frequency or increasing amplitude. Although the energy presented in Fig. 4.2 is calculated by integration of the whole pulse period, similar decrease is observed. By multiplying the energy per pulse with the operating frequency an average power can be calculated as suggested in [95]. Thus, the energy per pulse values measured at the exit of the power supply are multiplied by the frequency and presented in Fig. 5.2. As can be seen, the output power of the power supply increases slightly for higher repetition rates, causing a reduction in the transition voltage - here denoted with $U_{peak}$ - as stated in [68]. Similar behavior is reported for self-pulsed discharges in [67] or nanosecond repetitively pulsed ones in [140]. Moreover, consistently with the results of Hsu and Wu, a reduction of frequency increases the value of $I_{peak}$. As reported by the authors, even though the glow-to-arc transition process itself is controlled by the plasma physics rather than by the power supply, the amount of energy is crucial to generate a stable

plasma. Hence, it is concluded that a discharge may not fully transition into an arc if the energy amount in not sufficient, what seems to be the case here.
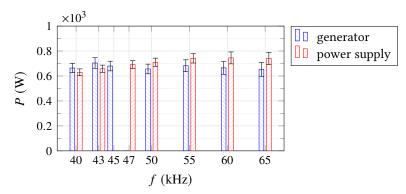


Figure 5.2: Average power calculated from the energy per pulse for different frequencies at a power setting of 100 %.

The glow-to-arc transition is characterized by a negative current-voltage slope (point H to I in Fig. 5.1). If a discharge is to be operated stably in this range with direct current, the current-voltage characteristic of the power supply must be steeper than that of the discharge so that the discharge can be maintained after ignition [149]. To achieve this, a balast resistor or a resonant LC circuit is usually used [51]. Nonetheless, as described by Cobine [26], the current-voltage characteristic of an arc is dynamic and changes with frequency. Depending on the heat conductivity of the electrodes and the plasma forming gas, i.e. on the temporal progression of electron and ion temperatures and concentrations to be precise, the initial linear progression of the negative slope is deformed to an elliptic shape as the ionization rate lags behind the current change. Thus, for arcs pulsed at high frequencies, the $i$-$u$ characteristic can have a positive slope, i.e. the voltage increases almost linearly with the current, which ensures stable operation of the discharge. As reported by Risacher *et al.*, who
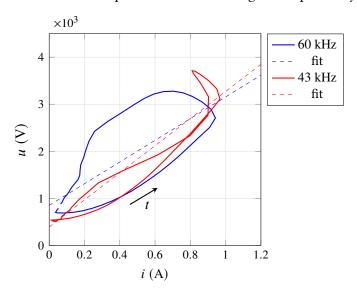


Figure 5.3: Voltage-current characteristic of an average pulse measured at the exit of the power supply with the time increase direction indicated by an arrow. The corresponding temporal progression of the pulses is shown in Fig. 4.1.

investigated the stability of low-current arcs in atmospheric air [152], if the discharge channel is long enough to minimize the influence of the electrode fall regions on the voltage across the electrodes, the shape of the current-voltage characteristic can indicate the state and stability of the plasma.

Consequently, such characteristics are plotted for both operating frequencies studied here. As depicted in Fig. 5.3, despite the traces having a more or less elliptic shape, positive slopes can be determined by linear fitting in both cases. According to the above discussion, Fig. 5.3 indicates that the operating frequency of the power supply is high enough so that the processes occurring in the plasma do not follow at the same rate.

Apart from the frequency, the width and amplitude of a pulse can be used to adjust the plasma parameters as stated in [113]. Since the pulse width is fixed at 10 µs, the trajectories of voltage and current were analyzed to determine the slew rate, i.e. maximal slope, for both edges of each pulse. The mean voltage slew rate (short USR) and mean current slew rate (ISR) for the rising and falling edges are presented in Fig. 5.4. The significantly higher ISRs observed for an operating frequency of 43 kHz may indicate that higher electron densities are to be expected. Furthermore, since the electron-controlled reactions depend on the reduced electric field, i.e. the electric field divided by the neutral gas density, USR changes may correlate with a change of electron parameters (i.e. $n_e$ and $T_e$). The time delay observed in Fig. 4.1 between voltage $u$ and current $i_{gen}$ measured near the
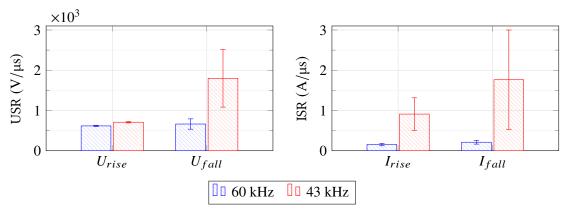


Figure 5.4: Mean voltage slew rate (USR) and current slew rate (ISR) for rising and falling edges measured for both frequencies measured prior to the plasma generator when operating with a power setting of 100 %.

plasma generator can be attributed to secondary electron emission according to [67, 106]. Although working with DC glow discharges, Hontañón *et al.* [67] and Akishev *et al.* [4] also reported sinusoidal oscillations with frequencies up to 55 kHz of unknown origin in the measured voltage and current traces. Oscillations in a similar frequency range as the operating pulse rate of the analyzed plasma system could influence the discharge stability, but are not observed in the measured electrical traces.

As shown in Fig. 5.2, the energy per pulse multiplied by the operating frequency allows the estimation of the consumed power. Korzec and Nettesheim measured current and voltage for a frequency of 50 kHz while operating a PG31 generator with dry compressed air and calculated an energy per pulse of 3 mJ similarly to the values estimated in section 4.1, as an integral over the period of the instantaneous power [95]. Comparing the result presented in [95] with Fig. 4.2, a resulting energy per pulse more than five times higher is obtained at 50 kHz when using nitrogen within this work. Based on the laser scattering results presented in section 4.2.1 and 4.2.3, the energy per pulse is directly coupled with the temperature of heavy particles (see sect. 5.3.1). Thus, if such a high discrepancy would be caused only by a different plasma carrier gas, then the temperatures should be also significantly different. However, this is not the case according to the gas temperatures published in the same paper [95] for both gases at a flow rate of 40 l/min. A detailed discussion of the gas temperature can be found in the sections 5.2 and 5.3. The steep current pulse slopes presented in Fig. 4 in [95] indicate that the measurement was performed by the authors at a higher gas flow rate than is the case here, although half as large amplitude of the voltage would suggest the contrary. Another

possible explanation for this discrepancy might be a different type of nozzle, although A450 is stated in the description, or a different measurement position of the electrical traces.

According to the manual of the PS2000 power supply [151], the maximal power consumption from the mains should not exceed 1200 V A. If maximal heat and switching losses of the power supply of 450 W are assumed [151], then the theoretical maximal output power amounts to 750 W. The calculated results presented in Fig. 5.2 do not exceed the supply's maximal output power value of 750 W, which on the one hand speaks for a good, energy-efficient design of the system and on the other hand is an indicator of the plausibility of the results. This value however cannot be considered to be the effective power transferred into the plasma, since several loss mechanisms exist. The power consumed by the plasma generator with the connection cable is roughly a sum of conduction and contact losses on the electrical connections $P_{cont}$, thermal losses due to Ohmic heating $P_{gen}$ as well as radiative losses $P_{rad}$ and finally the power which is coupled into the plasma $P_{plasma}$. Hence, the plasma power can be assumed to be lower than the measured power value $P_{avg}$ according to

$$P_{plasma} = P_{avg} - P_{cont} - P_{rad} - P_{gen}.$$

The manual of the PG31 defines a maximal temperature of the generator of 200 °C [150]. Consequently, the heat losses can be very roughly estimated as a sum of

$$P_{gen} = \left( Q_{nozzle} + Q_{body} \right) / t = \Delta T \left( m_{nozzle} c_{Cu} + m_{body} c_{316L} \right) / t \,.$$

Assuming a temperature difference $\Delta T$ of 180 K, a nozzle mass of 100 g, specific heat capacity of copper of 0.385 $\frac{\text{kJ}}{\text{kgK}}$ [118] as well as a mass of the generator's body of 400 g made of stainless steel with an assumed specific heat of 0.5 $\frac{\text{kJ}}{\text{kgK}}$ [117] and a time of 1 s, the heat losses are equal to

$$P_{gen} = 180 \left( 0.1 \cdot 0.385 + 0.4 \cdot 0.5 \right) / t_{period} \cong 42.9 \text{ W} \,.$$

Presuming other power losses are in a similar range, this might explain the the difference observed in Fig. 5.2 between the power measured at the power supply's exit and prior to the plasma generator.

## 5.2 Validity of results

The characteristic parameters of free electrons in pulsed low-current transient spark discharges have not been experimentally determined so far. Thus, the results obtained with the laser scattering setup are first compared with estimates based on emission spectroscopy measurements in section 5.2.1. Thereafter, the results are compared in section 5.2.2 with reference values determined experimentally or by calculations for similar discharges, i.e. glow discharges, nanosecond pulsed discharges or gliding arcs, all operated at atmospheric pressure.

### 5.2.1 Comparison of diagnostic methods

Several authors report a good agreement between experimental results of laser scattering and emission spectroscopy [32, 125, 142]. Nonetheless, discrepancies between both diagnostic methods are also reported [141]. To provide a better overview for the following discussion, the most important results presented in chapter 4 are summarized in table 5.1. According to this table 5.1, the results of laser scattering and emission spectroscopy are in good agreement. The values are of the same order of magnitude and show similar trends for both, electron number density and temperature of heavy particles. With both diagnostic methods, higher $\bar{n}_e$ and lower $\bar{T}_h$ values are obtained for the lower operating frequency of 43 kHz. The behaviour of the plasma at different operating frequencies will be discussed later in section 5.3. As can be also seen in table 5.1, the differences in the electron densities determined with the scattering experiment between the two frequencies studied are much more subtle

than is the case with the values estimated with spectroscopy. The spectroscopically determined number densities are only half or even only a third as large when absolute numbers are compared to each other at the same frequency.

Table 5.1: A summary of the results presented in chapter 4 obtained with both diagnostic methods when triggered at $I_{peak}$.

| Method | laser scattering | emission spectroscopy | laser scattering | emission spectroscopy |
|---|---|---|---|---|
| $f$ (kHz) | 60 | 60 | 43 | 43 |
| $\bar{n}_e$ (m$^{-3}$) | $1.7 \times 10^{21}$ | $0.5 \times 10^{21}$ ($H_\beta$ line) | $2.0 \times 10^{21}$ | $0.9 \times 10^{21}$ ($H_\beta$ line) |
| $\bar{T}_e$ (K) | 41000 | – | 49000 | – |
| $\bar{T}_h$ (K) | 5900 | 6600 | 5200 | 6100 |

This discrepancy between the absolute values of electron density might be related to the evaluation methodology of the Stark broadening as indicated in [141]. According to section 3.4.2, the shape of the hydrogen line is influenced by Doppler, van der Waals (vdW) and Stark broadening mechanisms as well as the instrumental profile of the used spectrograph. The applied evaluation methodology assumes that the contribution of Doppler and vdW components are insignificant compared to that corresponding to the Stark broadening and thus are neglected in the data evaluation. Both broadening mechanisms, Doppler and vdW, depend on the gas temperature according to the approximation formulas (2.63) and (2.64) given in [92, 141, 183]. Thereafter, the gas temperature must previously be estimated, either from scattering measurements [141] or from molecular spectra [183], to assess the actual influence on the width of the hydrogen line used for the estimation of the electron density. According to the results summarized in table 5.1, a heavy particle temperature in the range of 6000 K is expected. For a $T_h$ of 6000 K, the Doppler broadening is slightly more pronounced with a $\Delta\lambda_{Dopp} \cong 0.03$ nm than the vdW broadening with $\Delta\lambda_{vdW} \cong 0.01$ nm. Nevertheless, the width of the instrumental profile of the spectroscopic setup (depicted in Fig. 3.9) will increase only by less than 5 % when convoluted with such a $\Delta\lambda_{Dopp}$ (see Fig. 2.10). Thereafter, neglecting of both broadening mechanisms is unlikely to be the cause of the difference in the electron number densities.

According to the theory described in section 2.2.2, the Stark effect has been discussed for two limiting cases, the linear and the quadratic case. The approximation formulas given in [53], used by most authors [92, 141, 183] and also used here, are derived for the linear case, in which the line broadening is proportional to $\sim n_e^{2/3}$. Such linear method assumes a non-spherically symmetrical distribution of electrons within an atom, i.e. that the emitting atom already displays a dipole moment, and that the free electrons act collectively. In contrast, the quadratic Stark effect assumes a sequence of two consecutive interactions between the atom and the free plasma electrons. The first interaction "deforms" an initially spherical symmetric atom inducing a short-lived dipole moment, while the second interaction with another free electron is responsible for the eventual emission of radiation by the atom. As a consequence the line broadening is directly proportional (in a good first approximation) to $\sim n_e$. However, if the effects occurring in the analyzed plasma correspond to an intermediate situation between both limiting approximations, for example due to the complicated ionization process of nitrogen plasmas in non-equilibrium, then the estimation of $n_e$ is more complex and the values cannot be calculated directly with the approximation formula (2.75) corresponding to the linear case. This may be the reason for the difference between the $n_e$ values determined spectroscopically and by the scattering experiment. Nonetheless, it should be noted that the values summarized in table 5.1 are of the same order of magnitude and, more importantly, the same trends are observed, which seems to be a sufficient validation of the laser scattering results in combination with the molecular spectroscopy.

The spectroscopically determined values, i.e. $n_e$ and $T_h$, increase somewhat counter-intuitively for higher distances from jet axis (see Fig. 4.9-4.12). Such an increase of values was also observed in [70, 176] and might be caused by an effect described by Jonkers *et al.* [79]. The researchers used laser scattering to estimate electron parameters of a plasma torch with axial gas injection driven by microwaves and operated with argon as well as helium at atmospheric pressure. A significant increase in both electron density and temperature was observed with increasing lateral distance from torch axis. The effect was reduced by changing the ambient atmosphere from air to argon. Thus the authors concluded that it is attributed to air entrainment from the surroundings according to the following reasoning. The energy of ionized argon atoms is transferred to the surrounding nitrogen molecules [1], which most likely leads to the observed change through the subsequent ionization and de-excitation processes [79]. However, since the discharge in this work is operated with pure nitrogen and the increase is only observed in the spectroscopically determined values, the above hypothesis does not seem to prove the effects satisfactorily.
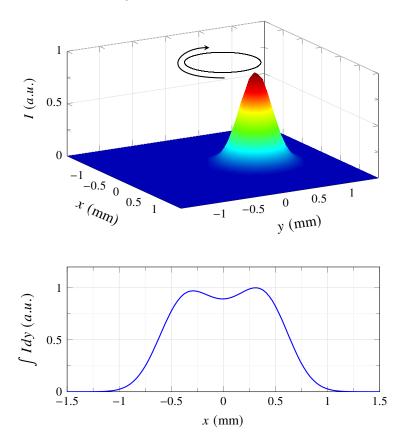


Figure 5.5: A two-dimentional Gaussian approximates the intensity emitted by the discharge channel. After integration on a detector, a bimodal intensity distribution can be observed when the movement of the channel is taken into account.

Another possible explanation for such an increase of values in the radial direction can be given if the beam geometry of the spectroscopic setup is considered in detail. A nearly Gaussian distribution can be assumed in a first approximation for the intensity radiated by the discharge plasma channel, which is then imaged by the spectrograph onto the sensor plane of the camera, where an integration of the signal in the viewing direction takes place. However, the integrated signal contains no information about the distribution of the emitted radiation in the direction of observation and thus an additional assumption is needed to describe the intensity distribution in the viewing direction. If again a nearly

---

[1]The energy transfer between argon and nitrogen is quiet complex and an ongoing research topic [43, 96]

Gaussian intensity distribution is assumed in the viewing direction, then as a result the emitted intensity can be approximated by a two-dimensional Gaussian as shown in Fig. 5.5. If the intensity peak is now positioned slightly off-center from the nozzle axis and moves e.g. rotationally, as marked in Fig. 5.5, then a bimodal distribution of the intensity is observed as a result of the integration on the camera sensor. Looking at such a bimodal distribution, it becomes apparent that the estimated values can increase towards further radial positions if the experimental setup is well aligned with the axis of the plasma generator. The above hypothesis is supported by the high speed images of the discharge channel, especially the HOBAS-3D image sequences presented in section 4.4.3. As can be seen in those images, the discharge channel twists differently with varying axial distance from nozzle exit, which inevitably will result in different images integrated by the camera sensor. Thus, according to this discussion, the lateral motion of the discharge channel is responsible for the increase in values for increasing radial distances.

Such an increase is not observed in the results of the laser scattering experiment, since the individual images are recorded with much shorter exposure times compared to spectroscopy and can thus be assumed as nearly instantaneous snapshots. Moreover, the images are sorted prior to evaluation as described in section 3.3.3, with the plasma zone region of interest constraining the position of the discharge channel. Hence this significantly reduces the influence of the channel's lateral motion in the scattering results.

According to the results presented in section 4.2, core heavy particle temperatures around 6000 K are reached on average and remain constant for several millimeters from nozzle outlet. Why the values initially remain constant becomes obvious when the geometry of the discharge channel is considered, as presented in the reconstructions in Fig. 4.18-4.20. In steady-state operation, the channel is blown out of the nozzle, twisted slightly by the cooling gas flow and at some point reverses to create a cathodic attachment point at the nozzle orifice. Thus the core values remain constant as long as the channel stretches out of the nozzle. Consequently, the turning point is probably located on average around 5 mm from nozzle outlet when the discharge is pulsed at 60 kHz, and accordingly at approx. 3 mm during operation at 43 kHz (see Fig. 4.4).
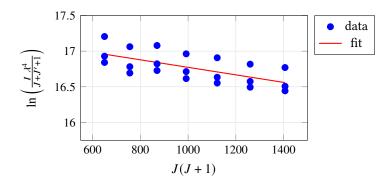


Figure 5.6: The measured rotational levels of the FNS $(0, 0)$-transition do not deviate significantly from a Boltzmann distribution defined by a single temperature. The linear fit is used to estimate the rotational temperature according to equation (2.83).

Finally, to validate the estimated heavy particle temperature values and, more importantly, verify if the rotational levels do not deviate from a Boltzmann distribution, the method described in section 2.2.6 is used. Thereafter, the amplitudes of the relevant rotational peaks of the FNS $(0, 0)$-transition (see Fig. 2.13) are compared in a Boltzmann plot with the quantum numbers of the involved electronic states. Such a plot is shown in Fig. 5.6 for a series of three spectra all measured at a distance of 1 mm while the discharge is pulsed at 60 kHz. As can be seen, the rotational levels show nearly no deviation from a single Boltzmann distribution (single slope in Fig. 5.6). Furthermore, a mean rotational temperature of 5700 K with a deviation of ±300 K is obtained from the linear fit according to equation (2.83), which

is in good agreement with the $T_h$ values summarized in table 5.1.

### 5.2.2 COMPARISON WITH VALUES IN PREVIOUSLY PUBLISHED WORKS

According to the current-voltage characteristic shown in Fig. 5.1, the conductive channel undergoes a transition between an abnormal glow discharge and a non-thermal arc with each current pulse. Therefore, similar to the previous section, the scattering results are compared in table 5.2 with the most relevant reference values obtained for glow discharges, gliding arcs and nanosecond pulsed discharges. For comparability reasons, only references are chosen in which the discharge is operated under conditions close to those in this work, i.e. at atmospheric pressure with nitrogen or compressed air as plasma gas. The references are also subdivided according to the method by which the parameters are determined, i.e. experimentally or by modeling. If the authors combined experimental techniques (usually emission spectroscopy and electrical measurements) with calculations to determine the electron parameters, this type of work is marked as "mixed". Furthermore, for a better overview, the discussion is organized by type of discharge, comparing first glow discharges with the results obtained when the scattering setup is triggered between two consecutive pulses, followed by a comparison with gliding arcs, and finally with nanosecond pulsed discharges.

Table 5.2: Comparison of the scattering results with the most relevant reference values.

| Type of work | experimental | experimental | experimental | mixed | experimental |
|---|---|---|---|---|---|
| Discharge type | transient spark | transient spark | glow | glow-to-arc transition | glow |
| Gas | $N_2$ | $N_2$ | – | Air | $N_2$ |
| $f$ (kHz) | 60 | 60 | DC | DC | DC |
| $i$ (A) | $\sim 1$ ($I_{peak}$) | 0.08 ($I_{valley}$) | 20 | 0.25 | 0.5 |
| $\overline{n}_e$ (m$^{-3}$) | $1.7 \times 10^{21}$ | $1.4 \times 10^{21}$ | $0.6 \times 10^{19}$ | $2.0 \times 10^{19}$ | $1.0 \times 10^{20}$ |
| $\overline{T}_e$ (K) | 41000 | 39000 | 58000 | – | 9500 |
| $\overline{T}_h$ (K) | 5900 | 4900 | – | 5500 | 3500 |
| Ref. | this work | this work | [149] | [152] | [114] |

| Type of work | experimental | experimental | mixed | mixed | mixed |
|---|---|---|---|---|---|
| Discharge type | non-thermal arc | gliding arc | gliding arc plasmatron | ns-pulsed | ns-pulsed |
| Gas | – | $N_2$ | $N_2$ | Air | Air |
| $f$ (kHz) | DC | 0.05 | DC | 30 | 0.01 |
| $i$ (A) | < 50 | 0.13 | 0.23 | 30 (peak) | 200 (peak) |
| $\overline{n}_e$ (m$^{-3}$) | < $10^{21}$ | $1.0 \times 10^{18}$ | $1.6 \times 10^{21}$ | $1.0 \times 10^{21}$ | $1.0 \times 10^{23}$ |
| $\overline{T}_e$ (K) | < 23000 | 10000 | – | 30000 | 40000 |
| $\overline{T}_h$ (K) | < 5800 | < 2600 | $\sim 6000$ | 5300 | < 1200 |
| Ref. | [149] | [34] | [60] | [139, 140] | [109] |

– *Comparison with glow discharges.* As reported by Reece Roth, the author of Fig. 5.1 at the beginning of this chapter, electron density of an abnormal glow discharge at atmospheric pressure ranges typically below $10^{19}$ m$^{-3}$ [149], about two orders of magnitude lower than the results determined in this work for the discharge triggered at $I_{valley}$. Risacher *et al.*, who investigated low-current arc discharges in a pin-plate arrangement operated in air at atmospheric

pressure, estimated slightly higher electron densities in the range of $2.0 \times 10^{19}$ m$^{-3}$ by solving the Elenbaas-Heller model under assumption of local thermal equilibrium [152]. The discharge was operated at a constant current of 250 mA for which a heavy particle temperature of 5500 K was spectroscopically measured, a value in the range of those measured here. Similar results for glow discharges are also given by others [4, 5]. Machala *et al.* reported electron densities one order of magnitude higher, when a glow discharge is constricted by a tube and operated with a swirled gas flow [114]. Due to such operating conditions, the discharge channel is expected to be more confined and as a result its diameter is reduced. According to the authors, this reduction increases the current density and thus a higher $n_e$ is measured. Furthermore, they also stress the stabilizing effect of a swirled gas flow. The swirl stabilization is found to be so effective that discharges with lengths of more than 100 mm could be reliably operated. The lower heavy particle temperature given in [114] compared to those estimated here, is most probably caused by the much higher gas flow rates, in excess of 100 l/min, at which the constricted glow discharges were operated. Although the electron temperature stated in [149] is suggested to be in a similar range to those estimated here (see Tab. 5.2), other researchers report values that are significantly lower [5, 114], which is why the measured electron temperatures cannot be assessed at this point. Since the reference discharges were operated with constant current, the difference may be attributed to the pulsed operation principle of the system investigated in this work.

– *Comparison with non-thermal / gliding arcs.* The electron density for a non-thermal arc is reported to range between $10^{20}$ m$^{-3}$ and $10^{21}$ m$^{-3}$ according to [149], which is in good agreement with the values measured within this work. Also the heavy particle temperatures correlate well, as can be seen in table 5.2. The so-called gliding arcs are another research area in which low-current discharges operated at atmospheric pressure are studied. One of the first groups of researchers to reignite research around gliding arcs in the early 1990s was led by A. Czernichowski. Although the researchers reported in [34] that electron densities of about $0.5 \times 10^{21}$ m$^{-3}$ were reached for gliding arcs operated with constant current of about 0.2 A in argon or argon-hydrogen mixtures, lower values were determined when the discharge was operated in air. Thereafter, when driven at mains frequency by a step-up transformer capable of 10 kV and a maximal current of 130 mA, a $n_e$ of about $10^{18}$ m$^{-3}$, $T_e$ of 10000 K and $T_h$ between 1700 K and 2600 K are reported for the non-thermal mode of operation [34]. Similar electron densities to those presented by Czernichowski *et al.* are reported in [62], while similar heavy particle temperatures in [129, 188]. Although the above results are lower than those estimated in this work, recent investigations of gliding arcs constricted by tubes, referred to as gliding arc plasmatron by Gröger *et al.* [60] or tornado discharge by researchers collaborating with Gutsol and Fridman [80], have shown that almost identical electron density and heavy particle temperature values to those given in chapter 4 can be reached by such discharges. The values presented in table 5.2 are determined by Gröger *et al.* for such a constricted gliding arc operated with nitrogen at a constant current of 230 mA [60]. The rotational and vibrational temperatures were thereby estimated by fitting of synthetic spectra after measuring of the SPS $(0,0)$- and FNS $(0,0)$-transitions, as was the case here. Thereafter, the authors determined the reduced electric field and used it to calculate the electron density with a collisional-radiative model of the discharge. The resulting $n_e$ was estimated to be $1.6 \times 10^{21}$ m$^{-3}$ [60]. According to the observations of Machala *et al.* discussed above [114], the increase in electron density when compared to the results reported by others [34, 62, 129] is most probably caused by the constriction of the discharge. Even though the $n_e$ value as well as the $T_h$ value agree well with the estimates presented here, the reason for the elevated electron temperature measured in this work is not yet clear as Gröger *et al.* did not state any $T_e$ values. However, the discharges discussed above are operated at constant currents or at relatively low frequencies, again suggesting that the electron temperature may be correlated with the frequency of the pulsed operating experiment (see next discussion point).

– *Comparison with nanosecond pulsed discharges.* Several research groups investigated experimentally nanosecond repetitively pulsed discharges to determine the electron parameters, reporting thereby on the transitional character between the glow and spark regimes of the conductive channel [109, 140]. Thus, to verify whether the relatively high electron temperatures are related to the operating frequency of the excitation source of a discharge, some of these studies are analyzed. Lo *et al.* reported $T_e$ values in the range of 40000 K for voltage pulses of 35 kV and 25 ns duration [109]. However, due to the current reaching over 200 A in the first 15 ns of the discharge, high electron densities of over $10^{23}$ m$^{-3}$ are deduced from evaluation of spectral lines emitted by singly ionized atomic nitrogen. This is to be expected since the current density $j$ is directly proportional to the electron density $n_e$ according to $j = -q_e n_e v_{e,th}$, with $q_e$ being the electron charge and $v_{e,th}$ the drift velocity of electrons [148]. Even higher $T_e$ and $n_e$ values are reported by Orrière *et al.*, who used a similar method as Lo *et al.* to estimate the electron parameters of a discharge driven by pulses of nanosecond duration at a repetition rate of 8 kHz [138]. Pai *et al.*, on the other hand, studied a nanosecond discharge operated in air by 8.3 kV high voltage peaks pulsed at 30 kHz [139]. For these working conditions, peak current values of 30 A were measured, resulting in a rotational temperature of 5300 K reached about 40 ns after a discharge took place. The temperature was also determined by fitting of synthetic spectra to the SPS $(0,0)$-transition. Both the electron density and temperature on the other hand are estimated based on calculations of the discharge radius and collision frequency between electrons and heavy particles [139]. According to table 5.2, the determined density of about $10^{21}$ m$^{-3}$ and electron temperature of about 30000 K reported by Pai *et al.* agree well with the results estimated in this work. Based on the above discussion, the initial suggestion that the relatively high electron temperature is related to the pulsed nature of the discharge seems to be confirmed. This issue will be discussed later in more detail in section 5.3.

As mentioned in the above comparison, several researchers determined spectroscopically the diameter of the discharge to estimate the electron temperature in subsequent calculations [60, 139, 152]. In contrast, due to the high spatial resolution achieved in this work, the diameter of the discharge channel is estimated here using laser scattering diagnostics (see Fig. 4.3). The plateau width observed in the radial distribution of $T_h$ ranges between 0.2 mm and 0.3 mm and is considered to be the core diameter of the discharge channel. This assumption appears to be correct when the diameter is compared with already published references. Hence, Pai *et al.* estimated a diameter of about 0.3 mm for the nanosecond pulsed discharge studied in their work [139]. The core diameter estimated by Gröger *et al.* amounted in turn to about 0.5 mm [60]. Lebouvier *et al.* modeled a low-current high-voltage DC plasma jet operated with a constant current in the range of 0.5 A and an air flow rate of 25 l/min in [105]. Although the calculations were conducted under the assumption of thermal equilibrium, i.e. $T_e = T_h$, and the geometry of the model is slightly larger compared to the plasma generator studied in this work, with a nozzle length of 70 mm and an outlet opening of 8 mm, analogous conclusions can be drawn when comparing the results. According to the radial temperature profiles presented by the authors, the diameter of the discharge channel at nozzle outlet is about 0.4 mm [105]. Furthermore, similarly to high speed images discussed in section 4.4, the calculated discharge channel is blown out of the nozzle several millimeters, reverses and reattaches to the front of the nozzle.

Apart from the references summarized in table 5.2, several researchers have analyzed comparable plasma systems to the one studied here [41, 81, 86, 95, 99, 146]. Though only few have determined the temperature of the effluent plasma jet using emission spectroscopy. Kubota *et al.* analyzed spectroscopically a comparable plasma system operated at a pulse frequency of 19 kHz with nitrogen flowing at 30 l/min [99]. The input power was reported to be in the range of 1500 W. Based on the second positive $(0,0)$-transition the rotational temperature was estimated to be about 5000 K inside the plasma generator and between 3000 K and 4000 K at nozzle exit. For the same plasma system, also pulsed at 19 kHz but working with a compressed air gas flow rate of 76.6 l/min, Dowling *et al.*

estimated a rotational temperature of about 1760 K at nozzle exit using the $(0, 2)$-transition spectra of the second positive system [41]. If a linear relationship between gas flow and temperature would be assumed in a first approximation for this result, than a rotational temperature of approx. 4500 K at an air flow rate of 30 l/min could be expected. Both results agree well with the temperature values estimated in this work (see Tab. 5.2).

Concluding, based on the above comparison with published works, it can be stated that the plasma parameters estimated in chapter 4 are plausible. Furthermore, the simple, compact and mobile laser scattering setup proven to be well suited for determining of electron parameters in transient plasmas at atmospheric pressure.

## 5.3 Observed physical effects

Apart from the validity of the experimentally determined values of the main plasma parameters in a time averaged form, the scattering results show additional effects that are addressed in this section to complete the discussion. These effects are related to the temporal evolution of the heavy particle temperature, discussed in section 5.3.1, and to the temporal evolution of the electron parameters, i.e. $n_e$ and $T_e$, discussed in section 5.3.2. In section 5.3.3, a simple model is used to explain the correlation between the time evolution of the electron density and a periodic change of the excitation current.

### 5.3.1 Temporal evolution of the heavy particle temperature

The scattering results show that slightly lower $T_h$ values are observed when either the frequency or the power setting is reduced (see Fig. 4.8). As mentioned at the beginning of this chapter, according to theoretical models of Lu [113] as well as Naidis [132], the gas temperature in pulsed discharges is associated with the dissipated power rather than the trajectories of voltage and current. Naidis, who modeled nanosecond pulsed spark discharges in air, observed no significant difference in the heavy particle temperature for pulses twice as long at half the initial frequency of 30 kHz [132]. The current trajectory measured at a pulse frequency of 60 kHz for the analyzed plasma generator is characterized by a relatively low amplitude and also low slew rates (see Fig. 4.1) what nonetheless results in a higher gas temperature. The behavior is reversed for the lower pulse frequency at which a higher amplitude and steeper current slew rates result in a lower $T_h$ value. Assuming that the power supply delivers a nearly equal electric charge and thus also a similar energy amount into the system with each current pulse, this indicates that a higher power is dissipated in the plasma generator with increased frequency, since with a faster repetition of similar pulses the power transferred to the discharge increases (under the above assumption). Such an increase for higher pulse repetition rates is measured at the exit of the power supply (see Fig. 5.2). Although a slower response of $T_h$ to steeper current slopes can be observed in the temporal distribution of the mean plasma parameters (see Fig. 4.7), this does not seem to have a significant effect on the mean temperature. Thereafter, the above statement that the heavy particle temperature depends on the dissipated power can be confirmed experimentally for the analyzed system.

The effect of a delayed response of heavy particles to input power changes (see Fig. 4.7), was observed by several researcher groups. An increase in heavy particle temperature was observed by Gutsol *et al.* while the current and power decreased at the same time [62]. A possible explanation for this "memory effect", as called by Gutsol *et al.*, is provided by Janda *et al.* [76]. According to their observations, the effect is connected with the exchange of rotational and vibrational energy leading to heating of heavy particles and consequently to slower decrease of electron density at elevated temperatures. The slower decrease of $n_e$ is explained by the authors with a strong temperature dependence of the electron recombination reactions, which slow down with increasing gas temperature. Another reason Janda *et al.* give for this behavior is a possible accumulation of various charged species in the discharge channel when operating at higher frequencies, which could lead to the appearance of

a space charge field that has to be first overcome by the external electric field. The influence of gas temperature and gas flow on discharge behavior is also discussed in [97, 114]. The experiment and calculation results of Machala *et al.* show that due to the elevated temperature caused by vibrational-translational energy relaxation, the particle density in the discharge channel is significantly reduced what enhances the reduced electric field and thus accelerates the ionization processes within the channel [114]. According to the above discussion, the effect observed in Fig. 4.7, that a higher gas temperature is measured even though the current is decreasing, is attributed to such a "memory effect". Furthermore, this effect is most likely responsible for the existence of the glow discharge between consecutive pulses as depicted in the high speed images in section 4.4.

### 5.3.2 Temporal evolution of free electrons

The parameters of free electrons estimated in this work appear to be relatively insensitive to fast changes of the discharge current (see Tab. 5.2 or Fig. 4.7 and Fig. 4.8). According to a theoretical model of a low-current DC discharge developed by Benilov and Naidis [11], a reduction of electron density by about an order of magnitude can be expected when the current value decreases from amperes to milliamperes. This reduction is attributed by the authors to a change in ionization rate. Hence for lower current values, for which non-LTE conditions are assumed, higher values of the reduced electric field are expected and thus the ionization rate of neutral particles is mainly controlled by electron impact. For higher currents, for which LTE conditions are assumed by the authors, lower $E/n$ and higher $T_h$ values are expected, hence the excitation process leading to ionization is reported to be controlled instead by associative ionization of metastable states [11]. A comparable statement can be found in the works of Akishev *et al.*, who reported that the excitation and de-excitation rates of nitrogen electronic states change with increasing temperature of heavy particles [4, 5]. While the excitation of the ground state $X^1\Sigma_g^+$ is mainly governed by electron impact, the excitation of metastables such as $A^3\Sigma_u^+$ to higher energy states as well as most de-excitation reactions are caused by collisions with other heavy particles. Thus, according to Akishev *et al.*, for low $E/n$ values the resulting free electrons are predominantly provided by associative ionization of following states

$$N_2\left(A^3\Sigma_u^+\right) + N_2\left(a'^1\Sigma_u^-\right) \rightarrow N_4^+ + q_e\,,$$
$$N_2\left(a'^1\Sigma_u^-\right) + N_2\left(a'^1\Sigma_u^-\right) \rightarrow N_4^+(X) + q_e\,,$$

although both initial states, $A^3\Sigma_u^+$ and $a'^1\Sigma_u^-$, are formed by collisions with electrons.

Naidis continued to develop the mathematical models presented in [11] and conducted calculations for low-current DC discharges stabilized by a longitudinal air flow [131] and calculations of nanosecond repetitively pulsed sparks [132]. As shown in [131], the influence of gas flow is only relevant when operating with currents of a few tens of milliamperes (non-LTE case). Much more interesting are the simulations of nanosecond repetitively pulsed sparks presented in [132]. The initial pulse conditions were adopted from experiments with a voltage amplitude of 5 kV, a pulse length of 5 ns and repetition rate of 30 kHz. According to the simulated results, the number density decreases after a pulse due to electron-ion recombination with a characteristic time constant of approximately 30 µs. Electron recombination times of about 10 µs are also reported by Kruger *et al.* [98]. A slow recombination rate of electrons is furthermore observed by Orrière *et al.* while investigating a nanosecond pulsed microgap discharge operated in air at a frequency of 8 kHz [138]. Similarly to others, the researchers postulated that the slower-than-expected recombination rate may originate from a combination of associative and stepwise ionization processes during the recombination phase. Moreover, they suggest that a high density of excited nitrogen atoms may also play a significant role in slowing down the recombination of free electrons [138]. The degree of dissociation can be assessed qualitatively, as suggested by Hontañón *et al.* in [67], based on the line intensities emitted by atomic nitrogen. Thereby

it is assumed, that the emitted line intensity is related in a first approximation to the number density of the excited atoms. Several lines radiated by excited atomic nitrogen between 818 nm and 825 nm are therefore plotted in Fig. 5.7 for both frequencies studied and clearly indicate that a higher degree of dissociation may be expected for the lower frequency according to the above assumption.
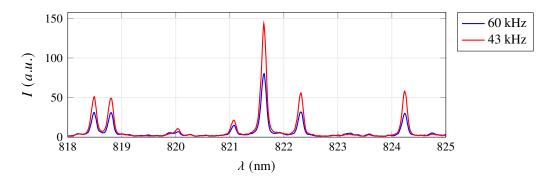


Figure 5.7: Comparison of line intensities emitted by atomic nitrogen suggesting an increased dissociation degree for lower operating frequencies.

The correlation of the above observations with the experimental results obtained in this work, suggests that the excitation and de-excitation processes of heavy particles may be responsible for the slow decay of electron parameters observed here, particularly since the plasma generator operates at even higher frequencies. Hence, when the current is rising the excitation and dissociation of nitrogen molecules is mainly caused by electron collisions. This assumption is supported by the fact that higher emission intensities of atomic nitrogen lines are observed for higher $T_e$ values (corresponding to a lower frequency - see Fig. 5.7), and that similar heavy particle temperatures where spectroscopically determined for the $N_2 \left( C^3\Pi_u \rightarrow B^3\Pi_g \right)$ and $N_2^+ \left( B^2\Sigma_u^+ \rightarrow X^2\Sigma_g^+ \right)$ transitions (see Fig. 4.10 and Fig. 4.11). According to Gröger et al., this is only possible when both states are populated by electron impact directly from the $X^1\Sigma_g^+$ ground state of molecular nitrogen [60]. Both electron density and electron temperature increase with increasing current and energy is transferred to heavy particles. After a pulse the reduction of the electron density does not immediately follow the current trajectory due to complex de-excitation reactions which slow down the recombination rate of free plasma electrons. This maintains a relative high electron density and may even lead to formation of further electrons. As discussed in section 5.2.2, the relatively high electron temperature is understood to be related to the pulsed operation mode of the system. According to [15, 98], pulsed operation requires a higher electron temperature to sustain a similar electron density as when the discharge is operated at constant current, since the energy transfer between free electrons and atoms (or molecules) is more inefficient due to the presence of charged or not yet recombined (when the pulse repetition rate is high enough) particles. Furthermore, the reported recombination times of electrons, which are of the same order of magnitude as the pulse period of the power supply [98, 132, 138], make the rather small temporal variance of the electron temperature understandable.

The above hypothesis may also explain the difference in the electron parameters observed for both frequencies. As shown in table 5.1, a higher electron density and higher electron temperature are measured for the lower operating frequency of 43 kHz. At this frequency however, a lower power is coupled into the generator (see Fig. 5.2) and the current is characterized by significantly steeper slew rates (see Fig. 5.4). As already discussed, nitrogen is a plasma gas whose recombination displays a somewhat slower rate due to de-excitation channels consisting of several steps. The resulting recombination time scale at atmospheric pressure happens thus to be in the same order of magnitude as the considered repetition period ($\sim$ 23 µs for 43 kHz and $\sim$ 17 µs for 60 kHz). If a recombination time of $\sim$ 20 µs is assumed, a slight change in the repetition rate of the pulsed excitation can strongly influence the ionization degree. Accordingly, if the repetition period is shorter than the recombination

time scale, each current pulse excitation encounters a plasma channel which is not yet fully neutralized and whose still-charged ions may strongly disturb and hinder the acceleration of the free electrons, making any collision less efficient for an eventual ionization. As a result, the higher repetition rate of 60 kHz leads to a plasma with a lower ionization than in the case of the 43 kHz pulse repetition rate. Thereafter, the scattering results summarized in table 5.1 suggest, that the ionization processes may be more efficient at lower frequencies for the discharge studied. Moreover, the higher current amplitude and steeper slew rates observed for this repetition rate when measuring prior to the plasma generator, suggest that these processes are correlated with the shape of the excitation pulses. A simple qualitative explanation attempt for this is given in the following section.

### 5.3.3 Simplified model describing plasma's response to a periodic current pulse

As stated at the end of previous section, the measured current and the resulting electron density are correlated with each other. To describe the response of the plasma's free electrons to periodic current changes, the following simplified model is proposed. As briefly discussed in section 5.3.2, the details of the ionization during the high current phase, or of the recombination during the low current phase, are quite complex. Assuming that these details cannot be fully resolved experimentally, the response of the plasma to a current change can be modeled in a first approximation with a proportional element with time delay (PT1 element). Such an element behaves similarly to a low-pass filter and is described by a complex transfer function (after a Laplace transform) $\hat{g}(s) = \dfrac{V}{1 + \tau s}$. Thereby:

- $V$ represents the coupling strength between the exciting current pulse $i(t)$ and the resulting free electron density $n_e(t)$. In the following discussion $V$ is assumed independent of the current amplitude $A_{max}$ (although this is physically never the case).

- $\tau$ is the characteristic time delay which describes the inertia of the system to change its ionization state. In principle $\tau$ can have a different value during the ionisation phase (high current amplitude) from that during the recombination phase (low current amplitude). Nonetheless, in the following qualitative discussion a single $\tau$ value will be considered for both phases.

To simplify the interpretation, a rectangular profile is assumed for the current pulses instead of triangular one. Thereafter, an electric current of period $T$ is assumed, consisting of a high amplitude phase and a low amplitude phase. During the high amplitude phase, an amplitude of $A_{max}$ is reach for a fraction $\xi$ of the period. During the remaining part of the period, a low amplitude of $A_{min}$ is assumed. Such an electric current of period $T$ is described mathematically as follows

$$i(t) = A_0 + A_1 \begin{cases} +1 & 0 \le t < \xi T \\ -1 & \xi T \le t < T \end{cases} \qquad \begin{aligned} A_0 &= \frac{A_{max} + A_{min}}{2} \\ A_1 &= \frac{A_{max} - A_{min}}{2} \end{aligned} \qquad (5.1)$$

with $0 < \xi < 1$. The Fourier transform of this current reads

$$i(t) = a_0 + \sum_{k=1}^{\infty} \left[ a_k \cos\left(\frac{2\pi k}{T} t\right) + b_k \sin\left(\frac{2\pi k}{T} t\right) \right] ,$$

$$a_0 = \frac{1}{T} \int_0^T i(t)\, dt = A_0 + A_1 (2\xi - 1) = A_{min} + \xi (A_{max} - A_{min}) ,$$

$$a_k = \frac{2}{T} \int_0^T i(t) \cos\left(\frac{2\pi k}{T} t\right) dt = \frac{2A_1}{\pi k} \sin(2\pi k \xi) = \frac{(A_{max} - A_{min})}{\pi k} \sin(2\pi k \xi) ,$$

$$b_k = \frac{2}{T} \int_0^T i(t) \sin\left(\frac{2\pi k}{T} t\right) dt = \frac{2A_1}{\pi k} [1 - \cos(2\pi k \xi)] = \frac{(A_{max} - A_{min})}{\pi k} [1 - \cos(2\pi k \xi)] . \quad (5.2)$$

If both $A_{min}$ and $A_{max}$ are now assumed to be high enough to maintain a certain ionization degree in a gas flow, i.e. to create and maintain a plasma, the density of free electrons $n_e(t)$ in the resulting plasma will react to the amplitude changes. At this point, it should be noted that the same discussion can be analogously repeated if the external input exciting the plasma state is an electric voltage instead of a current. The Laplace transform (denoted by ˆ) of the externally controlled current (5.2) which is switched on at $t = 0$ reads

$$\hat{i}(s) = a_0 \frac{1}{s} + \sum_{k=1}^{\infty} \left[ a_k \frac{s}{s^2 + \left(\frac{2\pi k}{T}\right)^2} + b_k \frac{\frac{2\pi k}{T}}{s^2 + \left(\frac{2\pi k}{T}\right)^2} \right] ,$$

leading to a response in the plasma density of free electrons given by

$$\hat{n}_e(s) \approx \frac{V}{1 + \tau s} \hat{i}(s) .$$

Followingly, when transformed back into the time domain (see Appendix E), it can be written

$$n_e(t) \approx V a_0 \left(1 - e^{-t/\tau}\right) + V \sum_{k=1}^{\infty} \frac{\left(-a_k + b_k \frac{2\pi k\tau}{T}\right)}{1 + \left(\frac{2\pi k\tau}{T}\right)^2} e^{-t/\tau}$$

$$+ V \sum_{k=1}^{\infty} \left[ \frac{a_k}{\sqrt{1 + \left(\frac{2\pi k\tau}{T}\right)^2}} \cos\left(\frac{2\pi k}{T}t - \arctan\left(\frac{2\pi k\tau}{T}\right)\right) \right.$$

$$\left. + \frac{b_k}{\sqrt{1 + \left(\frac{2\pi k\tau}{T}\right)^2}} \sin\left(\frac{2\pi k}{T}t - \arctan\left(\frac{2\pi k\tau}{T}\right)\right) \right] . \tag{5.3}$$

The assumption of an ionization/recombination time of $\tau \sim 20$ μs, according to section 5.3.2, for an operating frequency of $\frac{1}{T} \sim 60$ kHz results in $\frac{2\pi\tau}{T} \sim 8 > 1$. Hence the previous result (5.3) can be further approximated in a steady state, i.e. at $t \to \infty$, to

$$n_e(t) \approx V \left(A_{min} + \xi \left(A_{max} - A_{min}\right)\right)$$

$$- V\frac{T}{\tau} \xi \left(A_{max} - A_{min}\right) \sum_{k=1}^{\infty} \frac{\sqrt{1 - \cos(2\pi\xi k)}}{\sqrt{2}\pi^2 k^2} \cos\left(\frac{2\pi k}{T}t + \arctan\left(\frac{\sin(2\pi\xi k)}{1 - \cos(2\pi\xi k)}\right)\right) . \tag{5.4}$$

Thereafter, for the leading component (i.e. for $k = 1$), the response of the electron density is a superposition of a constant value of $V\left(A_{min} + \xi\left(A_{max} - A_{min}\right)\right)$ with an oscillation of amplitude $V\frac{T}{\tau}\xi\left(A_{max} - A_{min}\right)\frac{\sqrt{1 - \cos(2\pi\xi)}}{\sqrt{2}\pi^2}$. In other words, if the external excitation ranges between $A_{min}$ and $A_{max}$, the resulting electron density in plasma (and hence the current flowing along the discharge channel) oscillates with an amplitude scaling as $(T/\tau)\xi\left(A_{max} - A_{min}\right)$. Thus, this amplitude decreases with increasing frequency $1/T$ of the external excitation and its origin is simple - if the pulse repetition frequency $1/T$ increases, the characteristic inertia of the system characterized by $\tau$ (mainly the typical recombination time) is eventually no longer able to follow the repetition but saturates to the average value proportional to $A_{min} + \xi\left(A_{max} - A_{min}\right)$. Such a behaviour is observed for the studied plasma system (see Fig. 4.1). Consequently, in case of a much higher frequency (i.e. for $T \to 0$), the electron density and the current flowing through the channel will approach a constant value with a scaling factor of $A_{min} + \xi\left(A_{max} - A_{min}\right)$.

# 6

# CONCLUSION AND OUTLOOK

The main objective of this work was to investigate the properties of pulsed low-current discharges operated at atmospheric pressure in order to experimentally determine the relevant plasma parameters, in particular the electron number density and the electron temperature, since no information on these values could be found in published works so far. Another objective of this work was to verify the applicability of different diagnostic systems to such a discharge type, focusing on a simple laser scattering setup that allows the measurement of plasma parameters without any modifications. Thus, a commercially available system comparable to others was studied by the means of laser scattering, emission spectroscopy and high speed imaging. With these methods, a spatial distribution of $n_e$, $T_e$ and $T_h$ was obtained. The resolution and sensitivity of the scattering setup using a single spectrograph proved to be high enough to perform a measurement without a blocking mask. Furthermore, with the scattering diagnostics as well as emission spectroscopy setup synchronized with the working frequency of the plasma generator, a temporal distribution of the parameters was evaluated.

According to the results, depending on the operating frequency, an electron density between $1.7 \times 10^{21}$ m$^{-3}$ and $2.0 \times 10^{21}$ m$^{-3}$ with electron temperatures in the range of 40000 K can be expected for a pulsed low-current nitrogen discharge operated at atmospheric pressure. A heavy particle temperature of about 6000 K is reached in the core of the discharge channel, with the values decreasing further downstream on the axis of the effluent plasma jet from 4000 K to 2000 K at typical treatment distances of 10-15 mm from nozzle outlet. Furthermore, the diameter of the discharge channel is estimated to be about 0.2 mm. Due to the complex nature of the de-excitation processes of nitrogen, relatively slow electron recombination rates are observed and thus the once ionized channel does not extinguish between consecutive pulses, but rather transitions with each pulse from a glow discharge to a spark. Thereafter, the observed influence of the temporal changes of the excitation current on the estimated plasma parameters is slightly less than 20 %. Moreover, it could be shown that the reaction of the plasma on a current change can be modelled in a first approximation with a proportional element with time delay. Consequently, the measured values allow a direct coupling of the plasma properties with the voltage and current traces and hence with the corresponding adjustable parameters of the power supply, i.e. the operating frequency and the amplitude of the pulses. Since the input of the proposed model is an electrical trace, conclusions can be subsequently drawn for other operating points of a discharge.

The plausibility of the results was confirmed by a comparison of the laser scattering results with the emission spectroscopy as well as with reference values published for low-current glow, gliding and pulsed discharges in previous works. The comparison showed that the estimated values are in good agreement with the reference ones. It also showed that the relatively high electron temperature can be related to the pulsed operation mode of the system under study. Based on the obtained findings, the hypothesis that the temperature of heavy particles is determined by dissipated power, while the electron parameters, and therefore to some extent the chemical reactivity of the plasma, are defined

by the shape of the excitation pulse could be confirmed for this type of discharge. With additional high speed imaging diagnostics, the lateral motion of the discharge channel as well as the temporal progression of the cathodic attachment point was evaluated, which allow an even better understanding of the operating principle of such discharges. Once steady-state operation is reached and the discharge channel extends out of the nozzle exit, the influence of the gas flow on the radial motion of channel appears to be much less pronounced than initially expected. Additionally, the discharge channel is not relocated or shortened with each current pulse, as reported in previous works. The diagnostics also revealed that pressure waves are emitted with each current pulse, which may interfere with the inner walls or surroundings of the generator and thus lead to possible instabilities.

In conclusion, the results obtained in this work contribute significantly to the understanding of pulsed low-current discharges operated at atmospheric pressure. The presented results facilitate the development and validation of a computational model, which can be based on one of the existing works [39, 166, 169], to provide a more accurate chemical description of the plasma composition. With this knowledge, such discharges can be better adapted to specific applications in industrial or experimental environments, such as chemical vapour deposition, plasma-activation of liquids, $CO_2$ reforming, or, in general, applications with more stringent plasma chemistry requirements. Furthermore, the methods employed in this work can be simplified to design more application-oriented diagnostic systems. The laser scattering technique itself, although a simple and compact setup has proven to be sufficient for the determination of plasma parameters, appears to be suitable only for applications under laboratory conditions. The major hurdle to overcome with this measurement method is the low intensity of the scattered signal, which requires the use of a (currently still) quite expensive intensified camera. Nevertheless, other diagnostics used in this work can be simplified to allow the derivation of an industrially applicable diagnostic or process monitoring system. In particular, the spectroscopic estimation of the heavy particle temperature, which can be simplified as suggested in section 2.2.6 or described by Gardet *et al.* [52], coupled with the availability of inexpensive and integrable spectrometers [14] and development of integrated spectral sensors, such as the AS7265x family from ams-OSRAM AG, Premstaetten, Austria [6] or others [168, 177] costing no more than a few euros, appears to be a viable solution for a real-time monitoring system. Furthermore, the reactivity of a plasma can be estimated spectroscopically by relating the intensity of spectral lines of one transition to that of another, for example $I(N_2^+)/I(N_2)$ as suggested in [21, 60]. The devices suggested above should also be able to detect different substances introduced into the plasma. Another process monitoring method can be derived from the pressure waves emitted by the discharge, which can be captured by a microphone or by a structure-borne sound transducer. An extensive evaluation of such a microphone-based process diagnostic technique was elaborated by Law *et al.* and can be found in [104]. One advantage of a real-time monitoring system, whether sound- or spectrum-based, is that it can serve as quality assurance and a feedback loop for the control the plasma system simultaneously. Such a system, with proper calibration, can link the microscopic phenomena occurring in a plasma with the macroscopic phenomena achieved on the treated surface, which is essential for more and more environmental- and health-oriented applications that help to keep the Earth's ecosystem in balance. The latter should be the main goal of any future research work.

# Appendices

# A

# INFLUENCE OF THE MAGNETIC FIELD ON A POINT CHARGE

The force exerted by an incident electromagnetic wave on a point charge carrier moving with velocity $\vec{v}$ is a sum of

$$\vec{F} = \vec{F}_{el} + \vec{F}_{mag} = q\vec{E} + q\vec{v} \times \vec{B},$$

where $q$ denotes the charge, $\vec{E}$ the electric field strength and $\vec{B}$ the magnetic flux density. The electric and magnetic field are related by the impedance of free space $Z_0$, with

$$Z_0 = \frac{E}{H} = \sqrt{\frac{\mu_0}{\epsilon_0}} = \frac{1}{\epsilon_0 c}$$

with $H$ being the magnetic field strength, $\mu_0$ the vacuum permeability, $\epsilon_0$ the vacuum permittivity and $c$ the speed of light. Thereafter, for the force fractions can be written

$$\frac{F_{mag}}{F_{el}} = \frac{vB}{E} = \frac{v\mu_0 H}{E}$$

$$= \frac{v\mu_0 \sqrt{\frac{\epsilon_0}{\mu_0}} E}{E} = v\sqrt{\epsilon_0 \mu_0} = \frac{v}{c}.$$

According to the above discussion, the force acting on a point charge due to the magnetic field is smaller by a factor $v/c$ than that due to the electric field. In other words, a point charge must reach the speed of light for the B-field to have a similar effect as the E-field. Since the latter never becomes the case in plasmas operated at atmospheric pressure, due to the many collisions between particles, the effect of the B-field of an electromagnetic wave on a point charge can be neglected compared to the effect of the E-field of the same electromagnetic wave.

In the far field of an electric dipole, the following applies to the power density of the emitted electromagnetic wave

$$\vec{S} = \vec{E} \times \vec{H},$$

or in simplified form

$$S = E \cdot H = \frac{E^2}{Z_0} = \sqrt{\frac{\epsilon_0}{\mu_0}} E^2.$$

# B

# CALCULATION OF ROTATIONAL RAMAN SPECTRA

As presented in section 2.1.4, the rotational Raman spectrum can be calculated based on tabulated values for a known heavy particle temperature. Accordingly, the equations presented in section 2.1.4 are implemented in a numerical computation environment that allows an automated calculation of a spectrum for a given temperature (denoted with `in_T`). The function presented in the next section was used to obtain Fig. 2.8 and Fig. 2.9.

## B.1 CODE IMPLEMENTATION

The following code can be implemented in any numerical computing environment. In this work, a free and open source software available under the GPL License called Scilab (www.scilab.org) is used.

```
1  const.ee = 1.60218D-19;                // Electron charge [C]
2  const.c = 2.998D8;                      // Speed of light [m/s]
3  const.h = 6.6261D-34;                   // Planck's constant [J*s]
4  const.kB = 1.3807D-23;                  // Boltzmann constant [J/K]
5  laser.wavelen = 532E-9;                 // wavelength [m]
6  laser.E_pulse = 0.3;                    // pulse power in [J]
7  laser.t_pulse = 6E-9;                   // pulse time in [s]
8  P_i = laser.E_pulse/laser.t_pulse;      // incident laser power
9
10 L_det = 1E-3;                           // detection length in [m]
11 N_density = 1.138;                      // density of nitrogen in [kg/m^3] @ 300 K
12 diff_cross_sec_Rayleigh = 616.465E-34;  // differential cross section
13
14 function out = calc_roto(in_T)
15 dat = molecular_data();                 // molecular data from Herzberg
16                                         // -> rotational constant B for energy
17 // rotational quantum number
18 J = 0:50;
19 // energy of each rotational state
20 E_J = (dat(1,5).*const.ee).*J.*(J+1);
21 // wavelength of each rotational state
22 lam_Jplus = laser.wavelen + ((laser.wavelen^2)./(const.h.*const.c)).* ..
23                     dat(1,5).*const.ee.*(4.*J+6);    // Stokes
24 lam_Jminus = laser.wavelen - ((laser.wavelen^2)./(const.h.*const.c)).* ..
25                     dat(1,5).*const.ee.*(4.*J-2);    // anti-Stokes
26 // Placzek-Teller coefficients
27 Placzek_plus = 3.*(J+1).*(J+2)./(2.*(2.*J+1).*(2.*J+3));    // Stokes
28 Placzek_minus = 3.*(J).*(J-1)./(2.*(2.*J+1).*(2.*J-1));     // anti-Stokes
29 // polarizability anisotropy
```

**B**

```
30 gamma_sqr = 0.395E-82;                // (constant +/-8%) in [F^2*m^4]
31 // differential cross section for each case
32 diff_cross_sec_plus = (64*%pi^4/(45*const.eps0^2)).*Placzek_plus.* ..
33                                        (gamma_sqr)./(lam_Jplus.^4)
34 diff_cross_sec_minus = (64*%pi^4/(45*const.eps0^2)).*Placzek_minus.* ..
35                                        (gamma_sqr)./(lam_Jminus.^4)
36 // degeneracy
37 even_odd = modulo(J,2);        // find if J is an even or odd number
38 g_J = even_odd.*3;
39 g_J(~even_odd) = 6;
40 // approx. rotational partition function
41 Q = 9*const.kB*in_T/(2*dat(1,5).*const.ee);
42 // density of the rotational state J
43 n_J = (N_density./Q).*g_J.*(2.*J+1).*exp(-E_J./(const.kB.*in_T));
44 // scattered power of each Raman peak normalized with Rayleigh scattering
45 // cross section
46 P_iminus = n_J.*diff_cross_sec_minus/diff_cross_sec_Rayleigh;
47 P_iplus = n_J.*diff_cross_sec_plus/diff_cross_sec_Rayleigh;
48
49 // sort values by wavelength
50 a = [];
51 b = [];
52 k = 1;
53 for i=length(lam_Jminus):-1:1
54     a(1,k) = lam_Jminus(i);
55     b(1,k) = P_iminus(i);
56     k = k+1;
57 end
58 k = 1;
59 for i=(length(lam_Jminus)+1):1:(length(lam_Jminus)+length(lam_Jplus))
60     a(1,i) = lam_Jplus(k);
61     b(1,i) = P_iplus(k);
62     k = k+1;
63 end
64 a = [a*1E9; b];
65 // calculate spectrum considering instrumental profile
66 stepsize = 0.01;
67 apparatus = 0.22;                    // instrumenal profile in [nm]
68 lambda_syn = [];
69 lambda_syn = round(min(a(1,:))):stepsize:ceil(max(a(1,:)));
70 for i=1:length(lambda_syn)
71     for j=1:length(a(1,:))
72         tmp(i,j) = (b(1,j)/sqrt(2*%pi*apparatus^2))*exp(-(a(1,j)- ..
73                                        lambda_syn(i))^2/(2*apparatus^2));
74     end
75 end
76
77 // Output of values
78 for i=1:(size(tmp, 'r')-1)
79         out.intens(1,i) = sum(tmp(i,:));
80 end
81 out.lambda = lambda_syn(1:(length(lambda_syn)-1));
82 out.a = a;
83 out.diff_cross_sec = [lam_Jminus, lam_Jplus; ..
84                       diff_cross_sec_minus, diff_cross_sec_plus];
85 // Plot
86 scf();
87 plot2d(a(1,:), a(2,:), -5);
88 plot2d(out.lambda, out.intens, 5);
89 endfunction
```

# C

# CALCULATION OF THE PLASMA COMPOSITION BASED ON A TWO-TEMPERATURE MODEL

For the calculation of the gas composition a two-temperature plasma model is assumed, with a Maxwell-Boltzmann distribution function of the electrons and a Maxwell-Boltzmann distribution of heavy particles. Hence, the free electrons are assumed to be in local thermal equilibrium among themselves reaching an equilibrium temperature $T_e$ and similarly the heavy particles reach an equilibrium temperature $T_h$ among themselves. In addition, it is assumed that the heavy particle temperature applies to molecules as well as atoms regardless of their state, i.e. for both neutral and ionized particles. Thereafter, rotational and vibrational energy levels are assumed to be populated by heavy particle collisions and hence are also governed by $T_h$ [46]. As stated in section 2.2.5 the calculation is based on tabulated data.

Due to the local thermal equilibrium, the dissociation and ionization processes are assumed to occur with the same frequency as the recombination processes, hence the calculation is based on following "Saha" factors

$$\text{molecule dissociation:} \quad \frac{n_N^2}{n_{N_2}} = \frac{(Z_N)^2}{Z_{N_2}} \left( 2\pi \frac{\frac{m_N^2}{m_{N_2}} k_B T_h}{h^2} \right)^{3/2} \mathrm{e}^{-\frac{E_{dis,N_2}}{k_B T_h}} \equiv K_{d,N_2}\left(T_h\right) ,$$

$$\text{molecule ionization:} \quad \frac{n_e \, n_{N_2^+}}{n_{N_2}} = \frac{2 Z_{N_2^+}}{Z_{N_2}} \left( \frac{2\pi \, m_e \, k_B T_h}{h^2} \right)^{3/2} \mathrm{e}^{-\frac{E_{ion,N_2}}{k_B T_h}} \equiv K_{i,N_2}\left(T_h\right) , \qquad \text{(C.1)}$$

$$\text{1st atom ionization:} \quad \frac{n_e \, n_{N^+}}{n_N} = \frac{2 Z_{N^+}}{Z_N} \left( \frac{2\pi \, m_e \, k_B T_e}{h^2} \right)^{3/2} \mathrm{e}^{-\frac{E_{ion,N}}{k_B T_e}} \equiv K_{i,N}\left(T_e\right) ,$$

$$\text{2nd atom ionization:} \quad \frac{n_e \, n_{N^{++}}}{n_N} = \frac{2 Z_{N^{++}}}{Z_{N^+}} \left( \frac{2\pi \, m_e \, k_B T_e}{h^2} \right)^{3/2} \mathrm{e}^{-\frac{E_{ion,N^+}}{k_B T_e}} \equiv K_{i,N^+}\left(T_e\right) .$$

As can be seen, the Saha factors are a function of either the heavy species temperature or electron temperature. For nitrogen, the ionization of molecules occurs mainly under conditions of relatively low temperature and electron density, hence $T_h$ is assumed to govern the molecule ionization process [179].

The assumption of local thermal equilibrium implies that the following two conditions must be fulfilled. Firstly, the gas composition is quasi-neutral at lengths larger than the Debye length, hence

$$n_e = n_{N_2^+} + n_{N^+} + 2 n_{N^{++}} . \qquad \text{(C.2)}$$

Secondly, the ideal gas equation describing the influence of each gas species on the total gas pressure $P$ must be fulfilled. Thus,

$$\frac{P}{k_B T_e} = n_e + \frac{1}{\theta}\left(n_{N_2} + n_{N_2^+} + n_N + n_{N^+} + n_{N^{++}}\right) \quad \text{with} \quad \theta = \frac{T_e}{T_h}. \tag{C.3}$$

The quotient $\theta$ denotes the discrepancy between the electron and heavy particle temperature and is expected to vary between 5 and 15 for the analyzed nitrogen plasma. By combining the above equations C.1-C.3 it can be written

$$0 = n_e - n_{N_2}\frac{K_{i,N_2}}{n_e} - \sqrt{K_{d,N_2}\,n_{N_2}}\left(\frac{K_{i,N}}{n_e} + 2\frac{K_{i,N}\,K_{i,N^+}}{n_e^2}\right)$$
$$\equiv f_1\left(n_e, n_{N_2}\right), \tag{C.4}$$

$$0 = \frac{P}{k_B T_e} - n_e - \frac{1}{\theta}\left[n_{N_2}\left(1 + \frac{K_{i,N_2}}{n_e}\right) + \sqrt{K_{d,N_2}\,n_{N_2}}\left(1 + \frac{K_{i,N}}{n_e} + \frac{K_{i,N}\,K_{i,N^+}}{n_e^2}\right)\right]$$
$$\equiv f_2\left(n_e, n_{N_2}\right). \tag{C.5}$$

For better numeric solvability, the equations C.4, C.5 as well as C.1 are converted to be dimensionless with

$$\vec{x} = \begin{pmatrix} x_1 = \frac{k_B T_e}{P}\,n_e \\ x_2 = \frac{k_B T_e}{P}\,n_{N_2} \end{pmatrix} \quad \text{and} \quad K_i' = \frac{k_B T_e}{P}\,K_i,$$

where the index $i$ denotes the according dissociation or ionization process. As a result,

$$f_1\left(x_1, x_2\right) = x_1 - x_2\frac{K_{i,N_2}'}{x_1} - \sqrt{K_{d,N_2}'\,x_2}\left(\frac{K_{i,N}'}{x_1} + 2\frac{K_{i,N}'\,K_{i,N^+}'}{x_1^2}\right),$$
$$f_2\left(x_1, x_2\right) = 1 - x_1 - \frac{1}{\theta}\left[x_2\left(1 + \frac{K_{i,N_2}'}{x_1}\right) + \sqrt{K_{d,N_2}'\,x_2}\left(1 + \frac{K_{i,N}'}{x_1} + \frac{K_{i,N}'\,K_{i,N^+}'}{x_1^2}\right)\right]. \tag{C.6}$$

The solution

$$\vec{f}\left(\vec{x}\right) = \begin{pmatrix} f_1\left(x_1, x_2\right) \\ f_2\left(x_1, x_2\right) \end{pmatrix} = \vec{0}$$

is obtained iteratively by using the Newton-Raphson algorithm. The algorithm starts with a provisional solution $\vec{x}^{(prov)}$ and calculates an improved solution $\vec{x}$ iteratively by linearizing of $\vec{f}\left(\vec{x}\right)$ around the provisional solution until the equation system $\vec{f} = \vec{0}$ is satisfied in a given accuracy range. Hence, the algorithm is given by

$$\vec{0} = \vec{f}\left(\vec{x}\right) \approx \vec{f}\left(\vec{x}^{(prov)}\right) + \left(\frac{\partial \vec{f}}{\partial \vec{x}}\right)|_{\vec{x}^{(prov)}}\left(\vec{x} - \vec{x}^{(prov)}\right),$$

$$\begin{pmatrix} x_1 \\ x_2 \end{pmatrix} \approx \begin{pmatrix} x_1^{(prov)} \\ x_2^{(prov)} \end{pmatrix} - \left[\begin{pmatrix} \frac{\partial f_1}{\partial \vec{x_1}} & \frac{\partial f_1}{\partial \vec{x_2}} \\ \frac{\partial f_2}{\partial \vec{x_1}} & \frac{\partial f_2}{\partial \vec{x_2}} \end{pmatrix}|_{\vec{x}^{(prov)}}\right]^{-1}\begin{pmatrix} f_1 \\ f_2 \end{pmatrix}|_{\vec{x}^{(prov)}} \tag{C.7}$$

with

$$\frac{\partial \vec{f_1}}{\partial \vec{x_1}} = 1 + x_2 \frac{K'_{i,N_2}}{x_1^2} + \sqrt{K'_{d,N_2} x_2} \left( \frac{K'_{i,N}}{x_1^2} + 4 \frac{K'_{i,N} K'_{i,N^+}}{x_1^3} \right),$$

$$\frac{\partial \vec{f_1}}{\partial \vec{x_2}} = -\frac{K'_{i,N_2}}{x_1} - \frac{1}{2} \sqrt{\frac{K'_{d,N_2}}{x_2}} \left( \frac{K'_{i,N}}{x_1} + 2 \frac{K'_{i,N} K'_{i,N^+}}{x_1^2} \right),$$

$$\frac{\partial \vec{f_2}}{\partial \vec{x_1}} = -1 + \frac{1}{\theta} \left[ x_2 \frac{K'_{i,N_2}}{x_1^2} + \sqrt{K'_{d,N_2} x_2} \left( \frac{K'_{i,N}}{x_1^2} + 2 \frac{K'_{i,N} K'_{i,N^+}}{x_1^3} \right) \right],$$

$$\frac{\partial \vec{f_2}}{\partial \vec{x_2}} = -\frac{1}{\theta} \left[ \left( 1 + \frac{K'_{i,N_2}}{x_1} \right) + \frac{1}{2} \sqrt{\frac{K'_{d,N_2}}{x_2}} \left( 1 + \frac{K'_{i,N}}{x_1} + \frac{K'_{i,N} K'_{i,N^+}}{x_1^2} \right) \right].$$

A desired convergence between to consecutive iterations is usually reached after 30 to 40 iterations.

## C.1 Code implementation

For the sake of clarity, the tabulated values required for the calculation of the gas composition are not listed below. They can be found in [69] for both, the calculation of the partition functions for neutral molecules (denoted in the listing with N2n.x, where x stands for different constants) and ionized nitrogen molecules (N2i.x). The total electronic angular momentum quantum number $J$ and the corresponding energy $E$ for atomic nitrogen (denoted below as Nn.x, with x standing for $J$ or $E$), singly ionized atomic nitrogen (Ni.x) and doubly ionized atomic nitrogen (Nii.x) are taken from the NIST atomic database [134]. The data need to be imported prior to calculation. Input data are:

- a row vector containing the electron temperature (TTe)

- the factor theta, denoting the discrepancy between $T_e$ and $T_h$

- a flag (flag_hionN2) with which the mechanism governing the ionization of molecules can be changed. If the flag is set to 1, heavy particles collisions are responsible for molecule ionization. Otherwise, the molecules are ionized due to electron collisions.

The algorithm presented in the previous section is implemented in Scilab.

```
1  // universal constants
2  ee = 1.6022e-19;
3  kB = 1.3807e-23;
4  h  = 6.6261e-34;
5  c  = 2.998e8;
6  me = 9.1094e-31;
7  // atomic & molecular mass of nitrogen
8  mN  = 14.0067*1.6605e-27;
9  mN2 = 2*mN;
10 // gas pressure [Pa]
11 P = 1e5;
12 // for better numerical stability
13 eps = 1e-20;
14 pi  = %pi;
15
16 ///////////////////////////////////////////////////////////////
17 // partition functions for molecules (neutral & once ionized)  //
18 // and atoms (neutral & until twice ionized) for nitrogen plasma //
19 ///////////////////////////////////////////////////////////////
20 function [Z_N2n,Z_N2i,Z_Nn,Z_Ni,Z_Nii,Kd_N2,Ki_N2,Ki_N,Ki_Ni]= ..
```

```
21                                              partitionN2(TTe,theta,flag_hionN2)
22
23 // temperature of heavy gas species
24 invTTe = TTe.^(-1); // as a row vector
25 TTh    = TTe/theta;
26 invTTh = theta*invTTe;
27 // partition functions: diatomic molecules & ionized molecules
28 Z_N2n = zeros(1,length(invTTe));
29 for i=1:length(N2n.Te)
30     deltae = N2n.alphae(i)/(N2n.Be(i)+eps);
31     sigma  = (1-0.5*deltae)*N2n.Be(i)*(h*c*100/kB)*invTTh;
32     u      = (N2n.we(i)-2*N2n.wexe(i))*(h*c*100/kB)*invTTh;
33     gammae = (N2n.Be(i)/N2n.we(i));
34     Z_N2n = Z_N2n + 0.5*N2n.g(i)*exp(-(h*c*100/kB)*N2n.Te(i)*invTTe).* ..
35             ( (sigma.*(1-exp(-u))+eps).^(-1) ).* ..
36             1 + (1/3)*sigma + (1/15)*sigma.^2 + ..
37             8*gammae^2*( sigma.^(-1) ) - ..
38             deltae.*( (1-exp(+u)+eps).^(-1) ) + ..
39             2*N2n.wexe(i)/N2n.we(i).*u.*( (1-exp(+u)+eps).^(-2) ) );
40 end
41 Z_N2i = zeros(1,length(invTTe));
42 for i=1:length(N2i.Te)
43     deltae = N2i.alphae(i)/(N2i.Be(i)+eps);
44     sigma  = (1-0.5*deltae)*N2i.Be(i)*(h*c*100/kB)*invTTh;
45     u      = (N2i.we(i)-2*N2i.wexe(i))*(h*c*100/kB)*invTTh;
46     gammae = (N2i.Be(i)/N2i.we(i));
47     Z_N2i = Z_N2i + 0.5*N2i.g(i)*exp(-(h*c*100/kB)*N2i.Te(i)*invTTe).* ..
48             ( (sigma.*(1-exp(-u))+eps).^(-1) ).* ..
49             ( 1 + (1/3)*sigma + (1/15)*sigma.^2 + ..
50             8*gammae^2*( sigma.^(-1) ) - ..
51             deltae.*( (1-exp(+u)+eps).^(-1) ) + ..
52             2*N2i.wexe(i)/N2i.we(i).*u.*( (1-exp(+u)+eps).^(-2) ) );
53 end
54 // partition functions: atoms & atomic ions
55 Z_Nn  = (2*Nn.J+1)' *exp(-(ee/kB)*Nn.E *invTTe);
56 Z_Ni  = (2*Ni.J+1)' *exp(-(ee/kB)*Ni.E *invTTe);
57 Z_Nii = (2*Nii.J+1)'*exp(-(ee/kB)*Nii.E*invTTe);
58 // Saha factors for dissociation & ionization
59 Kd_N2 = Z_Nn.*Z_Nn./Z_N2n.*((2*pi*(mN^2/mN2)*kB/(h^2)*TTh).^1.5).* ..
60         exp(-(ee/kB)*N2n.Edis*invTTh);
61 if (flag_hionN2==0)
62     // ionization of N2 due to collisions with free electrons
63     Ki_N2 = 2*Z_N2i./Z_N2n.*((2*pi*me*kB/(h^2)*TTe).^1.5).* ..
64             exp(-(ee/kB)*N2n.Eion*invTTe);
65 else
66     // ionization of N2 due to collisions with heavy particles
67     Ki_N2 = 2*Z_N2i./Z_N2n.*((2*pi*me*kB/(h^2)*TTe).^1.5).* ..
68             exp(-(ee/kB)*N2n.Eion*invTTh);
69 end
70 Ki_N  = 2*Z_Ni./Z_Nn.* ((2*pi*me*kB/(h^2)*TTe).^1.5).* ..
71         exp(-(ee/kB)* Nn.Eion*invTTe);
72 Ki_Ni = 2*Z_Nii./Z_Ni.*((2*pi*me*kB/(h^2)*TTe).^1.5).* ..
73         exp(-(ee/kB)* Ni.Eion*invTTe);
74 endfunction
75
76 /////////////////////////////////////////////////////////
77 // calculating gas composition for given Te range & theta //
78 /////////////////////////////////////////////////////////
79 function [nne,nnN2,nnN2i,nnN,nnNi,nnNii,Z_N2n,Z_N2i]= ..
80                                 ionizationN2(TTe,theta,P,flag_hionN2)
81
```

```matlab
82  // calculating partition functions & Saha factors
83  [Z_N2n,Z_N2i,Z_Nn,Z_Ni,Z_Nii,Kd_N2,Ki_N2,Ki_N,Ki_Ni]= ..
84                          partitionN2(TTe,theta,flag_hionN2);
85  // re-scaling Saha factors
86  Kd_N2 = Kd_N2.*(kB*TTe/P);
87  Ki_N2 = Ki_N2.*(kB*TTe/P);
88  Ki_N  = Ki_N .*(kB*TTe/P);
89  Ki_Ni = Ki_Ni.*(kB*TTe/P);
90  // iterative calculation of gas composition (ne, nN2);
91  // notation: x=[ne*(kB*Te/P); nN2*(kB*Te/P)]
92  nne   = zeros(1,length(TTe));
93  nnN2  = zeros(1,length(TTe));
94  nnN2i = zeros(1,length(TTe));
95  nnN   = zeros(1,length(TTe));
96  nnNi  = zeros(1,length(TTe));
97  nnNii = zeros(1,length(TTe));
98  Z_N2n = zeros(1,length(TTe));
99  Z_N2i = zeros(1,length(TTe));
100 xx    = zeros(2,length(TTe));
101 ff    = zeros(2,length(TTe));
102
103 for j=1:length(TTe)
104     // initializing x
105     if (j==1)
106         xx(:,j) = [1e-10; 1];
107     else
108         xx(:,j) = xx(:,j-1);
109     end
110     // iterative solution for x=[ne*(kB*Te/P); nN2*(kB*Te/P)]
111     kappa  = 0.5;
112     ii_max = 50;
113     for ii=1:ii_max
114         x_prov = xx(:,j);
115         // Newton-Raphson method for solving
116         // ff(1)=0 (quasineutrality) & ff(2)=0 (ideal gas equation)
117         ff(1,j) = x_prov(1) - x_prov(2).*Ki_N2(j)./((x_prov(1)+eps)) - ..
118                   sqrt(Kd_N2(j).*x_prov(2)).* ..
119                   ( Ki_N(j)./((x_prov(1)+eps)) + ..
120                   2*Ki_N(j).*Ki_Ni(j)./((x_prov(1)+eps).^2) );
121         ff(2,j) = 1 - x_prov(1) - (1/theta)*( x_prov(2).* ..
122                   (1 + Ki_N2(j)./((x_prov(1)+eps)) ) + ..
123                   sqrt(Kd_N2(j).*x_prov(2)).* ..
124                   ( 1 + Ki_N(j)./((x_prov(1)+eps)) + ..
125                   Ki_N(j).*Ki_Ni(j)./((x_prov(1)+eps).^2) ) );
126         dff = zeros(2,2);
127         dff(1,1) = 1 + x_prov(2).*Ki_N2(j)./((x_prov(1)+eps).^2) + ..
128                    sqrt(Kd_N2(j).*x_prov(2)).* ..
129                    ( Ki_N(j)./((x_prov(1)+eps).^2) + ..
130                    4*Ki_N(j).*Ki_Ni(j)./((x_prov(1)+eps).^3) );
131         dff(1,2) = -Ki_N2(j)./((x_prov(1)+eps)) - ..
132                    0.5*sqrt(Kd_N2(j)./(x_prov(2)+eps)).* ..
133                    ( Ki_N(j)./((x_prov(1)+eps)) + ..
134                    2*Ki_N(j).*Ki_Ni(j)./((x_prov(1)+eps).^2) );
135         dff(2,1) = -1 + (1/theta)*( x_prov(2).* ..
136                    (0 + Ki_N2(j)./((x_prov(1)+eps).^2) ) + ..
137                    sqrt(Kd_N2(j).*x_prov(2)).* ..
138                    ( 0 + Ki_N(j)./((x_prov(1)+eps).^2) + ..
139                    2*Ki_N(j).*Ki_Ni(j)./((x_prov(1)+eps).^3) ) );
140         dff(2,2) = -(1/theta)*( (1 + Ki_N2(j)./((x_prov(1)+eps)) ) + ..
141                    0.5*sqrt(Kd_N2(j)./(x_prov(2)+eps)).* ..
142                    ( 1 + Ki_N(j)./((x_prov(1)+eps)) + ..
```

```scilab
143                          Ki_N(j).*Ki_Ni(j)./((x_prov(1)+eps).^2) ) );
144             // improved solution
145             xx(:,j) = x_prov - kappa*( dff\ff(:,j) );
146         end
147         // normalized particle densities
148         nne(j)   = xx(1,j);
149         nnN2(j)  = xx(2,j);
150         nnN(j)   = sqrt(nnN2(j).*Kd_N2(j));
151         nnN2i(j) = nnN2(j).*Ki_N2(j)./nne(j);
152         nnNi(j)  = nnN(j).*Ki_N(j)./nne(j);
153         nnNii(j) = nnNi(j).*Ki_Ni(j)./nne(j);
154 end
155 // re-scaling particle densities back to [m^-3]
156 nne   = nne  *(P/kB)./TTe;
157 nnN2  = nnN2 *(P/kB)./TTe;
158 nnN2i = nnN2i*(P/kB)./TTe;
159 nnN   = nnN  *(P/kB)./TTe;
160 nnNi  = nnNi *(P/kB)./TTe;
161 nnNii = nnNii*(P/kB)./TTe;
162 endfunction
163
164 ////////////////
165 // MAIN CODE //
166 ////////////////
167
168 Te_min = 3000;                  // electron temperature range [K]
169 Te_max = 35000;
170 DTe    = 1000;                  // step
171 TTe    = Te_min:DTe:Te_max;     // as a row vector
172 theta = 1;                      // theta factor: theta=Te/Th
173 // ionization of N2 molecules either due to collisions
174 // with heavy particles (flag=1) or with electrons (flag=0)
175 flag_hionN2 = 1;
176 flag_hionN2 = evstr(x_dialog('ionization of N2 due to heavy (=1) or electrons
        (=0):',string(flag_hionN2)));
177 // N2 ionization for different theta values
178 ttheta = [1,3,5,10,15];
179 nne   = zeros(length(ttheta),length(TTe));
180 nnN2  = zeros(length(ttheta),length(TTe));
181 nnN2i = zeros(length(ttheta),length(TTe));
182 nnN   = zeros(length(ttheta),length(TTe));
183 nnNi  = zeros(length(ttheta),length(TTe));
184 nnNii = zeros(length(ttheta),length(TTe));
185 Z_N2n = zeros(length(ttheta),length(TTe));
186 Z_N2i = zeros(length(ttheta),length(TTe));
187 for k=1:length(ttheta)
188     theta = ttheta(k);
189     [nne_aux,nnN2_aux,nnN2i_aux,nnN_aux, ..
190      nnNi_aux,nnNii_aux,Z_N2n_aux,Z_N2i_aux] = ..
191                             ionizationN2(TTe,theta,P,flag_hionN2);
192     nne(k,:)   = nne_aux;
193     nnN2(k,:)  = nnN2_aux;
194     nnN2i(k,:) = nnN2i_aux;
195     nnN(k,:)   = nnN_aux;
196     nnNi(k,:)  = nnNi_aux;
197     nnNii(k,:) = nnNii_aux;
198 end
```

# D

## CALCULATION OF THE EMISSION SPECTRUM OF THE $C^3\Pi_u \rightarrow B^3\Pi_g$ TRANSITION

The theoretical principles how to calculate a molecular emission spectrum with tabulated data are discussed in sections 2.2.4 and 2.2.5. Here a more practical approach for just one transition, the so called second positive system, the $C^3\Pi_u \rightarrow B^3\Pi_g$ of molecular nitrogen is presented. The calculations are based on works of Herzberg [63], to which it should be referred to for further details.

The second positive system, a transition from the $C^3\Pi_u$ energy level to the $B^3\Pi_g$ level of a nitrogen molecule contains all line branches ($P$, $Q$, $R$) according to the selection rules $\Delta J = 0, \pm 1$. Nonetheless, this is also a triplet transition hence it contains sub-branches. The spectrum then consists of 3 $P$-, 3 $R$- and 2 $Q$-branches. The $Q$-branches are weak and their intensity decreases rapidly with increasing rotational quantum number $J$, thus one of the $Q$-sub-branches can be neglected for the second positive system. The rotational energy term values for a triplet state can be calculated as follows

$$
\begin{aligned}
F_1(J) &= B_v \left( J(J+1) - \sqrt{Z_1(J)} - 2Z_2(J) \right) - D_v \left( J - \frac{1}{2} \right)^4 , \\[2mm]
F_2(J) &= B_v \left( J(J+1) + 4Z_2(J) \right) - D_v \left( J + \frac{1}{2} \right)^4 , \\[2mm]
F_3(J) &= B_v \left( J(J+1) + \sqrt{Z_1(J)} - 2Z_2(J) \right) - D_v \left( J + \frac{3}{2} \right)^4 ,
\end{aligned}
\tag{D.1}
$$

$$
\text{with} \quad Z_1(J) = Y(Y-4) + \frac{4}{3} + 4J(J+1)
$$

$$
\text{and} \quad Z_2(J) = \frac{1}{3Z_1(J)} \left( Y(Y-1) - \frac{4}{9} - 2J(J+1) \right) .
$$

The constant $Y$ in the above equations couples the spin momentum vector to the internuclear axis and can be found in [69]. To keep the nomenclature consistent with section 2.2.4, the initial level $C^3\Pi_u$ is designated by the index $i$ in the following and the final state $B^3\Pi_g$ of the transition by the index $f$. Thereafter, according to [63] the constant $Y$ for the $i \rightarrow f$ transition is given by

$$
\begin{aligned}
Y_i &= \frac{A_i}{B_{v,i}} \quad \text{with} \quad A_i = 42.24 , \\[2mm]
Y_f &= \frac{A_f}{B_{v,f}} \quad \text{with} \quad A_f = 39.20 .
\end{aligned}
$$

Additionally, let index $t$ denote the triplet sub-branches for better clarity. As the vibrational energy $E_v$ is calculated according to equation (2.77), the wavelength sets for each branch of the second positive system are given in nanometers by:

$$\text{P-branch:} \quad \lambda_{P,t} = 10^7 \left[ (E_{v,i} - E_{v,f}) + (F_{i,P,t}(J) - F_{f,P,t}(J-1)) \right]^{-1} \quad \text{with} \quad t = 1, 2, 3,$$

$$\text{R-branch:} \quad \lambda_{R,t} = 10^7 \left[ (E_{v,i} - E_{v,f}) + (F_{i,R,t}(J) - F_{f,R,t}(J-1)) \right]^{-1} \quad \text{with} \quad t = 1, 2, 3, \quad \text{(D.2)}$$

$$\text{Q-branch:} \quad \lambda_{Q,t} = 10^7 \left[ (E_{v,i} - E_{v,f}) + (F_{i,Q,t}(J) - F_{f,Q,t}(J-1)) \right]^{-1} \quad \text{with} \quad t = 2, 3.$$

Assuming a Maxwell-Boltzmann distribution of particles in each energy level, for the rotational line intensities can be written:

$$\text{P-branch:} \quad E_{rot,P,t} = \frac{J(J+2)}{(J+1)} e^{-\frac{q_e F_{i,P,t}}{k_B T_{rot}}} \quad \text{with} \quad t = 1, 2, 3,$$

$$\text{R-branch:} \quad E_{rot,R,t} = \frac{(J+1)(J-1)}{J} e^{-\frac{q_e F_{i,R,t}}{k_B T_{rot}}} \quad \text{with} \quad t = 1, 2, 3, \quad \text{(D.3)}$$

$$\text{Q-branch:} \quad E_{rot,Q,t} = \frac{(2J+1)}{J(J+1)} e^{-\frac{q_e F_{i,Q,t}}{k_B T_{rot}}} \quad \text{with} \quad t = 2, 3.$$

Assuming that the transfer function of the experimental setup has a Gaussian shape, the line intensities for each branch and sub-branch are convoluted with an according Gaussian profile. To increase the computation speed, an approximated solution is used where for the first sub-branch the minimal possible $J = 0$, for the second sub-branch $J = 1$ and for third $J = 2$. The intensity of each branch is given by

$$\text{P-branch:} \quad I_P = \sum_t E_{rot,P,t} \, e^{-\left(4\ln(2)\left(\frac{\lambda - \lambda_{P,t}}{\Delta\lambda_{app}}\right)^2\right)},$$

$$\text{R-branch:} \quad I_R = \sum_t E_{rot,R,t} \, e^{-\left(4\ln(2)\left(\frac{\lambda - \lambda_{R,t}}{\Delta\lambda_{app}}\right)^2\right)}, \quad \text{(D.4)}$$

$$\text{Q-branch:} \quad I_Q = \sum_t E_{rot,Q,t} \, e^{-\left(4\ln(2)\left(\frac{\lambda - \lambda_{Q,t}}{\Delta\lambda_{app}}\right)^2\right)}.$$

Thereafter, the total intensity of the rotational lines is a sum of equal to

$$I_{rot} = I_P + I_R + I_Q. \quad \text{(D.5)}$$

Depending on the vibrational quantum number $v$, the total line intensity according to eq. 2.82 is proportional to

$$I_{tot} \approx \sum_v n_{N_2} \frac{1}{\lambda_{if}^4} I_{rot} \, S_{v,if} \, e^{-\frac{E_{v,i} - E_{v,f}}{k_B T_{vib}}}, \quad \text{(D.6)}$$

where $S_{v,if}$ is the Franck-Condon coefficient and $\lambda_{if}$ the corresponding wavelength of each specific transition. Both, $S_{v,if}$ and $\lambda_{if}$ are tabulated and can be found in [110]. As can be seen from the above, the density of nitrogen molecules $n_{N_2}$ as well as the temperatures $T_{rot}$ and $T_{vib}$ are needed to compute the intensity. Assuming that $T_{rot} = T_{vib} = T_h$, these values are obtained from the calculation presented in Appendix C.

## D.1 Code implementation

The listing presented in this section shows a "quick & dirty" implementation of the above equations into a computing software, which is Scilab again. Before calculation of the spectrum, the plasma

composition needs to be computed. Then, the tabulated data for both energy levels, $C^3\Pi_u$ and $B^3\Pi_g$, as well as the Franck-Condon factors with corresponding wavelengths need to be imported. These values can be found in literature and hence are not listed below [69, 110, 137]. Additional input variables, which significantly influence the computation time, are the wavelength range for which the spectrum should be calculated (denoted with `in_lambda_hi` and `in_lambda_low`), the wavelength increment (`in_step`) and the FWHM of the apparatus profile (`in_apparatus`).

```
1  // universal constants
2  ee = 1.6022e-19;
3  kB = 1.3807e-23;
4  // wavelength range & step between points in [nm]
5  in_lambda_hi = 400;
6  in_lambda_low = 280;
7  in_step = 0.025;
8  // FWHM of the apparatus
9  in_apparatus = 0.065;
10
11 /////////////////////////////////////////////////
12 // spectrum calculation of the SPS-system of N2 //
13 /////////////////////////////////////////////////
14 function SPS = SPS_spectrum(Tvib, Trot, N2n, ..
15                            in_lambda_hi, in_lambda_low, ..
16                            in_step, in_apparatus)
17
18 J = 1:100;       // rotational quantum number
19 m = 1;
20 k = 1;
21 // load molecular constants from Herzberg
22 moldat_up = molecular_data(4,:);   // C3Pi-u state
23 moldat_down = molecular_data(3,:); // B3Pi-g state
24 // uncoupling of spin momentum vector - Herzberg pp. 418-419 [cm^(-1)]
25 A_up = 39.2;
26 A_down = 42.24;
27 F_up = [];
28 F_down = [];
29 for nu_up=1:size(SPS.FC)(1,1)         // nu'
30     Evib_up = (moldat_up(1) + ..
31              moldat_up(2).*(nu_up-1+0.5) - ..
32              moldat_up(3).*(nu_up-1+0.5)^2 + ..
33              moldat_up(4).*(nu_up-1+0.5)^3);     // in [cm^(-1)]
34     Bv_up = moldat_up(5) - moldat_up(6).*(nu_up-1+0.5);
35     Dv_up = moldat_up(7) + moldat_up(8).*(nu_up-1+0.5);
36     Y_up = A_up/Bv_up;                           // in [cm^(-1)]
37     for nu_down=1:size(SPS.FC)(1,2)   // nu"
38         Evib_down = (moldat_down(1) + ..
39                    moldat_down(2).*(nu_down-1+0.5) - ..
40                    moldat_down(3).*(nu_down-1+0.5)^2 + ..
41                    moldat_down(4).*(nu_down-1+0.5)^3);
42         Bv_down = moldat_down(5) - moldat_down(6).*(nu_down-1+0.5);
43         Dv_down = moldat_down(7) + moldat_down(8).*(nu_down-1+0.5);
44         Y_down = A_down/Bv_down;
45         // sqrtZ1 & Z2 are unitless
46         sqrtZ1 = (Y_up.*(Y_up - 4) + 4/3 + 4.*J.*(J+1)).^0.5;
47         Z2 = (1./(3.*sqrtZ1^2)) .* ..
48             (Y_up.*(Y_up - 1) - 4/9 - 2.*J.*(J+1));
49         F_up(:,1) = Bv_up.*(J.*(J+1) - (sqrtZ1) - 2.*Z2) - ..
50                   moldat_up(7).*(J - 0.5).^4;
51         F_up(:,2) = Bv_up.*(J.*(J+1) + 4.*Z2) - ..
52                   moldat_up(7).*(J + 0.5).^4;
53         F_up(:,3) = Bv_up.*(J.*(J+1) - (sqrtZ1) - 2.*Z2) - ..
```

```matlab
54                     moldat_up (7) .*( J + 1.5) .^4;
55         // Q-branch
56         sqrtZ1 = (Y_down.*(Y_down - 4) + 4/3 + 4.*J.*(J+1)).^0.5;
57         Z2 = (1./(3.*sqrtZ1^2)) .* ..
58             (Y_down.*(Y_down - 1) - 4/9 - 2.*J.*(J+1));
59         F_downQ(:,1) = Bv_down.*(J.*(J+1) - (sqrtZ1) - 2.*Z2) - ..
60                     moldat_down (7) .*( J - 0.5) .^4;
61         F_downQ(:,2) = Bv_down.*(J.*(J+1) + 4.*Z2) - ..
62                     moldat_down (7) .*( J + 0.5) .^4;
63         F_downQ(:,3) = Bv_down.*(J.*(J+1) - (sqrtZ1) - 2.*Z2) - ..
64                     moldat_down (7) .*( J + 1.5) .^4;
65         // P-branch
66         sqrtZ1 = (Y_down.*(Y_down - 4) + 4/3 + 4.*(J+1).*(J+2)).^0.5;
67         Z2 = (1./(3.*sqrtZ1^2)) .* ..
68             (Y_down.*(Y_down - 1) - 4/9 - 2.*(J+1).*(J+2));
69         F_downP (:,1) = Bv_down.*((J+1).*(J+2) - (sqrtZ1) - 2.*Z2) - ..
70                     moldat_down (7) .*( J + 0.5) .^4;
71         F_downP (:,2) = Bv_down.*((J+1).*(J+2) + 4.*Z2) - ..
72                     moldat_down (7) .*( J + 1.5) .^4;
73         F_downP (:,3) = Bv_down.*((J+1).*(J+2) - (sqrtZ1) - 2.*Z2) - ..
74                     moldat_down (7) .*( J + 2.5) .^4;
75         // R-branch
76         sqrtZ1 = (Y_down.*(Y_down - 4) + 4/3 + 4.*(J-1).*(J)).^0.5;
77         Z2 = (1./(3.*sqrtZ1^2)) .* ..
78             (Y_down.*(Y_down - 1) - 4/9 - 2.*(J-1).*(J));
79         F_downR (:,1) = Bv_down.*((J-1).*(J) - (sqrtZ1) - 2.*Z2) - ..
80                     moldat_down (7) .*( J - 1.5) .^4;
81         F_downR (:,2) = Bv_down.*((J-1).*(J) + 4.*Z2) - ..
82                     moldat_down (7) .*( J - 0.5) .^4;
83         F_downR (:,3) = Bv_down.*((J-1).*(J) - (sqrtZ1) - 2.*Z2) - ..
84                     moldat_down (7) .*( J + 0.5) .^4;
85
86         intens = [];
87         lambda = [];
88         // line intensity Q-branch
89         intens(:,1,1) = J-J;
90         intens(:,1,2) = ((2.*J+1)./(J.*(J+1))).* ..
91                         exp(-F_up(:,2)'.*ee./(Trot.*kB));
92         intens(:,1,3) = ((2.*J+1)./(J.*(J+1))).* ..
93                         exp(-F_up(:,3)'.*ee./(Trot.*kB));
94         // line intensity P-branch
95         intens(:,2,1) = ((J+2).*J./(J+1)).* ..
96                         exp(-F_up(:,1)'.*ee./(Trot.*kB));
97         intens(:,2,2) = ((J+2).*J./(J+1)).* ..
98                         exp(-F_up(:,2)'.*ee./(Trot.*kB));
99         intens(:,2,3) = ((J+2).*J./(J+1)).* ..
100                        exp(-F_up(:,3)'.*ee./(Trot.*kB));
101        // line intensity R-branch
102        intens(:,3,1) = ((J+1).*(J-1)./J).* ..
103                        exp(-F_up(:,1)'.*ee./(Trot.*kB));
104        intens(:,3,2) = ((J+1).*(J-1)./J).* ..
105                        exp(-F_up(:,2)'.*ee./(Trot.*kB));
106        intens(:,3,3) = ((J+1).*(J-1)./J).* ..
107                        exp(-F_up(:,3)'.*ee./(Trot.*kB));
108
109        while (m <= (max(J)-1))
110            // wavelength Q-branch in [nm]
111            lambda(m,1,1) = 0;
112            lambda(m,1,2) = 1D7/((Evib_up - Evib_down) + ..
113                            F_up(m,2) - F_downQ(m,2));
114            lambda(m,1,3) = 1D7/((Evib_up - Evib_down) + ..
```

```
115                                                 F_up(m,3) - F_downQ(m,3));
116                  // wavelength P-branch in [nm]
117                  lambda(m,2,1) = 1D7/((Evib_up - Evib_down) + ..
118                                       F_up(m,1) - F_downP(m+1,1));
119                  lambda(m,2,2) = 1D7/((Evib_up - Evib_down) + ..
120                                       F_up(m,2) - F_downP(m+1,2));
121                  lambda(m,2,3) = 1D7/((Evib_up - Evib_down) + ..
122                                       F_up(m,3) - F_downP(m+1,3));
123                  // wavelength R-branch in [nm]
124                  if (m == 1) then
125                      lambda(m,3,1) = 1D7/((Evib_up - Evib_down) + ..
126                                           0        - 0);
127                      lambda(m,3,2) = 1D7/((Evib_up - Evib_down) + ..
128                                           0        - 0);
129                      lambda(m,3,3) = 1D7/((Evib_up - Evib_down) + ..
130                                           0        - 0);
131                  else
132                      lambda(m,3,1) = 1D7/((Evib_up - Evib_down) + ..
133                                           F_up(m,1) - F_downR(m-1,1));
134                      lambda(m,3,2) = 1D7/((Evib_up - Evib_down) + ..
135                                           F_up(m,2) - F_downR(m-1,2));
136                      lambda(m,3,3) = 1D7/((Evib_up - Evib_down) + ..
137                                           F_up(m,3) - F_downR(m-1,3));
138                  end
139                  m = m + 1;
140              end
141              m = 1;
142
143              // convolution with apparatus profile
144              var_lambda = in_lambda_low:in_step:in_lambda_hi;
145              for a=1:length(var_lambda)
146                  // Q-branch
147                  tmp1 = intens(:,1,1)(1:size(lambda(:,1,1))(1,1)).* ..
148                          exp(-4.*log(2).*((var_lambda'(a)- ..
149                          lambda(:,1,1)(1:size(lambda(:,1,1))(1,1))).^2)./ ..
150                          (in_apparatus.^2));
151                  tmp2 = intens(:,1,2)(2:size(lambda(:,1,2))(1,1)).* ..
152                          exp(-4.*log(2).*((var_lambda'(a)- ..
153                          lambda(:,1,2)(2:size(lambda(:,1,1))(1,1))).^2)./ ..
154                          (in_apparatus.^2));
155                  tmp3 = intens(:,1,3)(3:size(lambda(:,1,3))(1,1)).* ..
156                          exp(-4.*log(2).*((var_lambda'(a)- ..
157                          lambda(:,1,3)(3:size(lambda(:,1,1))(1,1))).^2)./ ..
158                          (in_apparatus.^2));
159                  tmp(1) = tmp1(1);
160                  tmp(2) = tmp1(2) + tmp2(1);
161                  tmp(3:size(tmp1)(1,1)) = tmp1(:)(3:size(tmp1)(1,1)) + ..
162                                           tmp2(:)(2:size(tmp2)(1,1)) + ..
163                                           tmp3(:)(1:size(tmp3)(1,1));
164                  roto.Q(a) = sum(tmp);
165                  tmp = []; tmp1 = []; tmp2 = []; tmp3 = [];
166                  // P-branch
167                  tmp1 = intens(:,2,1)(1:size(lambda(:,2,1))(1,1)).* ..
168                          exp(-4.*log(2).*((var_lambda'(a)- ..
169                          lambda(:,2,1)(1:size(lambda(:,2,1))(1,1))).^2)./ ..
170                          (in_apparatus.^2));
171                  tmp2 = intens(:,2,2)(2:size(lambda(:,2,2))(1,1)).* ..
172                          exp(-4.*log(2).*((var_lambda'(a)- ..
173                          lambda(:,2,2)(2:size(lambda(:,2,2))(1,1))).^2)./ ..
174                          (in_apparatus.^2));
175                  tmp3 = intens(:,2,3)(3:size(lambda(:,2,3))(1,1)).* ..
```

D

```scilab
176                         exp (-4.*log(2).*((var_lambda'(a)- ..
177                         lambda(:,2,3)(3:size(lambda(:,2,3))(1,1))).^2)./ ..
178                         (in_apparatus.^2));
179                 tmp(1) = tmp1(1);
180                 tmp(2) = tmp1(2) + tmp2(1);
181                 tmp(3:size(tmp1)(1,1)) = tmp1(:)(3:size(tmp1)(1,1)) + ..
182                                          tmp2(:)(2:size(tmp2)(1,1)) + ..
183                                          tmp3(:)(1:size(tmp3)(1,1));
184                 roto.P(a) = sum(tmp);
185                 tmp = []; tmp1 = []; tmp2 = []; tmp3 = [];
186                 // R-branch
187                 tmp1 = intens(:,3,1)(1:size(lambda(:,3,1))(1,1)).* ..
188                         exp (-4.*log(2).*((var_lambda'(a)- ..
189                         lambda(:,3,1)(1:size(lambda(:,3,1))(1,1))).^2)./ ..
190                         (in_apparatus.^2))
191                 tmp2 = intens(:,3,2)(2:size(lambda(:,3,2))(1,1)).* ..
192                         exp (-4.*log(2).*((var_lambda'(a)- ..
193                         lambda(:,3,2)(2:size(lambda(:,3,1))(1,1))).^2)./ ..
194                         (in_apparatus.^2))
195                 tmp3 = intens(:,3,3)(3:size(lambda(:,3,3))(1,1)).* ..
196                         exp (-4.*log(2).*((var_lambda'(a)- ..
197                         lambda(:,3,3)(3:size(lambda(:,3,1))(1,1))).^2)./ ..
198                         (in_apparatus.^2));
199                 tmp(1) = tmp1(1);
200                 tmp(2) = tmp1(2) + tmp2(1);
201                 tmp(3:size(tmp1)(1,1)) = tmp1(:)(3:size(tmp1)(1,1)) + ..
202                                          tmp2(:)(2:size(tmp2)(1,1)) + ..
203                                          tmp3(:)(1:size(tmp3)(1,1));
204                 roto.R(a) = sum(tmp);
205                 tmp = []; tmp1 = []; tmp2 = []; tmp3 = [];
206             end
207             roto.lambda = var_lambda';
208             tmp = roto.Q + roto.P + roto.R;
209             // intnsity calculation for each rotational state
210             if (SPS.lambda(nu_up,nu_down) <> 0) & ..
211                (SPS.FC(nu_up,nu_down) <> 0) then
212                 tmp = N2n.*((SPS.lambda(nu_up,nu_down)).^(-4)).* ..
213                       tmp.*SPS.FC(nu_up,nu_down).* ..
214                       exp(-ee.*(Evib_up - moldat_up(1))./(kB.*Tvib));
215             else
216                 tmp = 0;
217             end
218             roto.tmp(nu_up, nu_down, :) = tmp;
219             roto.raw_intens(nu_up, nu_down, :) = tmp;
220             tmp = []; clear roto.Q; clear roto.P; clear roto.R;
221         end             // end of nu_down loop
222     // intensity calculation for each vibrational state
223     for i=1:size(roto.raw_intens)(1,3)
224         roto.tmp(nu_up, i) = sum(roto.raw_intens(nu_up, :, i));
225     end
226 end             // end of nu_up loop
227 //// total intensity calculation
228 for i=1:size(roto.raw_intens)(1,3)
229     roto.intens(i) = sum(roto.tmp(:,i));
230 end
231 SPS = roto;
232 clear roto.tmp;
233 endfunction
```

# E

# REVERSE LAPLACE TRANSFORMATION OF A SQUARE FUNCTION

As proposed in section 5.3.3, the response of the electron number density $n_e$ to a change in current can be approximated with a proportional element with time delay. Thereafter, the following can be written for the electron density in the frequency domain

$$\hat{n}_e(s) \approx \frac{V}{1 + \tau s} \hat{i}(s)$$

with the current $\hat{i}(s)$ given by

$$\hat{i}(s) = a_0 \frac{1}{s} + \sum_{k=1}^{\infty} \left[ a_k \frac{s}{s^2 + \left(\frac{2\pi k}{T}\right)^2} + b_k \frac{\frac{2\pi k}{T}}{s^2 + \left(\frac{2\pi k}{T}\right)^2} \right] .$$

To transform the response back into the time domain, an inverse Laplace transform of $\hat{n}_e(s)$ has to be calculated. Unfortunately, there is no straight forward method to do this. Therefore, the formula is split into partial fractions of which the inverse Laplace transform is known. Thus for the first part of the approximation function can be written

$$\hat{n}_{e,1}(s) \approx \frac{V}{1 + \tau s} \left[ a_0 \frac{1}{s} \right] = V a_0 \left[ \frac{1}{\tau} \frac{1}{s + \frac{1}{\tau}} \frac{1}{s} \right] = V a_0 \left[ \frac{\left(s + \frac{1}{\tau}\right) - s}{s \left(s + \frac{1}{\tau}\right)} \right] = V a_0 \left[ \frac{1}{s} - \frac{1}{s + \frac{1}{\tau}} \right] .$$

Thereafter, the inverse transform of the first part is given by

$$\mathcal{L}^{-1} \left\{ \hat{n}_{e,1}(s) \right\} \approx \mathcal{L}^{-1} \left\{ V a_0 \left[ \frac{1}{s} - \frac{1}{s + \frac{1}{\tau}} \right] \right\} = V a_0 \left( 1 - e^{-t/\tau} \right) . \tag{E.1}$$

The second part of the approximation function can be transformed into the time domain by the following steps

$$\frac{1}{\tau}\frac{1}{s+\frac{s}{\tau}}\frac{s}{s^2+\Omega^2} = \frac{\frac{s}{\tau}}{\left(s+\frac{1}{\tau}\right)\left(s^2+\Omega^2\right)}\frac{1+\Omega^2\tau^2}{1+\Omega^2\tau^2} = \frac{1}{1+\Omega^2\tau^2}\left[\frac{s\left(\Omega^2\tau+\frac{1}{\tau}\right)}{\left(s+\frac{1}{\tau}\right)\left(s^2+\Omega^2\right)}\right]$$

$$= \frac{1}{1+\Omega^2\tau^2}\left[\frac{-\left(s^2+\Omega^2\right)+\left(s+\frac{1}{\tau}\right)\left(s+\Omega^2\tau\right)}{\left(s+\frac{1}{\tau}\right)\left(s^2+\Omega^2\right)}\right] = \frac{1}{1+\Omega^2\tau^2}\left[\frac{-1}{\left(s+\frac{1}{\tau}\right)}+\frac{\left(s+\Omega^2\tau\right)}{\left(s^2+\Omega^2\right)}\right]$$

$$= \frac{1}{1+\Omega^2\tau^2}\left[-\frac{1}{\left(s+\frac{1}{\tau}\right)}+\frac{s}{\left(s^2+\Omega^2\right)}+\frac{\Omega^2\tau}{\left(s^2+\Omega^2\right)}\right]$$

$$= -\frac{1}{1+\Omega^2\tau^2}\frac{1}{s+\frac{1}{\tau}}+\frac{1}{\sqrt{1+\Omega^2\tau^2}}\left[\frac{1}{\sqrt{1+\Omega^2\tau^2}}\frac{s}{s^2+\Omega^2}+\frac{1}{\sqrt{1+\Omega^2\tau^2}}\frac{\Omega}{s^2+\Omega^2}\right].$$

(E.2)

The above equation (E.2) can be transformed using the following trigonometric addition theorem $\cos\left(\alpha\pm\beta\right) = \cos\alpha\cos\beta\pm\sin\alpha\sin\beta$, according to

$$f(t) = a\cos(\omega t)+b\sin(\omega t) = \sqrt{a^2+b^2}\left(\frac{a}{\sqrt{a^2+b^2}}\cos(\omega t)+\frac{b}{\sqrt{a^2+b^2}}\sin(\omega t)\right).$$

Since $\left(\dfrac{a}{\sqrt{a^2+b^2}}\right)^2+\left(\dfrac{b}{\sqrt{a^2+b^2}}\right)^2 = 1$ and thus $(\cos\varphi)^2+(\sin\varphi)^2 = 1$, it can be written

$$f(t) = \sqrt{a^2+b^2}\left(\cos\varphi\cos(\omega t)+\sin\varphi\sin(\omega t)\right) = \sqrt{a^2+b^2}\cos\left(\omega t+\varphi\right).$$

Hence, the equation (E.2) can be rewriten to

$$\frac{1}{\tau}\frac{1}{s+\frac{s}{\tau}}\frac{s}{s^2+\Omega^2} = -\frac{1}{1+\Omega^2\tau^2}\frac{1}{s+\frac{1}{\tau}}+\frac{1}{\sqrt{1+\Omega^2\tau^2}}\left[\cos\varphi\frac{s}{s^2+\Omega^2}+\sin\varphi\frac{\Omega}{s^2+\Omega^2}\right]$$

with $\cos\varphi = \dfrac{1}{\sqrt{1+\Omega^2\tau^2}}$, $\sin\varphi = \dfrac{\Omega\tau}{\sqrt{1+\Omega^2\tau^2}}$ and $\varphi = \arctan\left(\Omega\tau\right)$. Thereafter,

$$\mathcal{L}^{-1}\left\{\hat{n}_{e,2}(s)\right\} \approx \mathcal{L}^{-1}\left\{\frac{V}{1+\tau s}\sum_{k=1}^{\infty}\left[a_k\frac{s}{s^2+\left(\frac{2\pi k}{T}\right)^2}\right]\right\}$$

$$\approx \mathcal{L}^{-1}\left\{V\sum_{k=1}^{\infty}\left[-\frac{a_k}{1+\left(\frac{2\pi k\tau}{T}\right)^2}\frac{1}{s+\frac{1}{\tau}}+\frac{a_k}{\sqrt{1+\left(\frac{2\pi k\tau}{T}\right)^2}}\left(+\cos\varphi\frac{s}{s^2+\Omega^2}+\sin\varphi\frac{\Omega}{s^2+\Omega^2}\right)\right]\right\}$$

$$= V\sum_{k=1}^{\infty}\left[\frac{-a_k}{1+\left(\frac{2\pi k\tau}{T}\right)^2}e^{-t/\tau}+\frac{a_k}{\sqrt{1+\left(\frac{2\pi k\tau}{T}\right)^2}}\cos\left(\frac{2\pi k}{T}t-\arctan\left(\frac{2\pi k\tau}{T}\right)\right)\right].$$

(E.3)

Analogously to equation (E.2), the third part of the function is transformed to

$$
\frac{1}{\tau} \frac{1}{s + \frac{1}{\tau}} \frac{\Omega}{s^2 + \Omega^2} = \frac{1}{1 + \Omega^2 \tau^2} \left( + \frac{\Omega \tau}{s + \frac{1}{\tau}} - \frac{\Omega \tau s}{s^2 + \Omega^2} + \frac{\Omega}{s^2 + \Omega^2} \right)
$$

$$
= + \frac{\Omega \tau}{1 + \Omega^2 \tau^2} \frac{1}{s + \frac{1}{\tau}} + \frac{1}{\sqrt{1 + \Omega^2 \tau^2}} \left( - \sin \varphi \frac{s}{s^2 + \Omega^2} + \cos \varphi \frac{\Omega}{s^2 + \Omega^2} \right) ,
$$

prior to the inverse Laplace transform which is given by

$$
\mathcal{L}^{-1} \left\{ \hat{n}_{e,3}(s) \right\} \approx \mathcal{L}^{-1} \left\{ \frac{V}{1 + \tau s} \sum_{k=1}^{\infty} \left[ b_k \frac{\frac{2\pi k}{T}}{s^2 + \left( \frac{2\pi k}{T} \right)^2} \right] \right\}
$$

$$
= V \sum_{k=1}^{\infty} \left[ \frac{b_k \frac{2\pi k \tau}{T}}{1 + \left( \frac{2\pi k \tau}{T} \right)^2} e^{-t/\tau} + \frac{b_k}{\sqrt{1 + \left( \frac{2\pi k \tau}{T} \right)^2}} \sin \left( \frac{2\pi k}{T} t - \arctan \left( \frac{2\pi k \tau}{T} \right) \right) \right] . \quad \text{(E.4)}
$$

Finally, the response of the electron number density to a current change in the time domain is given by

$$
n_e(t) \approx V a_0 \left( 1 - e^{-t/\tau} \right) + V \sum_{k=1}^{\infty} \frac{\left( -a_k + b_k \frac{2\pi k \tau}{T} \right)}{1 + \left( \frac{2\pi k \tau}{T} \right)^2} e^{-t/\tau}
$$

$$
+ V \sum_{k=1}^{\infty} \left[ \frac{a_k}{\sqrt{1 + \left( \frac{2\pi k \tau}{T} \right)^2}} \cos \left( \frac{2\pi k}{T} t - \arctan \left( \frac{2\pi k \tau}{T} \right) \right) \right.
$$

$$
\left. + \frac{b_k}{\sqrt{1 + \left( \frac{2\pi k \tau}{T} \right)^2}} \sin \left( \frac{2\pi k}{T} t - \arctan \left( \frac{2\pi k \tau}{T} \right) \right) \right] . \quad \text{(E.5)}
$$

# Bibliography

## References

[1] F. Afshar. *Electronic drive for low wattage metal halide lamps focused on acoustic resonances in HID lamps*. PhD thesis, Technische Universität Berlin, 2007.

[2] F. Afshar. The theory of acoustic resonance and acoustic instability in HID lamps. *LEUKOS*, 5(1), 2008. URL: https://doi.org/10.1080/15502724.2008.10747627.

[3] C. A. Aggelopoulos. Recent advances of cold plasma technology for water and soil remediation: A critical review. *Chem. Eng. J.*, 428:131657, 2022. URL: https://doi.org/10.1016/j.cej.2021.131657.

[4] Y. Akishev, M. Grushin, V. Karalnik, A. Petryakov, and N. Trushkin. Non-equilibrium constricted dc glow discharge in $N_2$ flow at atmospheric pressure: stable and unstable regimes. *J. Phys. D: Appl. Phys.*, 43(7):075202, 2010. URL: https://doi.org/10.1088/0022-3727/43/7/075202.

[5] Y. Akishev, M. Grushin, V. Karalnik, A. Petryakov, and N. Trushkin. On basic processes sustaining constricted glow discharge in longitudinal $N_2$ flow at atmospheric pressure. *J. Phys. D: Appl. Phys.*, 43(21):215202, 2010. URL: https://doi.org/10.1088/0022-3727/43/21/215202.

[6] ams-OSRAM AG. *AS7265x - Smart 18-channel VIS to NIR spectral ID 3-sensor chipset with electronic shutter (data sheet)*, July 2018.

[7] A. Atzberger, G. Huismann, M. Szulc, S. Kirner, S. Zimmermann, G. Forster, and J. Schein. Pulsed current investigations and effects of the wire arc spraying process. In *International Thermal Spray Conference ITSC2016: Lectures & Posters of the Conference in Shanghai*, volume 324 of *DVS-Berichte*. DVS Media GmbH, May 2016.

[8] M. Baeva. Thermal and chemical nonequilibrium effects in free-burning arcs. *Plasma Chem. Plasma Process.*, 36:151–167, 2016. URL: https://doi.org/10.1007/s11090-015-9650-9.

[9] M. Baeva. A survey of chemical nonequilibrium in argon arc plasma. *Plasma Chem. Plasma Process.*, 37:513–530, 2017. URL: https://doi.org/10.1007/s11090-016-9778-2.

[10] K. H. Becker, U. Kogelschatz, K. H. Schoenbach, and R. J. Barker. *Non-equilibrium air plasmas at atmospheric pressure*. Plasma Physics. Institute of Physics Publishing, Bristol, UK, 2005. URL: https://doi.org/10.1201/9781482269123.

[11] M. S. Benilov and G. V. Naidis. Modelling of low-current discharges in atmospheric-pressure air taking account of non-equilibrium effects. *J. Phys. D: Appl. Phys.*, 36(15):1834–1841, 2003. URL: https://doi.org/10.1088/0022-3727/36/15/314.

[12] C. Biloiu, X. Sun, Z. Harvey, and E. Scime. An alternative method for gas temperature determination in nitrogen plasmas: Fits of the bands of the first positive system ($B^3\Pi_g \rightarrow A^3\Sigma_u^+$). *J. Appl. Phys.*, 101, 2007. URL: https://doi.org/10.1063/1.2537448.

[13] A. Bogaerts, E. Neyts, R. Gijbels, and J. J. A. M. van der Mullen. Gas discharge plasmas and their applications. *Spectrochim. Acta B*, 57(4):609–658, 2002. URL: https://doi.org/10.1016/S0584-8547(01)00406-2.

[14] Broadcom. *Qmini AFBR-S20M2xx - Miniature spectrometer with onboard processing for mobile applications and industrial integration (data sheet)*, July 2018.

[15] P. J. Bruggeman, F. Iza, and R. Brandenburg. Foundations of atmospheric pressure non-equilibrium plasmas. *Plasma Sources Sci. Technol.*, 26:123002, 2017. URL: http://dx.doi.org/10.1088/1361-6595/aa97af.

[16] T. M. Buzug. *Computer tomography*. Springer-Verlag Berlin Heidelberg, 2008. URL: https://doi.org/10.1007/978-3-540-39408-2.

[17] M. Cacciatore, M. Capitelli, and C. Gorse. Non-equilibrium dissociation and ionization of nitrogen in electrical discharges: the role of electronic collisions from vibrationally exited molecules. *Chem. Phys.*, 66:141–151, 1982. URL: https://doi.org/10.1016/0301-0104(82)88013-0.

[18] E. A. D. Carbone, S. Hübner, E. Iordanova, J. M. Palomares, and J. J. A. M. van der Mullen. Revision of the criterion to avoid electron heating during Laser Aided Plasma Diagnostics (LAPD). *J. Instrum.*, 7:C01016, 2012. URL: https://doi.org/10.1088/1748-0221/7/01/C01016.

[19] E. A. D. Carbone, S. Hübner, E. Iordanova, J. M. Palomares, and J. J. A. M. van der Mullen. Erratum: revision of the criterion for avoiding electron heating during Laser Aided Plasma Diagnostics (LAPD). *J. Instrum.*, 8, 2013. URL: https://doi.org/10.1088/1748-0221/8/05/E05001.

[20] E. A. D. Carbone and S. Nijdam. Thomson scattering on non-equilibrium low density plasmas: principles, practice and challenges. *Plasma Phys. Control. Fusion*, 57(1):014026, 2015. URL: https://doi.org/10.1088/0741-3335/57/1/014026.

[21] O. Carton, D. Ben Salem, S. Bhatt, J. Pulpytel, and F. Arefi-Khonsari. Plasma polymerization of acrylic acid by atmospheric pressure nitrogen plasma jet for biomedical applications. *Plasma Process. Polym.*, 9(10):984–993, 2012. URL: https://doi.org/10.1002/ppap.201200044.

[22] B. Chen, C. Zhu, L. Chen, J. Fei, Y. Gao, W. Wen, M. Shan, and Z. Ren. Atmospheric pressure plasma jet in organic solution: spectra, degradation effects of solution flow rate and initial pH value. *Plasma Sci. Technol.*, 16(12), 2014. URL: https://doi.org/10.1088/1009-0630/16/12/08.

[23] C.-J. Chen and S.-Z. Li. Spectroscopic measurement of plasma gas temperature of the atmospheric-pressure microwave incuded nitrogen plasma torch. *Plasma Sources Sci. Technol.*, 24(3), 2015. URL: https://doi.org/10.1088/0963-0252/24/3/035017.

[24] F. F. Chen. *Introduction to Plasma Physics and Controlled Fusion*, volume 1: Plasma Physics. Plenum Press, second edition, 1984. URL: https://doi.org/10.1007/978-3-319-22309-4.

[25] F. F. Chen and J. P. Chang. *Lecture Notes on Principles of Plasma Processing*. Plenum/Kluwer Publishers, 2002. URL: https://doi.org/10.1007/978-1-4615-0181-7.

[26] J. D. Cobine. *Gaseous conductors - theory and engineering applications*. Dover Publications Inc., 1958.

[27] V. Colombo, E. Ghedini, and P. Sanibondi. Thermodynamic and transport properties in non-equilibrium argon, oxygen and nitrogen thermal plasmas. *Prog. Nucl. Energy*, 50(8):921–933, 2008. URL: https://doi.org/10.1016/j.pnucene.2008.06.002.

[28] A. Compaan, A. Wagoner, and A. Aydinli. Rotational Raman scattering in the instructional laboratory. *Am. J. Phys.*, 62(7):639–645, 1994. URL: https://doi.org/10.1119/1.17484.

[29] Continuum. *Operating and maintenance manual for Surelite Lasers*, 996-0207 rev. j edition, 2002.

[30] Continuum. *Specification of Surelite I, II, III series*, 2002.

[31] J. Cooper. Plasma Spectroscopy. *Rep. Prog. Phys.*, 29(35), 1966. URL: https://doi.org/10.1088/0034-4885/29/1/302.

[32] D. L. Crintea, U. Czarnetzki, S. Iordanova, I. Koleva, and D. Luggenhölscher. Plasma diagnostics by optical emission spectroscopy on argon and comparison with Thomson scattering. *J. Phys. D: Appl. Phys.*, 42(4), 2009. URL: https://doi.org/10.1088/0022-3727/42/4/045208.

[33] B. A. Cruden, M. V. V. S. Rao, S. P. Sharma, and M. Meyyappan. Neutral gas temperature estimates in an inductively coupled $CF_4$ plasma by fitting diatomic emission spectra. *J. Appl. Phys.*, 91:8955–8964, 2002. URL: https://doi.org/10.1063/1.1474614.

[34] A. Czernichowski, H. Nassar, A. Ranaivosoloarimanana, A. A. Fridman, M. Šimek, K. Musiol, E. Pawelec, and L. Dittrichova. Spectral and electrical diagnostics of gliding arc. *Acta Phys. Pol.*, 89:595–603, 1996.

[35] W. Demtröder. *Molekülphysik*. Oldenbourg Verlag, München, Germany, 2003.

[36] W. Demtröder. *Laserspektroskopie 1, Grundlagen*. Springer-Verlag Berlin Heidelberg, 6. edition, 2011. URL: https://doi.org/10.1007/978-3-642-21306-9.

[37] W. Demtröder. *Laserspektroskopie 2, Experimentelle Techniken*. Springer-Verlag Berlin Heidelberg, 6. edition, 2013. URL: https://doi.org/10.1007/978-3-642-21447-9.

[38] M. Dobeic, S. Vadnjal, Z. Bajc, P. Umek, S. Pintarič, I. Uranjek, and K. Šinigoj Gačnik. Antibacterial properties of a non-thermal, atmospheric, Openair ®, plasma jet in surface decontamination of eggs in shell. *Slov. Vet. Res.*, 53(1), 2016. URL: https://www.slovetres.si/index.php/SVR/article/view/25/33.

[39] R. Dorai and M. J. Kushner. A model for plasma modification of polypropylene using atmospheric pressure discharges. *J. Phys. D: Appl. Phys.*, 36(6):666–685, 2003. URL: https://doi.org/10.1088/0022-3727/36/6/309.

[40] D. P. Dowling, M. Donegan, P. J. Cullen, V. J. Law, and V. Milosavljevic. Importance of plasma thermal energy transfer for plasma jet systems. *IEEE T. Plasma Sci.*, 42(10), 2014. URL: https://doi.org/10.1109/TPS.2014.2326962.

[41] D. P. Dowling, F. T. O'Neill, S. J. Langlais, and V. J. Law. Influence of a DC pulsed atmospheric pressure plasma jet processing conditions on polymer activation. *Plasma Process. Polym.*, 8:718–727, 2011. URL: https://doi.org/10.1002/ppap.201000145.

[42] D. P. Dowling and C. P. Stallard. Achieving enhanced material finishing using cold plasma treatments. *Transactions of the IMF*, 93:119–125, 2015. URL: https://doi.org/10.1179/0020296715Z.000000000240.

[43] N. A. Dyatko, Y. Z. Ionikh, and A. P. Napartovich. Influence of nitrogen admixture on plasma characteristics in a dc argon glow discharge and in afterglow. *Atoms*, 7(1), 2019. URL: https://doi.org/10.3390/atoms7010013.

[44] S. Eichler, N. Hussary, E. Siewert, and J. Schein. Investigation of the anode attachment process in plasma arc cutting. *J. Phys.: Conf. Ser.*, 550, 2014. URL: https://doi.org/10.1088/1742-6596/550/1/012007.

[45] D. E. Evans and J. Katzenstein. Laser light scattering in laboratory plasmas. *Rep. Prog. Phys.*, 32:207–271, 1969. URL: https://doi.org/10.1088/0034-4885/32/1/305.

[46] U. Fantz. Basics of plasma spectroscopy. *Plasma Sources Sci. Technol.*, 15:S137 – S147, 2006. URL: https://doi.org/10.1088/0963-0252/15/4/S01.

[47] G. Forster. *Bestimmung von Parametern thermischer Plasmen mittels Thomsonstreuung*. PhD thesis, Bundeswehr University Munich, Neubiberg, Germany, 1995.

[48] R. W. Fox, A. T. McDonald, and J. W. Mitchell. *Fox and McDonalds's introduction to fluid mechanics*. John Wiley & Sons Ltd, 10 edition, 2020.

[49] M. Fröhlich, S. Bornholdt, C. Regula, J. Ihde, and H. Kersten. Determination of the energy flux of a commercial atmospheric-pressure plasma jet for different process gases and distances between nozzle outlet and substrate surface. *Contrib. Plasma Phys.*, 54(2):155–161, 2014. URL: https://doi.org/10.1002/ctpp.201310062.

[50] D. H. Froula, S. H. Glenzer, N. C. Luhmann Jr., and J. Sheffield. *Plasma Scattering of Electromagnetic Radiation: Theory and Measurement Techniques*. Elsevier Academic Press, Amsterdam, The Netherlands, 2011. URL: https://doi.org/10.1016/C2009-0-20048-1.

[51] L. Fulcheri, J.-D. Rollier, and J. Gonzalez-Aguilar. Design and electrical charaterization of a low current - high voltage compact arc plasma torch. *Plasma Sources Sci. Technol.*, 16:183–192, 2007. URL: http://dx.doi.org/10.1088/0963-0252/16/1/023.

[52] G. Gardet, G. Moulard, M. Courbon, F. Rogemond, and M. Druetta. Evaluation of the rotational temperature in $n_2$ discharges using low-resolution spectroscopy. *Meas. Sci. Technol.*, 11(4):333–341, 2000. URL: https://doi.org/10.1088/0957-0233/11/4/301.

[53] M. A. Gigosos, M. A. Gonzalez, and V. Cardenoso. Computer simulated Balmer-alpha, -beta and -gamma Stark line profiles for non-equilibrium plasmas diagnostics. *Spectrochim. Acta B*, 58(8):1489–1504, 2003. URL: https://doi.org/10.1016/S0584-8547(03)00097-1.

[54] F. R. Gilmore, R. R. Laher, and P. J. Espy. Franck-Condon factors, r-centroids, electronic transition moments, and Einstein coefficients for many nitrogen and oxygen band systems. *J. Phys. Chem. Ref. Data*, 21(5), 1992. URL: https://doi.org/10.1063/1.555910.

[55] E. W. Gray and J. R. Pharney. Electrode erosion by particle ejection in low-current arcs. *J. Appl. Phys.*, 45(2), 1974. URL: https://doi.org/10.1063/1.1663300.

[56] H. R. Griem. *Spectral line broadening by plasmas*. Academic Press Inc., 1974.

[57] H. R. Griem. *Principles of Plasma Spectroscopy*. Cambridge Monographs on Plasma Physics. Cambridge University Press, 1997. URL: https://doi.org/10.1017/CBO9780511524578.

[58] H. R. Griem and R. H. Lovberg. *Plasma physics*, volume 9A of *Methods in Experimental Physics*. Academic Press Inc., New York, NY, USA, 1970.

[59] D. J. Griffiths. *Introduction To Electrodynamics*. Pearson Cambridge University Press, fourth edition, 2013.

[60] S. Gröger, M. Ramakers, M. Hamme, J. A. Medrano, N. Bibinov, F. Gallucci, A. Bogaerts, and P. Awakowicz. Characterization of a nitrogen gliding arc plasmatron using optical emission spectroscopy and high-speed camera. *J. Phys. D: Appl. Phys.*, 52(6):065201, 2018. URL: https://doi.org/10.1088/1361-6463/aaefe4.

[61] T. T. Gupta and H. Ayan. Application of non-thermal plasma on biofilm: a review. *Appl. Sci.*, 9(17), 2019. URL: https://doi.org/10.3390/app9173548.

[62] A. Gutsol, M. Kossitsyn, and A. A. Fridman. Generation and diagnostics of non-equilibrium plasma in gliding arc discharge. In *Electronic proceedings of 16th International Symposium on Plasma Chemistry, Taormina, Italy*, 22-27 June 2003.

[63] G. Herzberg. *Molecular Spectra and Molecular Structure.* D. Van Nostrand Company, Inc., I. Spectra of Diatomic Molecules edition, 1950.

[64] A. H. Hitchcock and A. E. Guile. A scanning electron microscope study of the role of copper oxide layers on arc cathode erosion rates. *J. Mater. Sci.*, 12:1095–1104, 1977. URL: https://doi.org/10.1007/BF00553598.

[65] P. Hoess. *Quantum Leap. The image intensifier module for continuous or gated operation providing high speed shutter.* Stanford Computer Optics Inc., 2014.

[66] P. Hoess. *4 Picos ultra high speed ICCD camera brochure.* Stanford Computer Optics Inc., Berkeley, CA, USA, June 2018.

[67] E. Hontañón, J. M. Palomares, M. Stein, X. Guo, R. Engeln, H. Nirschl, and F. E. Kruis. The transition from spark to arc discharge and its implications with respect to nanoparticle production. *J. Nanopart. Res.*, 15:1957, 2013. URL: https://doi.org/10.1007/s11051-013-1957-y.

[68] C.-C. Hsu and C.-Y. Wu. Electrical characterization of the glow-to-arc transition of an atmospheric pressure pulsed arc jet. *J. Phys. D: Appl. Phys.*, 42(21), 2009. URL: https://doi.org/10.1088/0022-3727/42/21/215202.

[69] K. P. Huber and G. Herzberg. *Molecular Spectra and Molecular Structure.* Springer Science+Business Media, IV. Constants of Diatomic Molecules edition, 1979. URL: https://doi.org/10.1007/978-1-4757-0961-2.

[70] S. Hübner, J. Santos Sousa, W. G. Graham, and J. J. A. M. van der Mullen. Thomson scattering on non-thermal atmospheric pressure plasma jets. *Plasma Sources Sci. Technol.*, 24:054005, 2015. URL: https://doi.org/10.1088/0963-0252/24/5/054005.

[71] R. H. Huddlestone and S. L. Leonard. *Plasma Diagnostic Techniques.* Academic Press Inc., 1965.

[72] S. Ikawa, A. Tani, Y. Nakashima, and K. Kitano. Physicochemical properties of bactericidal plasma-treated water. *J. Phys. D: Appl. Phys.*, 49(42), 2016. URL: https://doi.org/10.1088/0022-3727/49/42/425401.

[73] S. Iwarere, V. Rohani, D. Ramjugernath, F. Fabry, and L. Fulcheri. Hydrocarbons synthesis from syngas by very high pressure plasma. *Chem. Eng. J.*, 241, 2014. URL: http://dx.doi.org/10.1016/j.cej.2013.12.003.

[74] J. D. Jackson. *Classical Electrodynamics.* John Wiley & Sons Ltd, Hoboken, NJ, USA, third edition, 1999.

[75] J. F. James. *Spectrograph design fundamentals.* Cambridge University Press, Cambridge, UK, 2007.

[76] M. Janda, Z. Machala, L. Dvonč, D. A. Lacoste, and C. O. Laux. Self-pulsing discharges in pre-heated air at atmospheric pressure. *J. Phys. D: Appl. Phys.*, 48(3), 2015. URL: https://doi.org/10.1088/0022-3727/48/3/035201.

[77] N. Jeanvoine. *Plasma-material interaction and electrode degradation in high voltage ignition discharges.* PhD thesis, Saarland University, 2009. URL: http://dx.doi.org/10.22028/D291-22625.

[78] J. A. Jofre-Reche, J. Pulpytel, F. Arefi-Khonsari, and J. M. Martín-Martínez. Increased adhesion of polydimethylsiloxane (PDMS) to acrylic adhesive tape for medical use by surface treatment with an atmospheric pressure rotating plasma jet. *J. Phys. D: Appl. Phys.*, 49(33), 2016. URL: https://doi.org/10.1088/0022-3727/49/33/334001.

[79] J. Jonkers, L. J. M. Selen, J. J. A. M. van der Mullen, E. A. H. Timmermans, and D. C. Schram. Steep plasma gradients studied with spatially resolved Thomson scattering measurements. *Plasma Sources Sci. Technol.*, 6(4), 1997. URL: https://doi.org/10.1088/0963-0252/6/4/011.

[80] C. S. Kalra, Y. I. Cho, A. Gutsol, A. A. Fridman, and T. S. Rufael. Gliding arc in tornado using a reverse vortex flow. *Rev. Sci. Instrum.*, 76(2):025110, 2005. URL: https://doi.org/10.1063/1.1854215.

[81] M. Kehrer, J. Duchoslav, A. Hinterreiter, A. Mehic, and T. Stehrer. Surface functionalization of polypropylene using a cold atmospheric pressure plasma jet with gas water mixtures. *Surf. Coat. Technol.*, 384:125170, 2020. URL: https://doi.org/10.1016/j.surfcoat.2019.125170.

[82] M. Kehrer, A. Rottensteiner, W. Hartl, J. Duchoslav, T. Stehrer, and D. Stifter. Cold atmospheric pressure plasma treatment for adhesion improvement on polypropylene surfaces. *Surf. Coat. Technol.*, 403, 2020. URL: https://doi.org/10.1016/j.surfcoat.2020.126389.

[83] H. Kempkens and J. Uhlenbusch. Scattering diagnostics of low-temperature plasmas (Rayleigh scattering, Thomson scattering, CARS). *Plasma Sources Sci. Technol.*, 9:492–506, 2000. URL: https://doi.org/10.1088/0963-0252/9/4/305.

[84] T. Kewitz. *Diagnostik an Atmosphärendruck-Plasmajets.* PhD thesis, Kiel University, 2017.

[85] T. Kewitz, M. Fröhlich, J. von Frieling, and H. Kersten. Investigation of a commercial atmospheric pressure plasma jet by a newly designed calorimetric probe. *IEEE T. Plasma Sci.*, 43(5):1769–1773, 2015. URL: https://doi.org/10.1109/TPS.2015.2420679.

[86] T. Kewitz, C. Regula, M. Fröhlich, J. Ihde, and H. Kersten. Influence of the nozzle head geometry on the energy flux of an atmospheric pressure plasma jet. *EPJ Tech. Instrum.*, 8:1, 2021. URL: https://doi.org/10.1140/epjti/s40485-020-00061-4.

[87] J. H. Kim, Y. H. Choi, and Y. S. Hwang. Electron density and temperature measurement method by using emission spectroscopy in atmospheric pressure nonequilibrium nitrogen plasmas. *Phys. Plasmas*, 13, 2006.

[88] Y. Kim. Exploring emerging technologies with analysis of bibliographic data focused on plasma surface treatment. *Coatings*, 11, 2021. URL: https://doi.org/10.3390/coatings11111291.

[89] S. Kirner. *Tomographic two-color-pyrometry of the wire arc spray process regarding particle temperature and in-flight particle oxidation.* PhD thesis, Bundeswehr University Munich, 2018. URL: http://d-nb.info/1175916986.

[90] R. Köhler, P. Sauerbier, H. Militz, and W. Viöl. Atmospheric pressure plasma coating of wood and MDF with polyester powder. *Coatings*, 7(10):171, 2017. URL: https://doi.org/10.3390/coatings7100171.

[91] C. Kong, J. Gao, J. Zhu, A. Ehn, M. Aldén, and Z. Li. Re-igniting the afterglow plasma column of an AC powered gliding arc discharge in atmospheric-pressure air. *Appl. Phys. Lett.*, 112:264101, 2018. URL: https://doi.org/10.1063/1.5041262.

[92] N. Konjević, M. Ivković, and N. Sakan. Hydrogen Balmer lines for low electron number density plasma diagnostics. *Spectrochim. Acta B*, 76:16–26, 2012. URL: https://doi.org/10.1016/j.sab.2012.06.026.

[93] A. Kono and K. Iwamoto. High-spatial-resolution multichannel Thomson scattering measurements for atmospheric pressure microdischarge. *Jpn. J. Appl. Phys.*, 43(8):L1010–L1013, 2004. URL: https://doi.org/10.1143/JJAP.43.L1010.

[94] D. Korzec, D. Burger, and S. Nettesheim. Plasma activation from roll to roll. *Adhes. Adhes. Sealants*, 12:36–40, 03 2015. URL: https://doi.org/10.1007/s35784-015-0524-6.

[95] D. Korzec and S. Nettesheim. Application of a pulsed atmospheric arc plasma jet for low-density polyethylene coating. *Plasma Process. Polym.*, 17(1):1900098, 2020. URL: https://doi.org/10.1002/ppap.201900098.

[96] F. Krčma and M. Žáková. Pink afterglow in nitrogen-argon mixtures. *Eur. Phys. J. D*, 54:369–375, 2009. URL: https://doi.org/10.1140/epjd/e2009-00147-0.

[97] C. H. Kruger, C. O. Laux, Z. Machala, and G. V. Candler. Scaled-up nonequilibrium air plasmas. Technical report, Mechanical Engineering Department, Stanford University, 2004.

[98] C. H. Kruger, C. O. Laux, L. Yu, D. M. Packan, and L. Pierrot. Nonequilibrium discharges in air and nitrogen plasmas at atmospheric pressure. *Pure Appl. Chem.*, 74(3):337–347, 2002. URL: https://doi.org/10.1351/pac200274030337.

[99] Y. Kubota, R. Ichiki, T. Hara, N. Yamaguchi, and Y. Takemura. Spectroscopic analysis of nitrogen atmospheric plasma jet. *J. Plasma Fusion Res.*, 8:740–743, 2009.

[100] M. Kühn-Kauffeldt, J.-L. Marques, G. Forster, and J. Schein. Electron temperature and density measurement of tungsten inert gas arcs with *Ar-He* shielding gas mixture. *J. Instrum.*, 8:C10017, 2013. URL: https://doi.org/10.1088/1748-0221/8/10/C10017.

[101] H. J. Kunze. *Plasma diagnostics*, chapter The laser as a tool for plasma diagnostics. North-Holland Publishing Company, 1968.

[102] H. J. Kunze. *Introduction to Plasma Spectroscopy*. Springer Series on Atomic, Optical, and Plasma Physics. Springer-Verlag Berlin Heidelberg, 2009. URL: https://doi.org/10.1007/978-3-642-02233-3.

[103] C. O. Laux, T. G. Spence, C. H. Kruger, and R. N. Zare. Optical diagnostics of atmospheric pressure air plasmas. *Plasma Sources Sci. Technol.*, 12:125–138, 2003. URL: https://doi.org/10.1088/0963-0252/12/2/301.

[104] V. J. Law, F. T. O'Neill, and D. P. Dowling. Evaluation of the sensitivity of electro-acoustic measurements for process monitoring and control of an atmospheric pressure plasma jet system. *Plasma Sources Sci. Technol.*, 20(3), 2011. URL: https://doi.org/10.1088/0963-0252/20/3/035024.

[105] A. Lebouvier, C. Delalondre, F. Fresnet, V. Boch, V. Rohani, F. Cauneau, and L. Fulcheri. Three-dimensional unsteady MHD modeling of a low-current high-voltage nontransferred DC plasma torch operating with air. *IEEE T. Plasma Sci.*, 39(9):1889–1899, 2011. URL: https://doi.org/10.1109/TPS.2011.2160208.

[106] S.-H. Lee. Improving breakdown voltage characteristics of GDAs using trigger voltage. *J. Electr. Eng. Technol.*, 5(4):646–652, 2010. URL: https://doi.org/10.5370/JEET.2010.5.4.646.

[107] M. A. Lieberman and A. J. Lichtenberg. *Principles of plasma discharges and materials processing*. John Wiley & Sons Ltd, second edition, 2005.

[108] C. M. Limbach, C. Dumitrache, and A. P. Yalin. Laser Light Scattering from Equilibrium, High Temperature Gases: Limitations on Rayleigh Scattering Thermometry. In *47th AIAA Plasmadynamics and Lasers Conference*, 2016. URL: https://doi.org/10.2514/6.2016-3381.

[109] A. Lo, A. Cessou, C. Lacour, B. Lecordier, P. Boubert, D. A. Xu, C. O. Laux, and P. Vervisch. Streamer-to-spark transition initiated by a nanosecond overvoltage pulsed discharge in air. *Plasma Sources Sci. Technol.*, 26:045012, 2017. URL: https://doi.org/10.1088/1361-6595/aa5c78.

[110] A. Lofthus and P. H. Krupenie. The Spectrum of Molecular Nitrogen. *J. Phys. Chem. Ref. Data*, 6(1):113–307, 1977. URL: http://dx.doi.org/10.1063/1.555546.

[111] U. Lommatzsch, D. Pasedag, A. Baalmann, G. Ellinghorst, and H.-E. Wagner. Atmospheric pressure plasma jet treatment of polyethylene surfaces for adhesion improvement. *Plasma Process. Polym.*, 4, 2007. URL: https://doi.org/10.1002/ppap.200732402.

[112] D. A. Long. *The Raman Effect.* John Wiley & Sons Ltd, 2002. URL: https://doi.org/10.1002/0470845767.

[113] X. Lu. Effects of gas temperature and electron temperature on species concentration of air plasmas. *J. Appl. Phys.*, 102(3):033302, 2007. URL: https://doi.org/10.1063/1.2764242.

[114] Z. Machala, C. O. Laux, C. H. Kruger, and G. V. Candler. Atmospheric air and nitrogen DC glow discharges with thermionic cathodes and swirl flow. In *Proceedings of 42nd AIAA Aerospace Sciences Meeting and Exhibit, Reno, Nevada, USA*, 5-8 January 2004. URL: https://doi.org/10.2514/6.2004-355.

[115] Z. Machala, B. Tarabová, D. Sersenová, M. Janda, and K. Hensel. Chemical and antibacterial effects of plasma activated water: correlation with gaseous and aqueous reactive oxygen and nitrogen species, plasma sources and air flow conditions. *J. Phys. D: Appl. Phys.*, 52(3):034002, 2019. URL: https://doi.org/10.1088/1361-6463/aae807.

[116] A. Mai-Prochnow, R. Zhou, T. Zhang, K. K. Ostrikov, S. Mugunthan, S. A. Rice, and P. J. Cullen. Interactions of plasma-activated water with biofilms: inactivation, dispersal effects and mechanisms of action. *NPJ Biofilms Microbiomes*, 7(11):1–11, 2021. URL: https://doi.org/10.1038/s41522-020-00180-6.

[117] MatWeb Database. *Material properties of AlSI Type 316L Stainless Steel, annealed bar*, June 2021.

[118] MatWeb Database. *Material properties of copper, annealed*, June 2021.

[119] K. C. Meher, N. Tiwari, and S. Ghorui. Thermodynamic and transport properties of nitrogen plasma under thermal equilibrium and non-equilibrium conditions. *Plasma Chem. Plasma Process.*, 35:605–637, 2015. URL: https://doi.org/10.1007/s11090-015-9615-z.

[120] W. Merzkirch. *Flow visualization.* Academic Press Inc., second edition, 1987.

[121] R. B. Miles, W. R. Lempert, and J. N. Forkey. Laser Rayleigh scattering. *Meas. Sci. Technol.*, 12(5):R33–R51, 2001. URL: https://doi.org/10.1088/0957-0233/12/5/201.

[122] K. Muraoka and A. Kono. Laser Thomson scattering for low-temperature plasmas. *J. Phys. D: Appl. Phys.*, 44(4):043001, 2011. URL: https://doi.org/10.1088/0022-3727/44/4/043001.

[123] K. Muraoka and M. Maeda. *Laser-aided diagnostics of plasmas and gases.* Series in plasma physics. Institute of Physics Publishing, Bristol, UK, 2001. URL: https://doi.org/10.1201/9781420034066.

[124] K. Muraoka, K. Uchino, and M. D. Bowden. Diagnostics of low-density glow discharge plasmas using Thomson scattering. *Plasma Phys. Control. Fusion*, 40(7):1221 – 1239, 1998. URL: https://doi.org/10.1088/0741-3335/40/7/002.

[125] A. B. Murphy. Laser-scattering temperature measurements of a free-burning arc in nitrogen. *J. Phys. D: Appl. Phys.*, 27:1492–1498, 1994. URL: https://doi.org/10.1088/0022-3727/27/7/022.

[126] A. B. Murphy. Electron heating in the measurement of electron temperature by Thomson scattering: are thermal plasmas thermal? *Phys. Rev. Lett.*, 89(2):025002–1 – 4, 2002. URL: https://doi.org/10.1103/PhysRevLett.89.025002.

[127] A. B. Murphy. Thomson scattering diagnostics of thermal plasmas: Laser heating of electrons and the existence of local thermodynamic equilibrium. *Phys. Rev. E*, 69:016408–1 – 10, 2004. URL: https://doi.org/10.1103/PhysRevE.69.016408.

[128] A. B. Murphy and D. Uhrlandt. Foundations of high-pressure thermal plasmas. *Plasma Sources Sci. Technol.*, 27, 2018. URL: http://dx.doi.org/10.1088/1361-6595/aabdce.

[129] O. Mutaf-Yardimci, A. V. Saveliev, A. A. Fridman, and L. A. Kennedy. Thermal and nonthermal regimes of gliding arc discharge in air flow. *J. Appl. Phys.*, 87(4):1632–1641, 2000. URL: https://doi.org/10.1063/1.372071.

[130] H. Nagamatsu, R. Ichiki, Y. Yasumatsu, T. Inoue, M. Yoshida, S. Akamine, and S. Kanazawa. Steel nitriding by atmospheric-pressure plasma jet using $N_2/H_2$ mixture gas. *Surf. Coat. Technol.*, 225, 2013. URL: http://dx.doi.org/10.1016/j.surfcoat.2013.03.012.

[131] G. V. Naidis. Simulation of convection-stabilized low-current glow and arc discharges in atmospheric-pressure air. *Plasma Sources Sci. Technol.*, 16(2), 2007. URL: https://doi.org/10.1088/0963-0252/16/2/012.

[132] G. V. Naidis. Simulation of spark discharges in high-pressure air sustained by repetitive high-voltage nanosecond pulses. *J. Phys. D: Appl. Phys.*, 41(23), 2008. URL: https://doi.org/10.1088/0022-3727/41/23/234017.

[133] S. Narishige, S. Kitamura, S. Sakemi, K. Tomita, K. Uchino, K. Muraoka, and T. Sakoda. Thomson scattering diagnostics of glow discharge plasmas produced in Raman active gases. *Jpn. J. Appl. Phys.*, 41(11A):1259–1262, 2002. URL: https://doi.org/10.1143/JJAP.41.L1259.

[134] NIST atomic database. *https://www.nist.gov/pml/atomic-spectra-database*, June 2021. URL: https://www.nist.gov/pml/atomic-spectra-database.

[135] M. Noeske, J. Degenhardt, S. Strudthoff, and U. Lommatzsch. Plasma jet treatment of five polymers at atmospheric pressure: surface modifications and the relevance for adhesion. *Int. J. Adhes. Adhes.*, 24:171–177, 2004. URL: https://doi.org/10.1016/j.ijadhadh.2003.09.006.

[136] T. Nunnally, K. Gutsol, A. Rabinovich, A. A. Fridman, A. Gutsol, and A. Kemoun. Dissociation of $CO_2$ in a low current gliding arc plasmatron. *J. Phys. D: Appl. Phys.*, 44(27), 2011. URL: https://doi.org/10.1088/0022-3727/44/27/274009.

[137] V. N. Ochkin. *Spectroscopy of Low Temperature Plasma.* Wiley-VCH Verlag GmbH, 2009. URL: https://doi.org/10.1002/9783527627509.

[138] T. Orrière, E. Moreau, and D. Z. Pai. Ionization and recombination in nanosecond repetitively pulsed microplasmas in air at atmospheric pressure. *J. Phys. D: Appl. Phys.*, 51(49):494002, 2018. URL: https://doi.org/10.1088/1361-6463/aae134.

[139] D. Z. Pai, D. A. Lacoste, and C. O. Laux. Nanosecond repetitively pulsed discharges in air at atmospheric pressure - the spark regime. *Plasma Sources Sci. Technol.*, 19(6):065015, 2010. URL: https://doi.org/10.1088/0963-0252/19/6/065015.

[140] D. Z. Pai, D. A. Lacoste, and C. O. Laux. Transitions between corona, glow and spark regimes of nanosecond repetitively pulsed discharges in air at atmospheric pressure. *J. Appl. Phys.*, 107(9):093303, 2010. URL: https://doi.org/10.1063/1.3309758.

[141] J. M. Palomares, S. Hübner, E. A. D. Carbone, N. de Vries, E. M. van Veldhuizen, A. Sola, A. Gamero, and J. J. A. M. van der Mullen. $H_\beta$ Stark broadening in cold plasmas with low electron densities calibrated with Thomson scattering. *Spectrochim. Acta B*, 73:39–47, 2012. URL: https://doi.org/10.1016/j.sab.2012.07.005.

[142] J. M. Palomares, E. Iordanova, A. Gamero, A. Sola, and J. J. A. M. van der Mullen. Atmospheric microwave-induced plasmas in $Ar/H_2$ mixtures studied with a combination of passive and active spectroscopic methods. *J. Phys. D: Appl. Phys.*, 43(39), 2010. URL: https://doi.org/10.1088/0022-3727/43/39/395202.

[143] J. M. Palomares, E. Iordanova, S. Hübner, E. A. D. Carbone, and J. J. A. M. van der Mullen. Towards poly-diagnostics on cool atmospheric plasmas. *J. Instrum.*, 7:C02027, 2012. URL: https://doi.org/10.1088/1748-0221/7/02/C02027.

[144] J. Pawłat, P. Terebun, M. Kwiatkowski, B. Tarabová, Z. Koval'ová, K. Kučerová, Z. Machala, M. Janda, and K. Hensel. Evaluation of oxidative species in gaseous and liquid phase generated by mini-gliding arc discharge. *Plasma Chem. Plasma Process.*, 39:627–642, 2019. URL: https://doi.org/10.1007/s11090-019-09974-9.

[145] C. M. Penney, R. L. Peters, and M. Lapp. Absolute rotational Raman cross sections for $N_2$, $O_2$, and $CO_2$. *J. Opt. Soc. Am.*, 64(5):712 – 716, 1974. URL: https://doi.org/10.1364/JOSA.64.000712.

[146] J. Pulpytel, V. Kumar, P. Peng, V. Micheli, N. Laidani, and F. Arefi-Khonsari. Deposition of organosilicon coatings by a non-equilibrium atmospheric pressure plasma jet: design, analysis and macroscopic scaling law of the process. *Plasma Process. Polym.*, 8:664–675, 2011. URL: https://doi.org/10.1002/ppap.201000121.

[147] J. Rager. *Funkenerosion an Zündkerzenelektroden*. PhD thesis, Saarland University, 2006. URL: http://dx.doi.org/10.22028/D291-22327.

[148] Y. P. Raizer. *Gas Discharge Physics*. Springer-Verlag Berlin Heidelberg, 1991.

[149] J. Reece Roth. *Industrial plasma engineering - Volume 1: Principles*. Institute of Physics Publishing, Bristol, BS1 6BE, UK, 1995. URL: https://doi.org/10.1201/9780367802615.

[150] Relyon Plasma GmbH. *Operating instructions of plasma generator PG31*, October 2014.

[151] Relyon Plasma GmbH. *Operating manual of power supply PS2000*, May 2017.

[152] A. Risacher, S. Larigaldie, G. Bobillot, J.-P. Marcellin, and L. Picard. Active stabilization of low-current arc discharges in atmospheric-pressure air. *Plasma Sources Sci. Technol.*, 16(1):200–209, 2007. URL: https://doi.org/10.1088/0963-0252/16/1/025.

[153] J. Schein, A. Atzberger, and M. Szulc. Thermal plasmas: Influence of current modulation on process performance. In H. Toyoda and M. Vukovic, editors, *9th International Conference on Reactive Plasmas (ICRP-9): Conference Proceedings, Honolulu*. Japan Society of Applied Physics, October 2015.

[154] J. Schein and G. Forster. Innovative high-speed camera system diagnostics of plasma torch fluctuations. In *Thermal Spray 2008: Thermal Spray Crossing Borders, Proceedings from the International Thermal Spray Conference, Maastricht, Netherlands*. DVS Media GmbH, June 2008.

[155] C. D. Scott, H. E. Blackwell, S. Arepalli, and M. A. Akundi. Techniques for estimating rotational and vibrational temperature in nitrogen arcjet flow. *J. Thermophys. Heat Trans.*, 12(4), 1998. URL: https://doi.org/10.2514/2.6369.

[156] G. S. Settles. *Schlieren and shadowgraph techniques: visualizing phenomena in transparent media*. Springer-Verlag Berlin Heidelberg, 2001. URL: https://doi.org/10.1007/978-3-642-56640-0.

[157] E. Siewert, G. Wilhelm, M. Hässler, J. Schein, T. Hanson, M. Schnick, and U. Füssel. Visualization of gas flows in welding arcs by the Schlieren measuring technique. *Weld. J.*, 93(1), January 2014.

[158] B. M. Smirnov. *Plasma Processes and Plasma Kinetics : 586 Worked Out Problems for Science and Technology*. Wiley-VCH Verlag GmbH, 2007.

[159] R. Snoeckx and A. Bogaerts. Plasma technology - a novel solution for $CO_2$ conversion? *Chem. Soc. Rev.*, 46(19):5805–5863, 2017. URL: https://doi.org/10.1039/C6CS00066E.

[160] SpectralFit, S.A.S. *Specair v3.0 - User manual*, 2012. URL: http://spectralfit.com/manual.php.

[161] A. Starek, A. Sagan, D. Andrejko, B. Chudzik, Z. Kobus, M. Kwiatkowski, P. Terebun, and J. Pawłat. Possibility to extend the shelf life of NFC tomato juice using cold atmospheric pressure plasma. *Sci. Rep.*, 10, 2020. URL: https://doi.org/10.1038/s41598-020-77977-0.

[162] W. S. Struve. *Fundamentals of Molecular Spectroscopy*. John Wiley & Sons Ltd, 1989.

[163] J. A. Sutton and J. F. Driscoll. Rayleigh scattering cross sections of combustion species at 266, 355 and 532 nm for thermometry applications. *Opt. Lett.*, 29(22):2620–2622, 2004. URL: https://doi.org/10.1364/OL.29.002620.

[164] M. Szulc, S. Kirner, G. Forster, and J. Schein. A novel approach to determine in-flight particle oxidation for thermal spraying processes. *J. Therm. Spray Tech.*, 29:932–946, 2020. URL: https://doi.org/10.1007/s11666-020-01055-0.

[165] M. Szulc, S. Schein, J. Schaup, J. Schein, and S. Zimmermann. Suitability of thermal plasmas for large-area bacteria inactivation on temperature-sensitive surfaces - first results with Geobacillus stearothermophilus spores. *J. Phys.: Conf. Ser.*, 825:012017, 2017. URL: https://doi.org/10.1088/1742-6596/825/1/012017.

[166] Y. Tanaka. Time-dependent two-temperature chemically non-equilibrium modelling of high-power $Ar$-$N_2$ pulse-modulated inductively coupled plasmas at atmospheric pressure. *J. Phys. D: Appl. Phys.*, 39(2):307–319, 2006. URL: https://doi.org/10.1088/0022-3727/39/2/011.

[167] Y. Tanaka, T. Michishita, and Y. Uesugi. Hydrodynamic chemical non-equilibrium model of a pulsed arc discharge in dry air at atmospheric pressure. *Plasma Sources Sci. Technol.*, 14(1):134–151, 2005. URL: https://doi.org/10.1088/0963-0252/14/1/016.

[168] TAOS Inc. *TCS3472 - color light-to-digital converter with IR filter (data sheet)*, August 2012.

[169] P. Teulet, J. P. Sarrette, and A. M. Gomes. Collisional-radiative modelling of one- and two-temperature air and air-sodium plasmas at atmospheric pressure with temperatures of 2000 – 12000 K. *J. Quant. Spectrosc. Radiat. Transf.*, 70(2):159–187, 2001. URL: https://doi.org/10.1016/S0022-4073(00)00129-1.

[170] R. Thalman, K. J. Zarzana, M. A. Tolbert, and R. Volkamer. Rayleigh scattering cross-section measurements of nitrogen, argon, oxygen and air. *J. Quant. Spectrosc. Radiat. Transf.*, 147:171–177, 2014. URL: http://dx.doi.org/10.1016/j.jqsrt.2014.05.030.

[171] A. P. Thorne. *Spectrophysics.* Chapman and Hall, second edition, 1988. URL: https://doi.org/10.1007/978-94-009-1193-2.

[172] E. Traldi, M. Boselli, E. Simoncelli, A. Stancampiano, M. Gherardi, V. Colombo, and G. S. Settles. Schlieren imaging: a powerful tool for atmospheric plasma diagnostic. *EPJ Tech. Instrum.*, 5, 2018. URL: https://doi.org/10.1140/epjti/s40485-018-0045-1.

[173] J. P. Trelles. Nonequilibrium phenomena in (quasi-)thermal plasma flows. *Plasma Chem. Plasma Process.*, 40:727–748, 2020. URL: https://doi.org/10.1007/s11090-019-10046-1.

[174] K. Urashima and J.-S. Chang. Removal of volatile organic compounds from air streams and industrial flue gases by non-thermal plasma technology. *IEEE Trans. Dielectr. Electr. Insul.*, 7(5), 2000. URL: https://doi.org/10.1109/94.879356.

[175] M. J. van de Sande. *Laser scattering on low temperature plasmas. High resolution and stray light rejection.* PhD thesis, Technische Universiteit Eindhoven, Eindhoven, The Netherlands, 2002.

[176] A. F. H. van Gessel, E. A. D. Carbone, P. J. Bruggeman, and J. J. A. M. van der Mullen. Laser scattering on an atmospheric pressure plasma jet: disentangling Rayleigh, Raman and Thomson scattering. *Plasma Sources Sci. Technol.*, 21(1):015003, 2012. URL: https://doi.org/10.1088/0963-0252/21/1/015003.

[177] Vishay Semiconductors. *VEML6040 - RGBW color sensor with $I^2C$ interface (data sheet)*, November 2016.

[178] L. Wallenhorst. *Protective particle coatings applied by cold plasma spraying.* PhD thesis, Georg-August University School of Science, Göttingen, Germany, 2017.

[179] W. Z. Wang, M. Z. Rong, J. D. Yan, A. B. Murphy, and J. W. Spencer. Thermophysical properties of nitrogen plasmas under thermal equilibrium and non-equilibrium conditions. *Phys. Plasmas*, 18:113502, 2011. URL: https://doi.org/10.1063/1.3657426.

[180] K.-D. Weltmann, J. F. Kolb, M. Holub, D. Uhrlandt, M. Šimek, K. K. Ostrikov, S. Hamaguchi, U. Cvelbar, M. Černák, B. Locke, A. A. Fridman, P. Favia, and K. H. Becker. The future for plasma science and technology. *Plasma Process. Polym.*, 16(1):1800118, 2019. URL: https://doi.org/10.1002/ppap.201800118.

[181] C. Wiegand, O. Beier, K. Horn, A. Pfuch, T. Tölke, U.-C. Hipler, and A. Schimanski. Antimicrobial impact of cold atmospheric pressure plasma on medical critical yeasts and bacteria cultures. *Skin Pharmacol. Physiol.*, 27(1):25–35, 2014. URL: https://doi.org/10.1159/000351353.

[182] C. Wiegand, S. Fink, U.-C. Hipler, O. Beier, K. Horn, A. Pfuch, A. Schimanski, and B. Grünler. Cold atmospheric pressure plasmas exhibit antimicrobial properties against critical bacteria and yeast species. *J. Wound Care*, 26(8), 2017. URL: https://doi.org/10.12968/jowc.2017.26.8.462.

[183] D. Xiao, C. Cheng, J. Shen, Y. Lan, H. Xie, X. Shu, Y. Meng, J. Li, and P. K. Chu. Electron density measurements of atmospheric-pressure non-thermal $N_2$ plasma jet by Stark broadening and irradiance intensity methods. *Phys. Plasmas*, 21, 2014. URL: http://dx.doi.org/10.1063/1.4879033.

[184] D. A. Xu, M. N. Shneider, D. A. Lacoste, and C. O. Laux. Thermal and hydrodynamic effects of nanosecond discharges in atmospheric pressure air. *J. Phys. D: Appl. Phys.*, 47, 2014. URL: https://doi.org/10.1088/0022-3727/47/23/235202.

[185] Z. Xu, X. Zhou, W. Yang, Y. Zhang, Z. Ye, S. Hu, C. Ye, Y. Li, Y. Lan, J. Shen, X. Ye, F. Yang, and C. Cheng. In vitro antimicrobial effects and mechanism of air plasma-activated water on *Staphylococcus aureus* biofilm. *Plasma Process. Polym.*, 17(8), 2020. URL: https://doi.org/10.1002/ppap.201900270.

[186] L. Yu, L. Pierrot, C. O. Laux, and C. H. Kruger. Effects of vibrational nonequilibrium on the chemistry of two-temperature nitrogen plasmas. *Plasma Chem. Plasma Process.*, 21(4):483–503, 2001. URL: https://doi.org/10.1023/A:1012073800284.

[187] H. Zeghioud, P. Nguyen-Tri, L. Khezami, A. Amrane, and A. A. Assadi. Review on discharge plasma for water treatment: mechanism, reactor geometries, active species and combined processes. *J. Water Process. Eng.*, 38:101664, 2020. URL: https://doi.org/10.1016/j.jwpe.2020.101664.

[188] J. Zhu, A. Ehn, J. Gao, C. Kong, M. Aldén, M. Salewski, F. Leipold, Y. Kusano, and Z. Li. Translational, rotational, vibrational and electron temperatures of a gliding arc discharge. *Opt. Express*, 25(17):20243–20257, 2017. URL: https://doi.org/10.1364/OE.25.020243.

[189] S. Zimmermann, A. Atzberger, J. Schein, M. Szulc, and J. Zierhut. Pulsed current and pulsed powder operation of the One-Cathode-One-Anode-Plasma-Generator (OCOAPG). In *International Thermal Spray Conference ITSC2017: Proceedings of the Conference in Düsseldorf (Germany)*, volume 336 of *DVS-Berichte*. DVS Media GmbH, June 2017.